

A neutral atom quantum register

von
Dominik Schrader

Bonn 2004

Mathematisch-Naturwissenschaftliche Fakultät
der
Rheinischen Friedrich-Wilhelms-Universität Bonn

Angefertigt mit Genehmigung
der Mathematisch-Naturwissenschaftlichen Fakultät
der Rheinischen Friedrich-Wilhelms-Universität Bonn

1. Gutachter: Prof. Dr. Dieter Meschede
2. Gutachter: Prof. Dr. Karsten Buse

Tag der Promotion: 16.12.2004

Dieser Forschungsbericht ist auf dem Hochschulschriftenserver der ULB
Bonn http://hss.ulb.uni-bonn.de/diss_online elektronisch publiziert.

Summary / Zusammenfassung

In this thesis I present the realization of a quantum register of single neutral atoms, which is a building block of a quantum computer. It consists of a well known number of “qubits” – the quantum analogs of classical bits – that can be individually addressed and coherently manipulated. Here, a string of single cesium atoms trapped in the potential wells of a standing wave optical dipole trap serves as quantum register. The quantum information is encoded into the hyperfine states of the atoms which are coherently manipulated using microwave radiation.

Chapter 1 is devoted to the presentation of a number of tools to control all degrees of freedom of single neutral atoms. A magneto-optical trap provides an exactly known number of cold atoms which are transferred into an optical dipole trap. A photon-counting CCD camera along with molasses cooling allow us to continuously observe the trapped atoms including their controlled transport along the trap axis using our optical “conveyor belt”. Finally, I present techniques to initialize, coherently manipulate and measure the hyperfine states of individual atoms with high efficiency.

The experimental realization of the quantum register is the focus of Chapter 2, where I describe its working principle and fully characterize its properties. Write and read operations on the quantum register are performed by position-selective coherent manipulation of atom qubits and state-selective measurements. For this purpose, an image is acquired to determine the positions of all trapped atoms. A magnetic field gradient is applied along the trap axis so that individual atom qubits are addressed by tuning the frequency of the microwave radiation to the respective Zeeman-shifted atomic resonance frequency. This addressing scheme operates with a spatial resolution of $2.5 \mu\text{m}$ and qubit rotations on individual atoms are performed with 99 % contrast including all experimental imperfections. In a final read-out operation each individual atomic state is analyzed. I finally investigate the coherence properties of the quantum register in detail and identify the mechanisms that lead to decoherence.

Gegenstand dieser Arbeit ist die Realisierung eines Quantenregisters aus einzelnen neutralen Atomen, welches einen zentralen Baustein eines Quantencomputers bildet. Ein Quantenregister besteht aus einer wohldefinierten Anzahl von “Qubits” – den quantenmechanischen Analoga von Bits – die individuell adressiert und kohärent manipuliert werden können. Die Qubits werden in dieser Arbeit mit einzelnen Cäsiumatomen realisiert, die in den Potentialtöpfen einer optischen Dipolfalle in Stehwellen-Konfiguration gefangen sind. Die Quanteninformation ist in den Hyperfein-Zuständen der Atome kodiert, die mit Hilfe von Mikrowellenstrahlung kohärent manipuliert werden.

In Kapitel 1 stelle ich eine Reihe von Werkzeugen vor, um sämtliche Freiheitsgrade einzelner neutraler Atome zu kontrollieren. Eine magneto-optische Falle dient als Quelle einer genau bestimmten Anzahl von kalten Atomen, die dann in eine optische Dipolfalle umgeladen werden. Mit Hilfe von Melasse-Kühlverfahren und einer photonenzählenden CCD-Kamera können wir die gespeicherten Atome und sogar deren kontrollierten Transport kontinuierlich beobachten. Schließlich beschreibe ich die Techniken, mit denen wir die Hyperfeinzustände einzelner Atome mit hoher Effizienz präparieren, kohärent manipulieren und messen.

Die experimentelle Realisierung des Quantenregisters steht im Zentrum von Kapitel 2. Ich beschreibe sein Funktionsprinzip und charakterisiere seine Eigenschaften umfassend. Die einzelnen Qubits des Registers werden mit Hilfe von positionselektiver kohärenter Manipulation beschrieben und analysiert. Zu diesem Zweck bestimmen wir zunächst die Positionen aller gespeicherten Atome, indem wir ein Bild der Atomkette auswerten. In einem Magnetfeldgradienten adressieren wir dann einzelne Atome mit Mikrowellenstrahlung, indem wir die Mikrowellenfrequenz auf die Zeeman-verschobene Resonanzfrequenz des entsprechenden Atoms abstimmen. Die räumliche Auflösung dieser Adressiertechnik beträgt $2,5 \mu\text{m}$. Sie ermöglicht uns, Qubit-Rotationen auf einzelnen Atomen mit einem Kontrast von 99 % durchzuführen, einschließlich aller experimentellen Imperfektionen. Zum Schluss untersuche ich detailliert die Kohärenzeigenschaften des Quantenregisters und identifiziere die Dekohärenzmechanismen.

Parts of this thesis have been published in the following journal articles:

1. D. SCHRADER, I. DOTSENKO, M. KHUDAVERDYAN, Y. MIROSHNYCHENKO, A. RAUSCHENBEUTEL, AND D. MESCHEDE, *Neutral atom quantum register*, Phys. Rev. Lett. **93**, 150501 (2004)
2. M. KHUDAVERDYAN, W. ALT, I. DOTSENKO, L. FÖRSTER, S. KUHR, D. MESCHEDE, Y. MIROSHNYCHENKO, D. SCHRADER, AND A. RAUSCHENBEUTEL, *Adiabatic quantum state manipulation of single trapped atoms*, Phys. Rev. A (2005), in print, available at [arXiv:quant-ph/0411120](https://arxiv.org/abs/quant-ph/0411120)
3. Y. MIROSHNYCHENKO, D. SCHRADER, S. KUHR, W. ALT, I. DOTSENKO, M. KHUDAVERDYAN, A. RAUSCHENBEUTEL, AND D. MESCHEDE, *Continued imaging of the transport of a single neutral atom*, Optics Express **11**, 3498 (2003)
4. S. KUHR, W. ALT, D. SCHRADER, I. DOTSENKO, Y. MIROSHNYCHENKO, W. ROSENFELD, M. KHUDAVERDYAN, V. GOMER, A. RAUSCHENBEUTEL, AND D. MESCHEDE, *Coherence properties and quantum state transportation in an optical conveyor belt*, Phys. Rev. Lett. **91**, 213002 (2003)
5. W. ALT, D. SCHRADER, S. KUHR, M. MÜLLER, V. GOMER, AND D. MESCHEDE, *Single atoms in a standing-wave dipole trap*, Phys. Rev. A **67**, 033403 (2003)
6. D. SCHRADER, S. KUHR, W. ALT, M. MÜLLER, V. GOMER, AND D. MESCHEDE, *An optical conveyor belt for single neutral atoms*, Appl. Phys. B **73**, 819 (2001)

Contents

Introduction	1
1 Tools for single atom control	3
1.1 A single atom MOT	4
1.1.1 Principle	4
1.1.2 Experimental setup	6
1.1.3 Single atom detection	9
1.2 A standing wave optical dipole trap	10
1.2.1 Dipole potential	10
1.2.2 Experimental setup of the dipole trap	13
1.2.3 Transfer of a single atom between MOT and dipole trap	14
1.3 Imaging single atoms	14
1.3.1 Properties of the intensified CCD camera	15
1.3.2 Imaging system	15
1.3.3 Illumination of single atoms in the dipole trap	16
1.3.4 Images of single trapped atoms	19
1.4 An optical conveyor belt	23
1.4.1 A moving standing wave	23
1.4.2 Imaging the controlled motion of a single atom	26
1.5 State preparation and detection	26
1.5.1 State preparation by optical pumping	27
1.5.2 Single atom state-selective detection	28
1.6 Quantum state preparation using microwave radiation	30
1.6.1 Bloch vector model	31
1.6.2 Experimental microwave setup	32
1.6.3 Frequency calibration	33
1.6.4 Rabi rotations	36
1.7 Robust spin flips by adiabatic population transfer	37
1.7.1 Dressed state picture	38
1.7.2 Experimental setup for adiabatic frequency sweeps	40
1.7.3 Spectrum of adiabatic population transfer	41
1.8 Conclusion	44
2 Experimental realization of a neutral atom quantum register	47
2.1 Introduction	47
2.2 Calibration of the position dependent atomic resonance	48
2.2.1 Magnetic field	48
2.2.2 Experimental sequence	49
2.2.3 Result	51
2.3 Position-selective quantum state preparation	52

2.3.1	Addressing of a single atom	52
2.3.2	Addressing resolution	56
2.3.3	Position-selective adiabatic population transfer	62
2.3.4	Rabi rotations	64
2.3.5	Multi-atom addressing	65
2.3.6	Scalability	67
2.4	Coherence properties	68
2.4.1	Crosstalk	68
2.4.2	Optical Bloch equations with damping	69
2.4.3	Ramsey spectroscopy in a magnetic guiding field	70
2.4.4	Spin echo spectroscopy in a magnetic guiding field	73
2.4.5	Dephasing mechanisms in a magnetic guiding field	75
2.4.6	Spin echo spectroscopy in a magnetic field gradient	78
2.4.7	Dephasing mechanisms in a magnetic field gradient	80
2.4.8	Discussion	87
3	Conclusion and outlook	89
3.1	A cavity-QED quantum gate with neutral atoms	90
3.1.1	An optical high-finesse resonator for storing photons	90
3.1.2	A four-photon entanglement scheme	90
3.2	Single atom sorting	92
3.3	A single-atom interferometer	93
A	Light shifts in multi-level atoms	95
B	An entanglement scheme for two atoms in a cavity	99
B.1	Hamiltonian of a coupled atom-atom-cavity system	99
B.2	Master equation approach to model dissipation	101
B.3	Numerical calculation for our system parameters	101
	List of Figures	105
	List of Tables	107
	Bibliography	109
	Acknowledgements	117

Introduction

In the past century, research in quantum mechanics was initially focussed on the theoretical exploration and later on the experimental investigation of quantum effects. At the beginning of the 21st century, the field of “quantum engineering”, i. e. the experimental control of individual quantum systems, opens the route to practical applications of genuine quantum effects that were so far considered to be of theoretical interest only. In this context, quantum information processing has emerged as a field of research with potentially very powerful applications, where information is coded into the quantum states of microscopic physical systems (qubits). The quantum concepts of state superposition and entanglement can lead to a dramatic speed up in solving certain classes of computational problems, such as factoring [1] and sorting algorithms [2].

Over the past decade various quantum computing schemes have been proposed. In a sequential network of quantum logic gates information is processed using discrete one- and two-qubit operations [3]. Following a different approach, the “one-way quantum computer” processes information by performing one-qubit rotations and measurements on an entangled cluster state [4]. All of these schemes require a quantum register, i. e. a well known number of qubits each of which can be prepared in a desired quantum state. Write and read operations on a quantum register are performed by coherent one-qubit rotations of individually addressed qubits and by state-selective measurements.

Several physical systems, such as ions in a linear Paul trap [5], nuclear spins in molecules [6], or magnetic flux qubits [7] can serve as quantum registers. With some of them, significant achievements in quantum computing have already been accomplished. Trapped ions have successfully been entangled [8, 9], which led to the recent implementation of quantum gates [10, 11] and the Deutsch-Jozsa quantum algorithm [12]. Using nuclear spins in molecules, Shor’s factoring algorithm was implemented by demonstrating factorization of the number “15” [13].

Neutral atoms also exhibit favorable properties for storing and processing quantum information and represent an alternative physical system to perform quantum computation. Their hyperfine ground states are readily prepared in pure quantum states including state superpositions and can be well isolated from their environment. The resulting long coherence times and the easy state manipulation and analysis by means of microwave radiation already gave rise to technical applications such as atomic clocks and can also turn into virtue in quantum information processing. In addition, countable numbers of neutral atoms can be trapped using laser cooling techniques and their external degrees of freedom

can be manipulated [14, 15]. The coherence properties of laser trapped atoms have been found to be adequate for storing quantum information [16, 17]. Moreover, controlled cold collisions [18] or the exchange of microwave [19] or optical [20, 21] photons in a resonator offer interesting schemes for mediating coherent atom–atom interaction, essential for the realization of quantum logic operations.

In this thesis, I present the realization of a quantum register using a string of an exactly known number of neutral cesium atoms [22]. The atoms are trapped in the potential wells of a spatially modulated, light induced potential created by a far detuned standing wave dipole trap [14, 23]. The positions of the atoms can be optically resolved with an imaging system using an intensified CCD camera [24, 25]. We use microwave radiation to coherently manipulate the atomic hyperfine ground states, which encode the quantum information. A magnetic field gradient along the trap axis allows us to spectroscopically resolve the individual atoms in order to perform selective coherent one-qubit operations on the quantum register. Our addressing scheme operates with a high spatial resolution of $2.5\ \mu\text{m}$ and qubit rotations on individual atoms are performed with 99 % contrast. In a final read-out operation we analyze each individual atomic state. Finally, I have measured the coherence time and performed a detailed investigation of the dephasing mechanisms of our quantum register.

Five basic requirements for building a quantum computer have been postulated by DiVincenzo [26]. They include the availability of a scalable physical system with well characterized qubits, the ability to initialize and to measure the states of the qubits, long relevant coherence times, and a universal set of quantum gates. Except for the demonstration of two-qubit quantum gates, our quantum register fulfils all of these criteria. This work therefore represents an important step towards quantum computing with neutral atoms [27].

In order to pursue the next step on this route – the implementation of a two-qubit quantum gate – we have designed our quantum register to be compatible with the requirements of cavity quantum electrodynamics experiments. Our optical conveyor belt [14, 23] should allow us to deterministically place two atoms inside the mode of a high-finesse optical resonator. Here, two-qubit gate operations could be performed by the exchange of cavity photons. Since our scheme of addressing individual atom qubits does not require optical access to the trapped atoms, coherent selective one-qubit operations will even be possible inside the cavity. Our quantum register is therefore a versatile tool for the implementation of quantum logic operations.

Chapter 1

Tools for single atom control

Quantum engineering at the single atom level requires a spectrum of techniques to control all degrees of freedom of neutral atoms. During the past years we have advanced standard experimental methods and invented new tools that allow us to trap, to detect and to manipulate individual atoms. In order to control their external degrees of freedom we employ two different types of laser traps, a magneto-optical trap and a dipole trap. For coherent manipulation of internal atomic states microwave radiation has shown to be well suited.

The invention of laser cooling in 1975 [28, 29] and its first realization by S. Chu in 1985 [30] has opened the door to experimental research with cold neutral atoms. The magneto-optical trap (MOT), first realized in 1987 [31], has evolved to become the standard cold atom source for hundreds of experiments world-wide and has been a prerequisite for tremendous achievements such as the creation of Bose-Einstein condensates [32, 33]. The operation of such a MOT in special regimes has also permitted the capture and observation of single cold atoms [34, 35, 36]. We have advanced these trapping techniques such that we routinely operate a single atom MOT.

Optical tweezers can move microscopic objects without mechanical contact [37] and have proven to be a reliable and precise tool in biology, photochemistry, and nanofabrication [38]. Also known as optical dipole traps, they attract polarizable particles into regions of high electric field strength, e. g. in the focus of a laser beam [39], and became a valuable technique for the manipulation of cold atoms [40]. Just a few years ago, we demonstrated the transfer of a single cesium atom from the MOT into a dipole trap [41]. We now use a standing-wave variant of this trap as an “optical conveyor belt” which tightly confines single atoms in space and transports them over distances of up to 1 cm with sub-micrometer precision [14, 23]. In contrast to the MOT, the dipole trap has the advantage that the laser frequency can be far off-resonant with respect to all atomic resonance frequencies so that the coherence of long-lived internal states is not destroyed by excitations.

The observation of single atoms is essential for controlling their degrees of freedom. The first image of an individual atomic particle in a trap was obtained by recording the fluorescence light from a single barium ion on a photographic plate in 1980 [42]. Technological

advances during the following decades have made high-efficiency photon-counting cameras available which permit the imaging of trapped ion crystals [43, 44] and of single neutral atoms in an optical dipole trap [15]. The development of a home-made diffraction-limited objective [24] has enabled us to detect and image the fluorescence light of a single atom and of trapped neutral atom strings with high signal-to-noise ratio. Efficient cooling of the atoms in our dipole trap recently allowed us to continuously image the controlled transport of a single atom [25].

In addition to the control of external degrees of freedom of single atoms, manipulation and detection of the internal atomic states are essential tools for quantum engineering. The first experiments of atomic state preparation by optical pumping were performed in 1949 [45, 46] with the selective population of Zeeman levels of mercury atoms. Later, the quantum shelving technique permitted to measure the state of a single trapped ion by the observation of quantum jumps [47].

Recently, we have demonstrated atomic state preparation and detection at the level of a single neutral atom with nearly perfect efficiency. For the preparation of quantum states, coherent manipulation of the internal atomic states is required. In the case of cesium atoms, the long-living hyperfine ground states are well suited to store quantum information [17, 48, 49] and can easily be manipulated and analyzed by means of microwave radiation. Similar to the phenomenon of nuclear magnetic resonance [50], the interaction of the electromagnetic field with the atomic dipole moment leads to the observation of Rabi oscillations [51]. In addition to the preparation of quantum states by inducing Rabi rotations, we use a microwave frequency sweep to implement a more robust technique for efficient population transfer using the method of adiabatic passage [52].

1.1 A single atom MOT

Magneto-optical traps (MOTs) have been the draft horses to cool neutral atoms to temperatures of about $100 \mu\text{K}$ for almost two decades. They employ standard laser cooling techniques and are quite robust with respect to variations of experimental conditions. We have set up a MOT to provide single cold cesium atoms for our experiments. Their fluorescence light is imaged on a single photon detector and allows us to count the exact atom number in real-time.

1.1.1 Principle

The working principle of a MOT relies on a velocity dependent cooling force and a position dependent restoring force to provide spatial confinement of the atoms. The first is realized by three orthogonal, counterpropagating pairs of laser beams which are slightly red detuned with respect to the atomic resonance. A moving atom preferentially absorbs photons from those laser beams opposed to its direction of motion because their frequencies are Doppler shifted closer to the atomic resonance. The net force resulting from the momentum transfer of the absorbed and isotropically emitted photons slows the atom down. This so-called Doppler force ideally cools atoms to the Doppler temperature

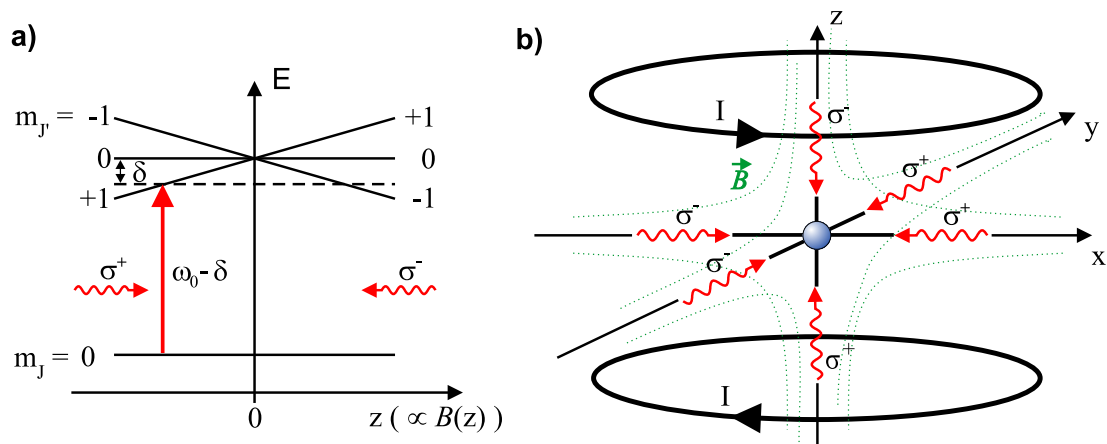


Figure 1.1: Magneto-optical trap (MOT). (a) In this 1-D model the $J' = 1$ excited state of an atom is Zeeman split in the linear magnetic field gradient. If the atom is displaced from the center to the left, the $m_J = 0 \leftrightarrow m_J = 1$ transition is shifted into resonance and is excited only by the σ^+ -polarized laser from the left which pushes the atom back into the center. (b) Anti-Helmholtz configuration of the magnetic field to produce the 3-D quadrupole field for the MOT, and corresponding laser polarizations.

$T_D = \hbar\Gamma/2k_B$, where Γ is the natural linewidth of the atom. For cesium, $\Gamma = 2\pi \cdot 5.22$ MHz and $T_D = 125$ μ K.

The restoring force is obtained by adding a quadrupole magnetic field and by circularly polarizing the laser beams. The magnetic field is zero at the center and increases linearly in radial direction. It lifts the degeneracy of the Zeeman multiplicity of the excited state of the model atom in Figure 1.1. If the circular polarizations of the laser beams are set correctly, an atom which is displaced from the center of the quadrupole field is shifted into resonance with that laser beam which pushes the atom back to the center. As a result, a MOT simultaneously cools and confines atoms in space.

Standard MOTs typically trap $10^6 - 10^{10}$ atoms. To capture very few atoms only, our MOT operates in a regime where the rate at which atoms are loaded into the MOT, R_{load} , is significantly reduced [36, 53]. Since

$$R_{\text{load}} \propto \left(\frac{\partial B}{\partial z} \right)^{-14/3} \quad (1.1)$$

we apply a high magnetic field gradient of $\partial B/\partial z = 340$ G/cm to decrease R_{load} by six orders of magnitude with respect to standard MOTs, where $\partial B/\partial z = 20$ G/cm. In addition, by loading the atoms from the background vapor instead of feeding the MOT by an atomic beam, we achieve loading rates as low as 1-10 atoms/min.

Many of our experiments demand the presence of exactly one atom. In addition, single atom experiments require many repetitions for good statistics. In order to reduce the overall measurement times, we circumvent the drawback of the long waiting time until an atom is captured by the MOT. We actively load atoms into the MOT by decreasing its

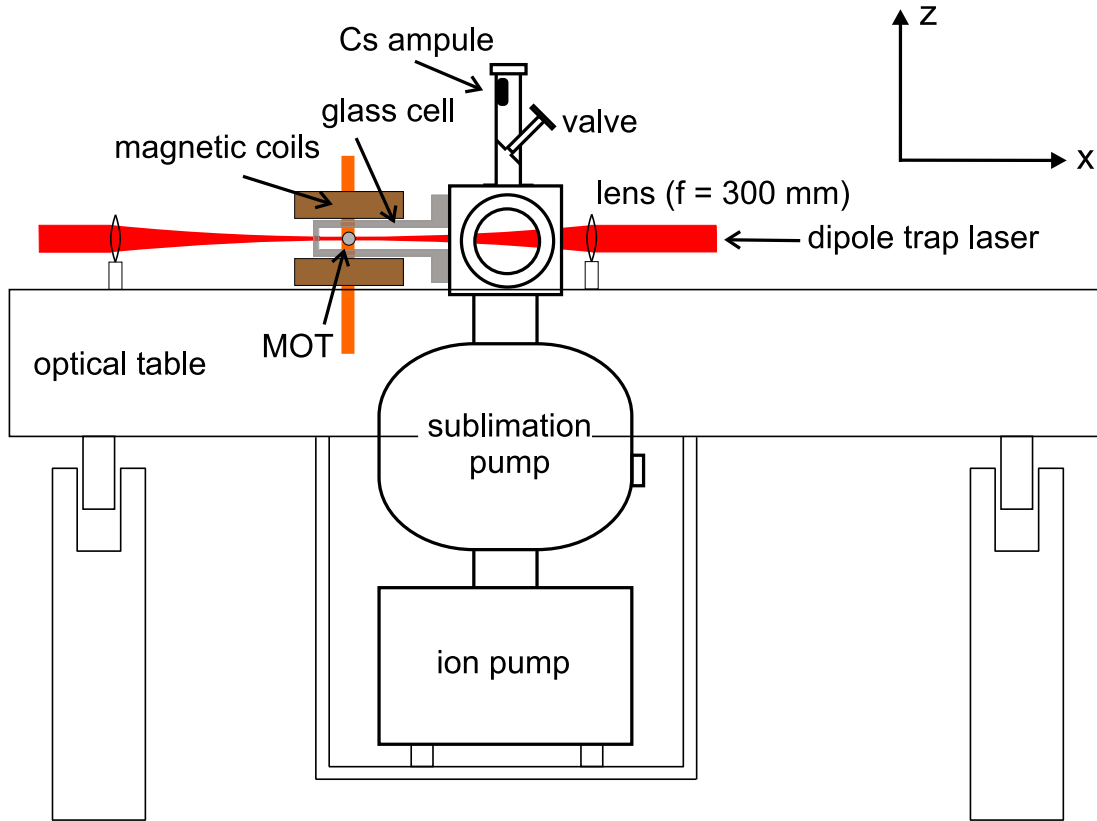


Figure 1.2: Side view of the vacuum system. A large cut-out of the optical table allows us to place the two vacuum pumps underneath the table surface. Cesium atoms are provided by a cesium reservoir which is connected to the vacuum chamber by a valve. For optimum optical access we perform all experiments in a rectangular glass cell which is attached to the vacuum system. All optical elements are set up outside the vacuum chamber.

magnetic field gradient by an order of magnitude for a time of typically $t_{\text{low}} = 10$ ms and thus temporarily increasing R_{load} [48]. Finally, we adjust t_{low} such that on average one atom is loaded into the MOT. The Poissonian nature of the atom number statistics then results in the capture of exactly one atom with a probability of 37 %.

1.1.2 Experimental setup

The details of our experimental MOT setup have been described extensively in previous theses of our group [48, 54]. Here, I only present the most important components which are relevant for this thesis.

Vacuum system

To provide for optimal optical access from all sides, we perform our experiments in a $3 \times 3 \times 12.5$ cm³ glass cell which is attached to a vacuum chamber, see Figure 1.2. A

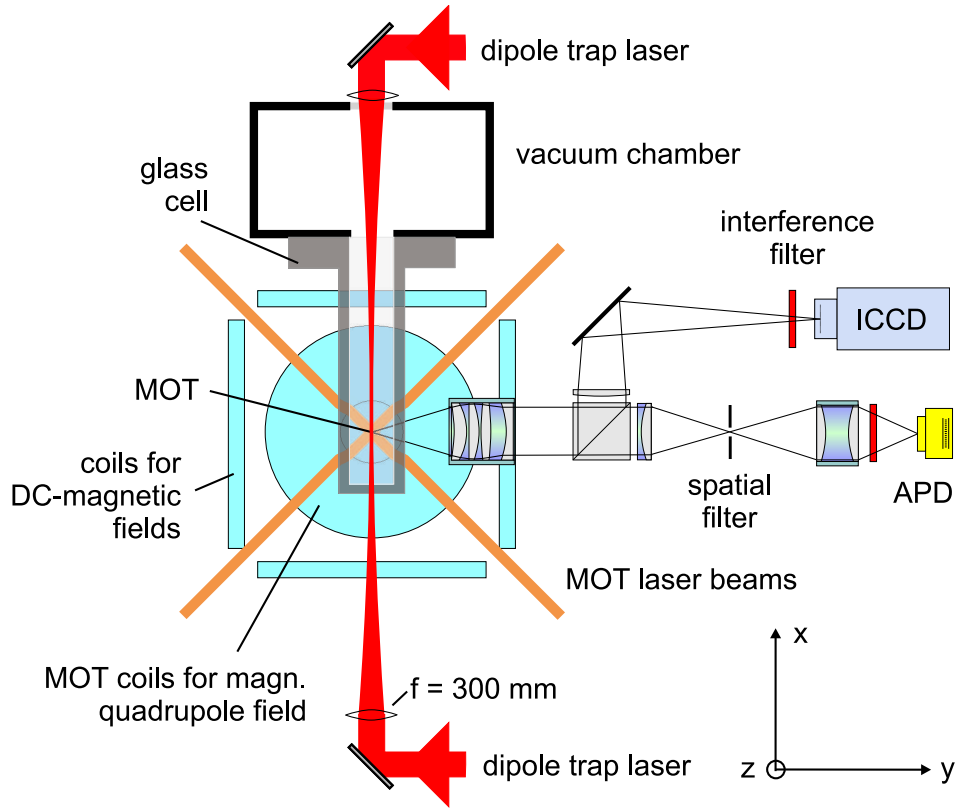


Figure 1.3: Experimental setup of MOT, dipole trap, and imaging system. Both dipole trap lasers are focussed into the MOT in the center of the glass cell. In addition to the coil pair (along z) providing the MOT quadrupole field, three pairs of orthogonal coils (the pair along z not shown) are used for compensating magnetic DC-fields and for applying guiding fields. The fluorescence light from the MOT is collected and collimated by an objective. One part is spatially and spectrally filtered and focussed onto an avalanche photodiode (APD), the other part is sent to an intensified CCD camera (ICCD).

constantly working ion pump produces an ultra-high vacuum in the glass cell with a pressure of less than 10^{-10} mbar. An additional titanium sublimation pump was only operated a few times. A reservoir containing cesium is connected to the chamber by a valve which is usually closed. Opening this valve about once every two weeks for a few minutes sufficiently raises the cesium partial pressure in the vacuum system for normal operation of our single atom MOT.

Lasers

Three pairs of orthogonal MOT cooling laser beams intersect in the center of the glass cell, see Figure 1.3. The counterpropagating beams are created by retro-reflection. Their frequency is red detuned by approximately Γ from the closed $F = 4 \leftrightarrow F' = 5$ transition of the cesium $D2$ line ($\lambda = 852$ nm), see Figure 1.4 for a level scheme. After an atom has

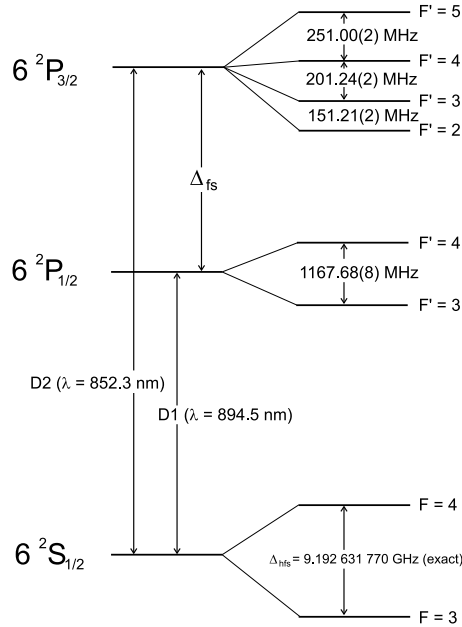


Figure 1.4: Level scheme of the cesium D-doublet.

been excited to $F' = 5$ it can only spontaneously decay to $F = 4$ and is ready to absorb the next cooling photon. However, with a slight probability of 10^{-3} it is off-resonantly excited to $F' = 4$ from where it can decay to $F = 3$. To pump the atom back into the cooling cycle we employ a repumping laser resonant with $F = 3 \leftrightarrow F' = 4$. It is shined into the MOT area along the axis of the glass cell.

Both cooling and repumping lasers are diode lasers in Littrow configuration which are actively stabilized to polarization spectroscopies. Details and further references can be found in the thesis of Wolfgang Alt [54]. The cooling laser is stabilized to the $F = 4 \leftrightarrow F' = 3 - F' = 5$ - crossover resonance of the spectroscopy, which is red detuned by 225 MHz with respect to $F = 4 \leftrightarrow F' = 5$. An acousto-optical modulator (AOM, central frequency = 110 MHz) in double pass configuration compensates for this detuning and tunes the frequency between +35 MHz and -45 MHz with respect to $F = 4 \leftrightarrow F' = 5$. The repumping laser is directly stabilized to the $F = 3 \leftrightarrow F' = 4$ resonance. Both lasers and their spectroscopies are set up on a separate optical table, and we use optical fibers to transfer the laser light to the main table.

Magnetic coils

Two water-cooled coils in Anti-Helmholtz configuration along the z axis create the quadrupole magnetic field for the MOT. They run currents of 16 A to provide a field gradient of 340 G/cm. Three orthogonal pairs of coils compensate DC-magnetic fields in three dimensions. The current supplies for the coil pairs in x and in z direction can be switched so that we can apply guiding magnetic fields during the course of an experiment.

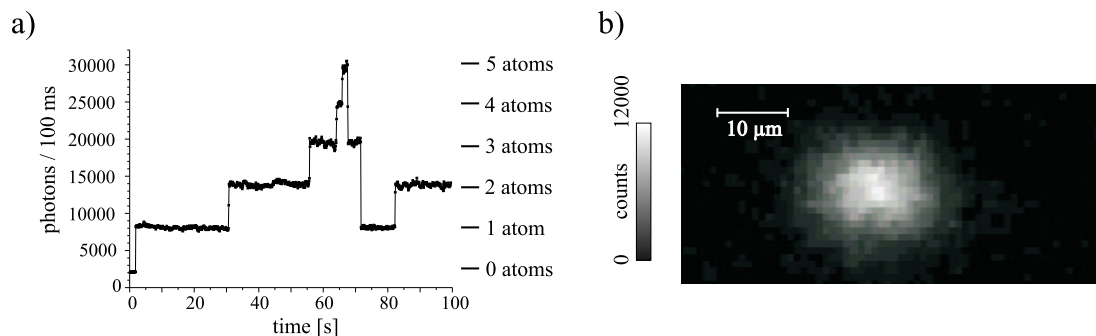


Figure 1.5: Fluorescence light from single atoms in a MOT. (a) The APD signal of the MOT fluorescence shows discrete levels. Since every trapped atom equally contributes to the overall signal we can infer the exact number of atoms. (b) The camera picture (exposure time: 1 s) of a single trapped atom reveals the size of the trapping region to be roughly $10 \mu\text{m}$ in diameter.

Computer control

Our experiments require complex sequences of laser and microwave pulses, along with controlled changing of magnetic fields, intensities and frequencies. For this purpose we use a computer control system which consists of a 32-channel digital board (National Instruments, PCI-DIO32-HS) with a time resolution of 500 ns and two buffered 8-channel D/A boards (National Instruments, PCI 6713) with analog output voltages in the range of -10 V ... +10 V and a time resolution of $2 \mu\text{s}$. The corresponding software was developed by Stefan Kuhr during his Ph.D. thesis [48].

1.1.3 Single atom detection

We use two detectors to observe the trapped atoms in the MOT, a single-photon counting avalanche photodiode (APD), which allows us to determine their exact number, and an intensified CCD camera (ICCD), which provides spatial information.

For the detection of single atoms both efficient collection of fluorescence light and minimizing stray light are essential. A custom-designed diffraction-limited objective ($\text{NA}=0.29$) collects fluorescence light from 2 % of the solid angle [24]. A beam splitter divides the collimated light to send one part to the camera and the other to the APD (EG&G, SPCM200 CD2027), see Figure 1.3. To minimize the stray light background we have wrapped the entire optical path of the imaging system in black paper and aluminum foil and blocked laser beam reflections off the glass cell. In addition, the fluorescence light is focussed through a spatial filter which consists of an aperture of $150 \mu\text{m}$ diameter. Stray light from sources outside the optical path of the fluorescence light are not transmitted through the pinhole. Finally, interference filters before both the APD and the ICCD, with a transmission of 80 % at 852 nm and 10^{-6} at 1064 nm, attenuate the stray light of our dipole trap laser.

Figure 1.5 (a) shows a typical APD signal during operation of the MOT. The fluorescence signal as a function of time reveals discrete steps which arise from the fact that every

atom trapped in the MOT contributes equally to the overall signal. Therefore, the atom number is directly inferred from the fluorescence level. The observed photon count rate per atom $R = 6 \times 10^4 \text{ s}^{-1}$ is about a factor of three larger than the remaining background light which is governed by MOT laser stray light. The required time to distinguish N from $N + 1$ atoms is determined by the ratio of the Poissonian fluctuations of the photon count rate and R . It takes $300 \mu\text{s}$ to distinguish one from two atoms with 4σ -significance [48].

An image of a single trapped atom in the MOT is presented in Figure 1.5 (b) with an exposure time of 1 s. The width of the fluorescence spot shows that the atom is confined in a region of about $10 \mu\text{m}$ diameter. Details of the characteristics of the ICCD and single atom imaging techniques are presented in Section 1.3.

1.2 A standing wave optical dipole trap

While the magneto-optical trap is a very efficient tool for cooling and trapping atoms it is not suited for preparing atoms in specific electronic states. Spontaneous emission destroys any coherent information encoded in the atoms on a timescale of tens of nanoseconds. However, the conservative potential of a dipole trap allows trapping with long coherence times. It is created by the interaction of a far-detuned laser beam with the atomic dipole moment, and the photon scattering rates are only a few photons per second.

1.2.1 Dipole potential

Classical model

To derive a simple equation for the dipole potential we consider an atom as a charged harmonic oscillator which is driven by a classical electromagnetic field $E(t) = E_0 \cos \omega t$ [40]. Since the atomic dipole moment $p(t)$ is parallel to $E(t)$, the system is described by a one-dimensional equation

$$\ddot{p}(t) + \Gamma \dot{p}(t) + \omega_0^2 p(t) = \frac{e^2}{m_e} E_0 \cos(\omega t) . \quad (1.2)$$

Here, e and m_e are the electron charge and mass, ω_0 is the atomic resonance frequency. The damping rate Γ accounts for the radiative energy loss of the dipole [55]

$$\Gamma = \frac{e^2 \omega^2}{6\pi \epsilon_0 m_e c^3} . \quad (1.3)$$

The induced atomic dipole moment is proportional to the electromagnetic field, $p = \alpha E$, so that the polarizability α can be calculated by integrating Equation (1.2):

$$\alpha(\omega) = \frac{e^2}{m_e} \frac{1}{\omega_0^2 - \omega^2 - i\omega\Gamma} . \quad (1.4)$$

The dipole potential $U_{\text{dip}}(\mathbf{r})$ is the time-averaged interaction energy between atom and field $\langle W \rangle_{\text{T}}$:

$$U_{\text{dip}}(\mathbf{r}) = \langle W \rangle_{\text{T}} = -\frac{1}{2} \langle p \cdot E \rangle_{\text{T}} = -\frac{1}{2\epsilon_0 c} \Re(\alpha) I(\mathbf{r}) . \quad (1.5)$$

It is proportional to the field intensity $I = c\epsilon_0|E_0|^2/2$ and to the in-phase component of the atomic dipole moment, $\Re(\alpha)$. Its quadrature component, $\Im(\alpha)$, is proportional to the absorbed power P_{abs} , which yields the photon scattering rate

$$R_s(\mathbf{r}) = \frac{P_{\text{abs}}(\mathbf{r})}{\hbar\omega} = \frac{\langle \dot{\mathbf{p}} \cdot \mathbf{E} \rangle_{\Gamma}}{\hbar\omega} = \frac{1}{\hbar\epsilon_0 c} \Im(\alpha) I(\mathbf{r}). \quad (1.6)$$

I can approximate Equations (1.5) and (1.6) in the regime of large detuning $|\omega - \omega_0| \gg \Gamma$:

$$U_{\text{dip}}(\mathbf{r}) = \frac{\hbar\Gamma}{8} \frac{\Gamma}{\Delta'} \frac{I(\mathbf{r})}{I_0}, \quad (1.7)$$

$$R_s(\mathbf{r}) = \frac{\Gamma}{8} \left(\frac{\Gamma}{\Delta'} \right)^2 \frac{I(\mathbf{r})}{I_0} = \frac{\Gamma}{\hbar\Delta'} U_{\text{dip}}(\mathbf{r}). \quad (1.8)$$

Here, I have introduced the saturation intensity $I_0 = 11 \text{ W/m}^2$ in the case of cesium, and:

$$\frac{1}{\Delta'} = \frac{1}{\omega - \omega_0} + \frac{1}{\omega + \omega_0}. \quad (1.9)$$

In the regime of red-detuning, $\Delta' < 0$, the dipole potential is negative (1.7) so that an atom is attracted to regions of high intensities. To minimize the photon scattering rate (1.8) it is favourable to choose a large detuning while compensating the decreasing potential depth by higher intensities.

The classical model provides a simple result for the dipole potential. However, it fails to take into account the atomic multi-level structure and the polarization of the electromagnetic field. A more suitable, perturbative description of the interaction of a classical electro-magnetic field with a multi-level atom is given in Appendix A and yields the AC-Stark shift (also referred to as ‘‘light shift’’) of every atomic level. It turns out that the individual light shift of the Zeeman sublevels depends on the polarization of the electromagnetic field.

Standing wave trapping field

Since the depth of the dipole potential is proportional to the intensity, a variety of trap configurations can be designed by properly creating the desired intensity pattern of the trapping laser beam. In our case, we use a standing wave configuration which consists of two focussed counterpropagating laser beams with parallel linear polarization. Their interference pattern is sinusoidally modulated and thus creates a series of potential wells for the atoms.

The intensity profile of the two interfering beams with a waist w_0 and total power P is

$$I(\mathbf{r}) = I(x, \rho) = I_{\text{max}} \frac{w_0^2}{w^2(x)} e^{-\frac{2\rho^2}{w^2(x)}} \cos^2(kx), \quad (1.10)$$

with the beam radius $w(x) = w_0(1 + x^2/z_R^2)^{1/2}$, the Rayleigh range $z_R = \pi w_0^2/\lambda$, the peak intensity $I_{\text{max}} = 4P/\pi w_0^2$, and $\rho = \sqrt{y^2 + z^2}$. Small corrections due to the wave-front curvature and Gouy phase shift of the Gaussian beams have been neglected. Using

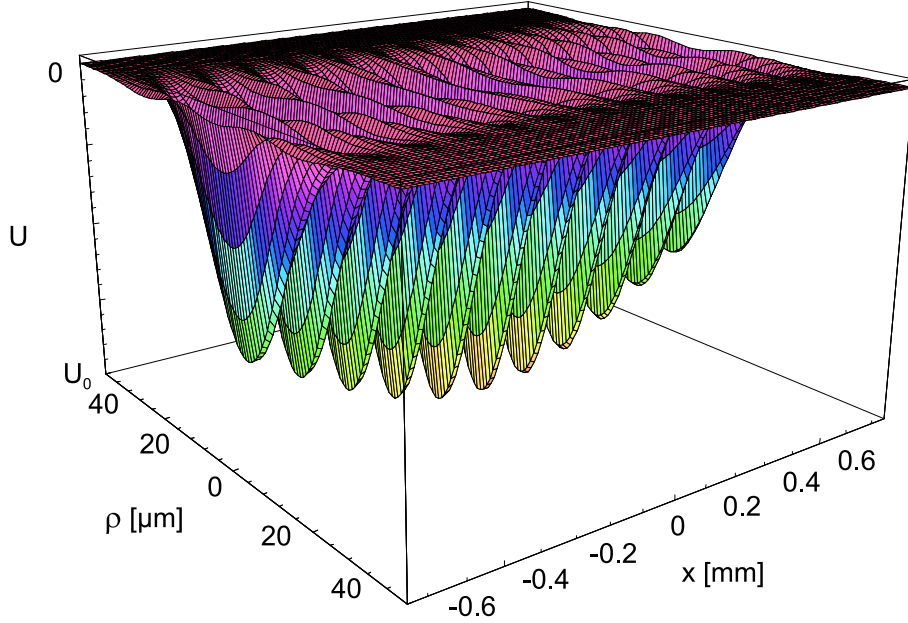


Figure 1.6: Three-dimensional view of the standing-wave trapping potential for $w_0 = 19 \mu\text{m}$. In x -direction, the wavelength has been stretched by a factor of 250 to visualize the individual potential wells.

Equation (A.10) we get the resulting dipole potential:

$$U(\rho, x) = -U_0 \frac{w_0^2}{w^2(x)} e^{-\frac{2\rho^2}{w^2(x)}} \cos^2(kx), \quad (1.11)$$

with a maximum trap depth of

$$U_0 = \frac{\hbar\Gamma}{8} \frac{I_{\text{max}}}{I_0} \frac{\Gamma}{\Delta'_{\text{eff}}}, \quad (1.12)$$

and the effective detuning Δ'_{eff} defined in Equation (A.11). Figure 1.6 shows the trapping potential in the (x, ρ) -plane.

Trapped atoms oscillate in the potential wells which can be approximated harmonically in both axial and radial directions. A Taylor expansion of Equation (1.11) at $(\rho, x) = (0, 0)$ yields for the respective oscillation frequencies:

$$\Omega_{\text{ax}} = \frac{2\pi}{\lambda} \sqrt{\frac{2U_0}{m}} \quad (1.13a)$$

$$\Omega_{\text{rad}} = \frac{2}{w_0} \sqrt{\frac{U_0}{m}}. \quad (1.13b)$$

1.2.2 Experimental setup of the dipole trap

Dipole trap laser

We use a commercial, arclamp-pumped Nd:YAG laser (Quantronix/Excel Technologies, Model 112) with a wavelength of $\lambda = 1064$ nm and a maximal output power of 11 W as the dipole trap laser. Brewster windows and pinholes inside the two-mirror resonator ensure linear polarization and a clean TEM₀₀-transverse mode of the output beam. By inserting an etalon into the resonator we reduce the number of longitudinal laser modes to about 5 with a spacing of 196 MHz. The resulting coherence length of 30 cm ensures a well-modulated interference pattern of the standing wave inside the vacuum chamber.

Alignment

The output beam is split into two beams which are focussed to the same point from opposite sides, see Figure 1.3. Good overlap between the foci of both laser beams and the MOT are essential for efficient atom transfer between the two traps. In order to carefully align each dipole trap laser beam onto the MOT we minimize the fluorescence from atoms trapped in the MOT. The dipole trap laser induces a light shift of the cooling transition which increases the detuning with respect to the MOT cooling laser, thus resulting in a decrease of fluorescence. For fine-tuning of this alignment we move the last mirrors before the vacuum chamber with piezo-elements.

Trap parameters

We typically work with a total Nd:YAG laser power of $P = 2$ W in the vacuum chamber. Telescopes and focussing lenses of the trapping laser beams are chosen to focus both laser beams to a waist of $w_0 = 16$ μm . These parameters result in a trap depth of $U_0 = 2.6$ mK according to Equation (1.12). More reliable values for the actual trap depth and beam waists can be inferred by measuring the oscillation frequencies of the trap. Eqs. (1.13a,1.13b) yield:

$$U_0 = \frac{m}{2} \left(\frac{\lambda \Omega_{\text{ax}}}{2\pi} \right)^2 \quad (1.14a)$$

$$w_0 = \frac{2}{\Omega_{\text{rad}}} \sqrt{\frac{U_0}{m}}. \quad (1.14b)$$

To measure the trap frequencies we modulate the trap depth by modulating the laser power using the AOMs. Parametric heating causes atom losses as soon as the modulation frequency equals twice their oscillation frequency [54]. The measured values of $\Omega_{\text{ax}} = 2\pi \cdot (265 \pm 8)$ kHz ($P = 1.56$ W) and $\Omega_{\text{rad}} = 2\pi \cdot (3.6 \pm 0.2)$ kHz ($P = 1.8$ W) yield a trap depth of $U_0 = 0.8 \pm 0.02$ mK at $P = 2$ W and a beam waist of $w_0 = 18.9 \pm 1.1$ μm assuming 100 % contrast. This result is confirmed by an independent optical measurement of the waist size which yields a value of $w_0 = 19.5 \pm 0.9$ μm . The scattering rate is directly inferred from the trap depth and amounts to $\Gamma_{\text{sc}} = U_0 \Gamma / \hbar \Delta'_{\text{eff}} = 9$ s⁻¹.

The significant discrepancy compared to the calculated trap depth can partly be explained by aberrations and clipping of the large (diameter $2w = 17$ mm) collimated beams at the 1-inch mirrors and lenses before the final focussing lens. As confirmed by an optical ray tracing simulation they cause an increase of the waist by the observed amount resulting in a decrease of the trap depth by more than 30 % to $U_0 = 1.8$ mK [56]. Furthermore, they cause an additional decrease of the trap depth due to losses of a fraction of the laser power in diffraction rings. Finally, the reduction of the standing wave interference contrast by imprecise lateral alignment of the beams and imperfect axial overlap of the beam foci reduce our measured axial oscillation frequency from which we calculate the trap depth.

1.2.3 Transfer of a single atom between MOT and dipole trap

We transfer an atom from the MOT into the dipole trap by operating both traps simultaneously for a few tens of milliseconds. Figure 1.7 shows the fluorescence signal of a single trapped atom in the MOT. When the MOT lasers are switched off, this signal decreases to the stray-light level of the Nd:YAG laser of typically 200 photons/100 ms. After a storage time of 1 s, the atom is transferred back into the MOT by reversing the procedure described above. The observed fluorescence level after switching off the dipole trap laser indeed reveals the presence of the atom.

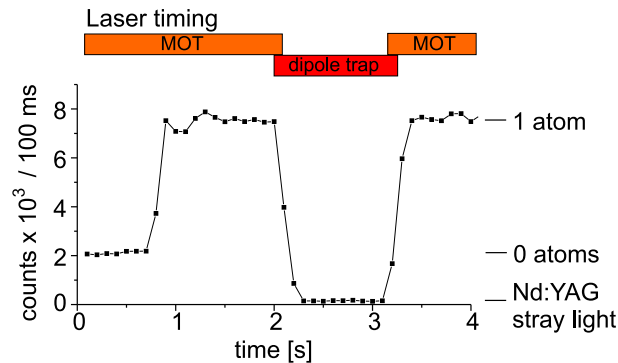


Figure 1.7: Transfer of a single atom between MOT and dipole trap. Once the atom has been transferred to the dipole trap, the recorded fluorescence signal drops to the stray-light background. Transfer back to the MOT reveals the presence of the atom by observing its fluorescence.

The transfer efficiency between the traps has been measured to be 97.2 ± 0.8 % [48]. However, in many experiments even higher efficiencies were accomplished, see Section 2.3.2. The lifetime of atoms in the dipole trap is limited to 25 ± 3 s by background gas collisions [41, 57].

1.3 Imaging single atoms

We have recently managed to continuously image a single neutral atom in a dipole trap for more than one minute [25]. Our capability to obtain spatial information of the trapped

atom provides a powerful tool for the manipulation of all atomic degrees of freedom. It allows us to precisely control the absolute position of trapped atoms [58]. Furthermore, our ability to spatially resolve a string of trapped atoms is a prerequisite for the individual addressing of the atoms, see Chapter 2 and Reference [22].

1.3.1 Properties of the intensified CCD camera

Operating principle

To image the trapped atoms, we use an intensified CCD camera (Roper Scientific, PI-MAX:1K), see section 1.1.3. The GaAs photocathode of the image intensifier (Roper Scientific, GEN III HQ) has a quantum efficiency of $\eta_{\text{ICCD}} = 12 \pm 2\%$ at 852 nm which we determined by comparing the detected single atom fluorescence rate with the APD signal. Since the fluorescence light is unpolarized, the polarizing beam splitter in the optical path of the imaging system, see Figure 1.3, equally distributes the collected fluorescence photons among the APD and the ICCD. From the known quantum efficiency of the APD of 50 % we infer η_{ICCD} . The discrepancy with respect to the specified value of $\eta_{\text{ICCD}} = 30\%$ has remained unclear so far.

Each photoelectron from the photocathode is amplified by a multi-channel electron multiplier to about 10^6 electrons. They produce light on a phosphorous screen which is guided to the low-noise CCD chip by an optical fiber bundle. The CCD chip consists of an array of 1024×1024 pixels, with each pixel having a size of ($13 \mu\text{m} \times 13 \mu\text{m}$). After exposure, the desired part of the chip is read out by a computer. This operation takes between 100 ms and 10 s depending on the size of the region to be read out.

Signal and Noise

A single photoelectron emitted from the photocathode produces a photon burst resulting in 390 ± 180 counts on the CCD chip concentrated in a 3×3 pixel area with 50 % in the central pixel. This signal allows us to reliably detect single photons well above the readout noise floor of the camera of 90 ± 9 counts/pixel rms. The CCD dark current amounts to only 1 count per pixel per second.

A further noise contribution arises from thermal electrons released from the photocathode. About 16000 thermal electrons are emitted per second so that on average each camera pixel is hit by the corresponding photon burst once per minute.

1.3.2 Imaging system

Our imaging system (Figure 1.3) consists of the diffraction limited objective (see Section 1.1.3) with a working distance of 36 mm. The collimated fluorescence light is focussed onto the photocathode of the ICCD with a lens of focal length $f = 500$ mm. The resulting magnification of 14 was chosen such that each camera pixel roughly corresponds to about $1 \mu\text{m}^2$ at the position of the MOT. A more accurate calibration of the magnification by comparing images of a controllably transported single atom (see Section 1.4) yields a cor-

responsiveness of $\mu_{\text{ICCD}} = 0.937 \pm 0.008 \mu\text{m}/\text{pixel}$.

The resolution of our imaging optics is given by the Airy disk radius of its point spread function $r_{\text{PSF}} = 1.8 \mu\text{m}$ [24], calculated from the numerical aperture of the objective of $NA = 0.29$ [59]. We obtained further information on our imaging resolution by analyzing atom images, see 1.3.4.

1.3.3 Illumination of single atoms in the dipole trap

Since an atom in the MOT emits fluorescence photons due to near-resonant excitation by the MOT lasers, an image of the atom can be taken by exposing the camera to its fluorescence light. An atom stored in the dipole trap hardly scatters any photons from the dipole trap laser so that imaging requires additional illumination by resonant or near-resonant light. However, the photon recoils of energy $E_r = \hbar^2 k^2 / 2m$ will heat the atom. In a trap of depth $U_0 = 1 \text{ mK}$, an atom initially at rest in the bottom of the potential well will be heated out of the trap after scattering $n_{\text{heat}} = U_0 / 2E_r = 5600$ photons where the factor of 2 takes into account that one scattering process causes two recoils. Considering the 2 % collection efficiency of the fluorescence light and the quantum efficiency of the ICCD, only 7 photons would be detected until the atom is lost. While this is enough to detect the atom, a non-destructive illumination process with a larger signal is certainly preferable.

We therefore illuminate the trapped atom by an optical molasses consisting of the MOT cooling and repumping lasers which cool the atom in the dipole trap while up to 120000 photons per second are scattered. However, finding good laser parameters for illumination was only possible after several technical improvements. We found that unless the radiation pressure of the counterpropagating molasses beams is carefully balanced, the trapped atoms jump between different potential wells during illumination. We therefore thoroughly centered the cooling laser beams onto the MOT by laterally scanning each beam to maximize the single atom fluorescence rate. In addition, we adjusted the intensities of the counterpropagating beam pairs to be equal within 10 %. Finally, we ensured the laser polarization to contain at least 99.5 % of their power in the correct circularity to guarantee a reasonably pure $\sigma^+ - \sigma^-$ configuration.

1-D molasses cooling

In a simplified model, we studied the presence of Doppler and sub-Doppler cooling mechanisms for atoms in a standing-wave dipole trap being illuminated by a 1-D optical molasses [60]. To experimentally investigate the cooling effects in this system, we measured the temperature of single trapped atoms after illumination by one pair of horizontal MOT cooling laser beams and the MOT repumping laser beam. Adiabatically lowering the dipole trap depth to $10 \mu\text{K}$ to let hot atoms escape and studying the atom survival probability has proven to be an effective temperature measurement at the level of few atoms [54, 57]. A larger survival probability indicates colder atoms. This quantity is shown in Figure 1.8 as a function of the cooling laser detuning Δ_c with respect to the unperturbed $F = 4 \leftrightarrow F' = 5$

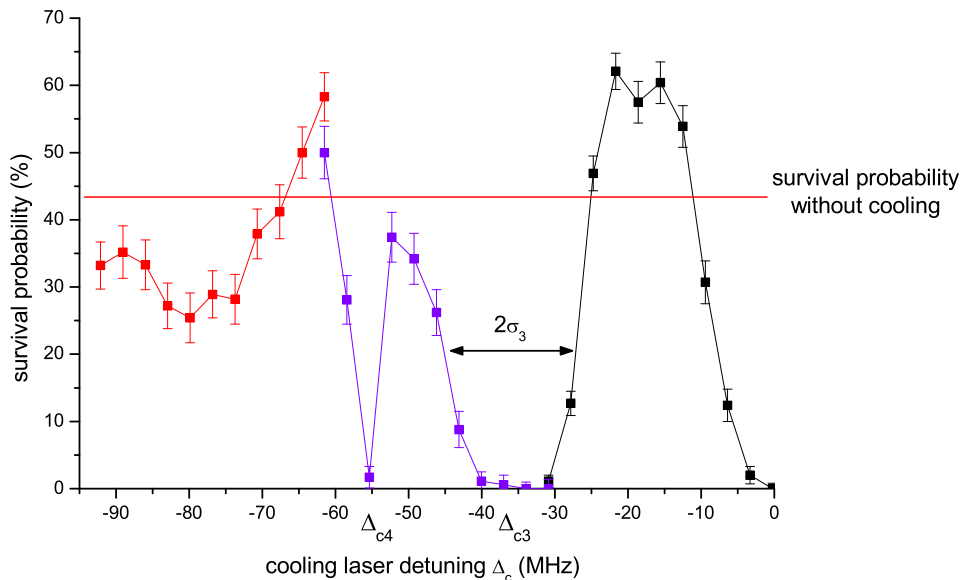


Figure 1.8: 1-D molasses cooling in the dipole trap. The atom survival probability shows a regime of efficient cooling for a cooling laser detuning between -10 and -25 MHz. The molasses illumination causes heating of the atoms at detunings around -37 MHz and -55 MHz indicated by a drop of the survival probability to zero. This heating effect is due to multi-photon resonances between the optical molasses lasers and the dipole trap laser.

resonance at a cooling laser power of $115 \mu\text{W}$ per beam corresponding to a saturation parameter of $s_0 = I/I_0 = 10$, and a dipole trap depth of $U_0 = 0.7$ mK. The horizontal bar at 42 % in Figure 1.8 indicates the typical atom survival probability without molasses cooling after transfer from the MOT into the dipole trap and lowering of the trap depth. Our measurement shows that for $\Delta_c/2\pi \approx -20$ MHz the molasses illumination indeed provides further cooling of the atoms after their transfer from the MOT.

Multi-photon resonances

However, the observed cooling regime is narrow and drops off quickly for larger detuning. Notably, there are two regions of cooling laser detuning for which the measured survival probability drops to zero. We attribute these to multi-photon resonances which pump the atom out of the cooling cycle.

The narrow resonance at $\Delta_{c4}/2\pi = -55$ MHz is caused by a four-photon process which resonantly connects the two hyperfine ground states. As shown in Figure 1.9 (b), the cooling and repumping transition are coupled by two neighboring Nd:YAG laser modes spaced at 196 MHz. There are three effects that furnish experimental evidence to support this conclusion. First, the resonance condition $|\Delta_{c4}|/2\pi = 251 \text{ MHz} - 196 \text{ MHz} = 55 \text{ MHz}$

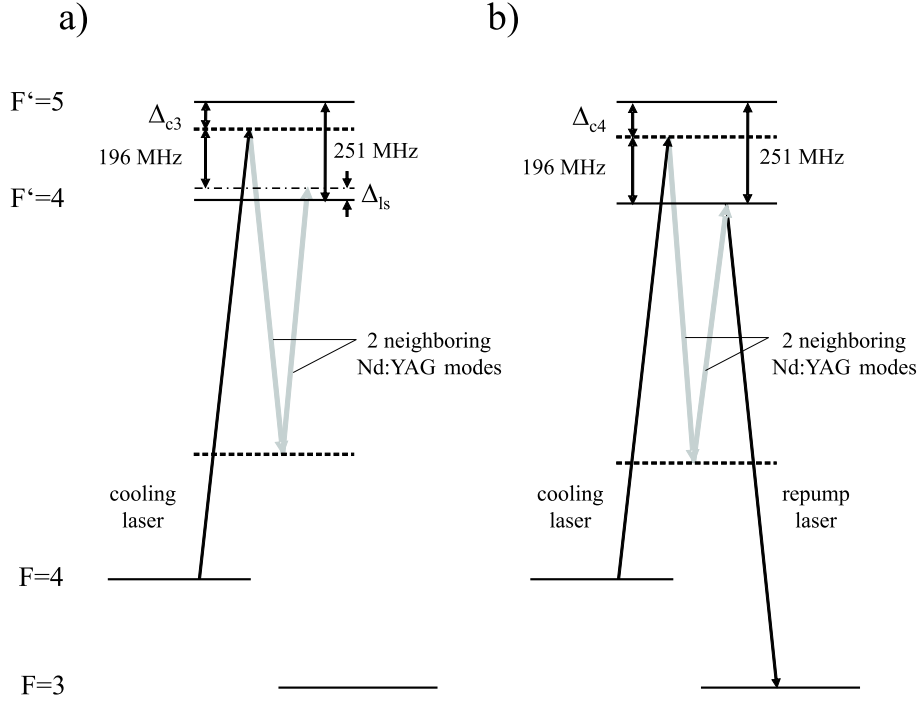


Figure 1.9: Three- and four-photon resonances during illumination in the dipole trap. a) Two neighboring Nd:YAG modes spaced at 196 MHz connect the detuned cooling laser resonantly with the light-shifted $F' = 4$ state and pump the atom out of the closed cooling cycle between $F = 4$ and $F' = 5$. Similarly, at a different cooling laser detuning (b), cooling and repumping laser couple the two ground states via a four-photon resonance with two Nd:YAG modes and inhibit the desired cooling process.

confirms the measured position of the resonance. It is independent of the light shift of the D2 transition Δ_{ls} which we checked by measuring the spectrum for different dipole trap laser powers. Second, the resonance disappears when we switch off the repumping laser of the optical molasses. Finally, the width of the resonance is smaller than Γ and is thus not determined by a spontaneous emission process but rather by the line widths of the molasses lasers.

The other resonance at $\Delta_{c3}/2\pi \approx -37$ MHz seems to be caused by a three-photon process, again involving two Nd:YAG laser modes, which resonantly connect the cooling laser to the light-shifted excited $F' = 4$ level, see Figure 1.9 (a). Here, the corresponding resonance condition $|\Delta_{c3}|/2\pi = 251 \text{ MHz} - 196 \text{ MHz} - \Delta_{ls}/2\pi = 37 \text{ MHz}$ can be used to directly infer $\Delta_{ls}/2\pi = 18 \text{ MHz}$ from the spectrum. We confirmed that the position of this resonance linearly depends on Δ_{ls} by performing the same measurement for different dipole trap laser powers. The resonance width is determined by the spontaneous decay rate to the ground state Γ and by the Zeeman sublevel dependent light shift of the excited state w_{ls} , see Appendix A. The theoretically expected values yield $\Delta_{ls}/2\pi = 14 \text{ MHz}$ for the transition light shift, which is calculated from the trap depth, and $2\sigma_3 = 2\sqrt{\Gamma^2 + w_{ls}^2} = 17 \text{ MHz}$

for the width of the resonance. Their good agreement with the values obtained from the spectrum confirm that our model describes the observations reasonably well.

Optimization of cooling parameters

Each day we run an experiment we optimize the trap depth and the optical molasses for efficient cooling. Starting from the cooling parameter regime identified above, we fine-tune these parameters such that we no longer observe hopping of the atoms between different potential wells while we maximize the photon scattering rate. As a second criterion, we minimize the radial width of a single atom image, which is a measure for the energy of the atom, see Section 1.3.4. At a trap depth of 0.8 mK, we typically set the cooling laser beams to a power of 80 μW per beam, a waist size of $w_0 = 1$ mm ($s_0 = 11.5$) and a detuning of $\Delta_c/2\pi = -5$ MHz. Also, we found that the fluorescence rate can be increased by employing a 3-D rather than a 1-D optical molasses without reducing the cooling efficiency.

The undesired side effects of the observed three- and four-photon resonances involving the trapping laser modes and the optical molasses, significantly narrow the regime in which cooling can be achieved. More importantly, slight changes of the trap depth due to decreasing intensity and pointing drifts of the two trapping laser beams result in a drift of the three-photon resonance which can turn the cooling regime into a heating regime within several hours. We therefore perform this optimization every four to six hours during the course of an experiment. Since the reduction of the cooling efficiency is caused by the multi-mode character of the Nd:YAG laser, we have bought and set up a single frequency Yb:YAG laser at a wavelength of 1030 nm which will serve as a dipole trap laser in future experiments.

1.3.4 Images of single trapped atoms

Imaging of an atom in the MOT

Under continuous illumination the fluorescence light of a single atom in the MOT produces $R_{\text{MOT}} = 6400$ photoelectrons/s on the photocathode. Figure 1.10. (a) shows an image of a single atom trapped in the MOT with an exposure time of 1 s. We determine the size (σ_x, σ_z) and the position (x_0, z_0) of the MOT by binning the pixels of the picture in the vertical and horizontal directions after suitably clipping the image to minimize the background noise. Then we fit the resulting histograms with Gaussians:

$$I(x) = B + A \exp\left(-\frac{(x - x_0)^2}{2\sigma_x^2}\right), \quad I(z) = B + A \exp\left(-\frac{(z - z_0)^2}{2\sigma_z^2}\right). \quad (1.15)$$

Here, the MOT has a $1/\sqrt{e}$ -width of $\sigma_x(\text{MOT}) = 5.3 \pm 0.1$ μm in the horizontal and of $\sigma_z(\text{MOT}) = 4.1 \pm 0.1$ μm in the vertical direction. The asymmetry of the MOT size in vertical and horizontal direction is caused by the fact that the magnetic field gradient along the z direction is twice as large as in x direction.

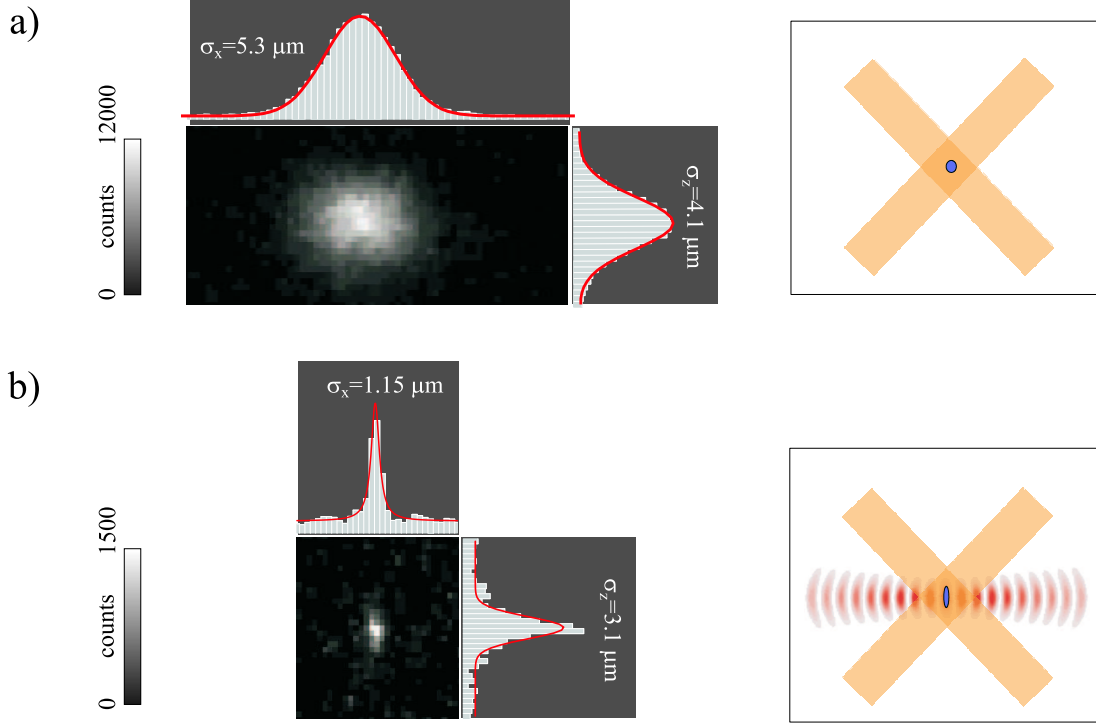


Figure 1.10: (a) Image of a single trapped atom in the MOT with an exposure time of 1 s. This is the same image already depicted in Figure 1.5 (b). (b) Image of a single trapped atom in a potential well of the dipole trap under continuous illumination with a 3-D optical molasses (exposure time: 0.5 s). On the right side, the respective laser configurations are shown.

A trajectory of an atom in the MOT corresponds to a trace of sequentially recorded single photon events. In order to reconstruct the atomic trajectory with a spatial resolution at the diffraction limit of our optics, the mean spacing between consecutive photons should not exceed the diffraction limited spot size r_{PSF} . This condition results in an upper limit of the atomic velocity of $v_{\text{max}}^{\text{d}} = r_{\text{PSF}} \cdot R_{\text{MOT}} = 11.5 \text{ mm/s}$. This number is much smaller than the Doppler velocity $v_{\text{D}} = 9 \text{ cm/s}$ of a cesium atom in a MOT. The trajectory of an atom moving at velocity v_{D} can therefore not be reconstructed at full spatial resolution. However, to only detect the motion of an atom from one to another side of the MOT, the upper limit for the atomic velocity is $v_{\text{max}}^{\text{g}} = 2\sigma_z(\text{MOT}) \cdot R_{\text{MOT}} = 5 \text{ cm/s}$. This number is close to the Doppler velocity of 9 cm/s, and it seems feasible to resolve such motion in future experiments. A similar experiment to reveal the atom motion within a MOT has been performed using the previous version of our apparatus by analyzing photon correlations of a single trapped atom [61].

Imaging of an atom in the dipole trap

In order to image an atom in the dipole trap we illuminate it with the optical molasses. Figure 1.10 (b) shows such an image with an exposure time of 0.5 s. The observed fluorescence spot corresponds to about 70 detected photons. From a sample of 10 images we infer that the trapping region has a width of $\sigma_z(\text{DT}) = 3.1 \pm 0.5 \mu\text{m}$ in the radial direction of the dipole trap, which is considerably smaller than the trap radius $w_0 = 19 \mu\text{m}$. This indicates that the energy of the atom is much smaller than the trap depth and that the atom is cooled during illumination.

The axial width of the fluorescence spot $\sigma_x(\text{DT}) = 1.15 \pm 0.15 \mu\text{m}$, however, exceeds the axial confinement of the trapped atom which is a fraction of the period of the dipole potential of $\lambda/2 = 532 \text{ nm}$. We can therefore use $\sigma_x(\text{DT})$ to determine the actual resolution of our imaging system. It is given by the diffraction-limited resolution of our imaging optics on the one hand and the internal blur of the ICCD on the other hand. To estimate a value for the first limit, we consider the image of an ideal point source. It is given by a point spread function whose Airy disk radius equals $r_{\text{PSF}} = 1.8 \mu\text{m}$ for our objective (NA=0.29), see 1.3.2. Following a similar procedure as for a real atom image, we integrate this point spread function along one dimension and determine the $1/\sqrt{e}$ -radius of the resulting function to $\sigma_{\text{diff}} = 0.6 \mu\text{m}$. We measure the internal blur of the ICCD by analyzing light spots produced by thermal photoelectrons. Their Gaussian intensity distribution has an average half-width of 1.13 ± 0.02 pixels corresponding to $\sigma_{\text{ICCD}} = 1.06 \pm 0.02 \mu\text{m}$ [25]. Combining both values yields $\sigma_{\text{total}} \approx \sqrt{\sigma_{\text{diff}}^2 + \sigma_{\text{ICCD}}^2} = 1.2 \mu\text{m}$ which agrees with the measured value of $\sigma_x(\text{DT}) = 1.15 \pm 0.15 \mu\text{m}$. An increase of the optical magnification of our imaging system would reduce the relative contribution of the internal blur of the ICCD to the total resolution of our imaging system. For example, doubling the magnification would cause σ_{ICCD} to correspond to only $0.53 \pm 0.01 \mu\text{m}$, effectively decreasing σ_{total} to $0.8 \mu\text{m}$. This improvement could easily be implemented for future experiments.

The axial width of a single atom image effectively measures the resolution of our imaging system. We can therefore give a more accurate value for the radial extension of the trapping region σ_{rad} by deconvoluting the radial intensity distribution of the image with the axial one:

$$\sigma_{\text{rad}} = \sqrt{\sigma_z^2 - \sigma_x^2} = 2.9 \pm 0.6 \mu\text{m}. \quad (1.16)$$

When the radial oscillation frequency Ω_{rad} of the trap is known, the temperature of the atom can be extracted from σ_{rad} [54]. The radial width of the atom image therefore serves as a valuable signal to minimize the temperature of the trapped atom.

Imaging of a string of atoms

Figure 1.11 shows an image of a string of five atoms in the dipole trap. Each atom is trapped in a separate well. The average spacing between neighboring atoms is roughly $10 \mu\text{m}$ in this case so that on average 20 potential wells between them are unpopulated. The minimum separation required to resolve two neighboring atoms, can be defined according to the Rayleigh criterion which is usually applied to determine the resolution of

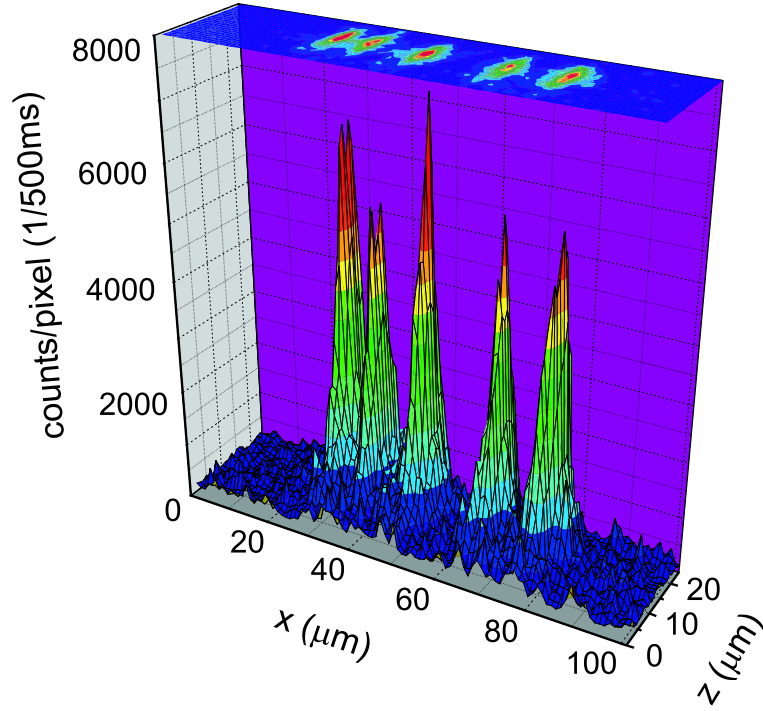


Figure 1.11: Image of a string of five trapped atoms. The atoms are trapped in separate potential wells and have an average separation of $10 \mu\text{m}$.

microscopes and telescopes. It states that the sum of the two intensity profiles must drop to at least $8/\pi^2$ of their maximum value in between the two maxima [62]. For our case this minimum separation equals $3 \mu\text{m}$ so that we can resolve two atoms as long as they are separated by 6 or more potential wells.

After transfer of the atoms from the MOT, their positions are distributed over the MOT trapping region of diameter $2\sigma_x(\text{MOT}) = 11 \mu\text{m}$. Thus, for more than two atoms, the pairwise atom separation is usually not sufficiently large to optically resolve all atoms. In order to spread their spatial distribution, we use the 1-D time-of-flight method and switch off one arm of the dipole trap for $t_{\text{off}} = 1 \text{ ms}$. During this time the atoms freely expand along the trap axis. Since the laser beam is not switched off instantaneously but ramped to zero within 1 ms, which is adiabatic with respect to the axial oscillation frequency, the atoms are adiabatically cooled from Doppler temperature T_D to $T_D/10$ [54]. Their average velocity along the trap axis is therefore $v_D/\sqrt{10}$ so that the atom distribution increases to $\sigma_{\text{tof}} = \sqrt{(t_{\text{off}}v_D)^2/10 + \sigma_x(\text{MOT})^2} = 30 \mu\text{m}$ before we switch back to the standing wave configuration.

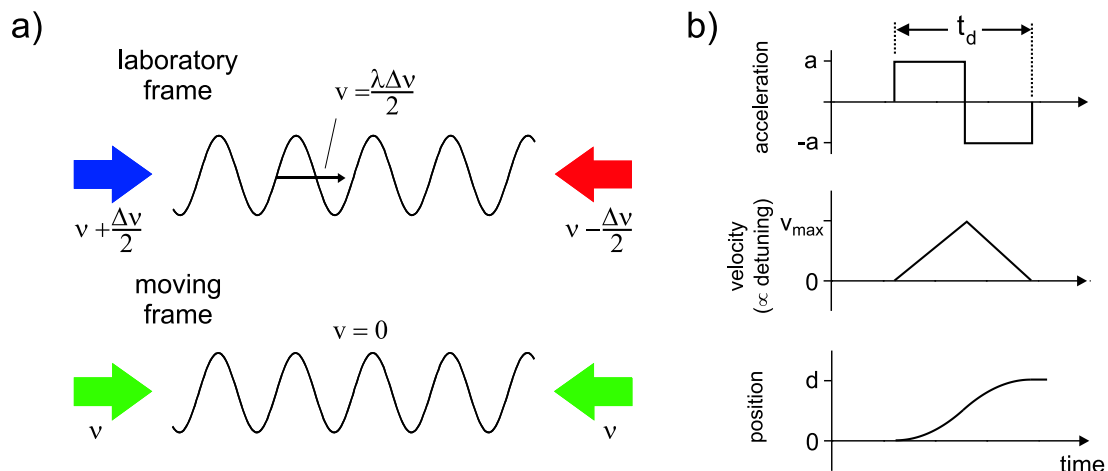


Figure 1.12: Working principle of the optical conveyer belt. (a) If the counterpropagating beams are detuned with respect to each other, the reference frame in which both beams are Doppler shifted to the same frequency is moving at the velocity v . (b) In order to transport an atom over the distance d , we expose it to constant acceleration and deceleration.

1.4 An optical conveyer belt

To precisely control the position of an atom we use an optical conveyer belt [14, 23]. This device was designed to transport a desired number of atoms into the mode of an optical high-finesse resonator in a controlled manner. There they could interact via the exchange of single photons. This is a key technique for the implementation of a quantum logic gate. Combining this tool with our imaging techniques, we demonstrated the first continued observation of controlled single atom transport [25].

1.4.1 A moving standing wave

The standing wave configuration of our dipole trap is well suited to transport trapped atoms. A mutual detuning of the counter-propagating beams by $\Delta\nu = \nu_2 - \nu_1$ will cause the standing wave structure to move at the velocity $v = \lambda\Delta\nu/2$. This can be seen by considering the Doppler shift which compensates this detuning in the reference frame moving at v , see Figure 1.12 (a). The time-dependent dipole potential

$$U(x, \rho, t) = -U_0 \frac{w_0^2}{w^2(x)} e^{-\frac{2\rho^2}{w^2(x)}} \cos^2(\pi\Delta\nu t - kx) \quad (1.17)$$

can therefore be used to transport trapped atoms along the dipole trap axis.

In order not to lose an atom during transport, it is important to smoothly accelerate and decelerate the potential. A simple way of transporting it over a desired distance d during the time t_d is to uniformly accelerate it at a during the first half of the time interval followed by a uniform deceleration at $-a$ during the second half. The velocity changes from 0 to $v_{\max} = at_d/2$ and back to 0 during this time, see Figure 1.12 (b).

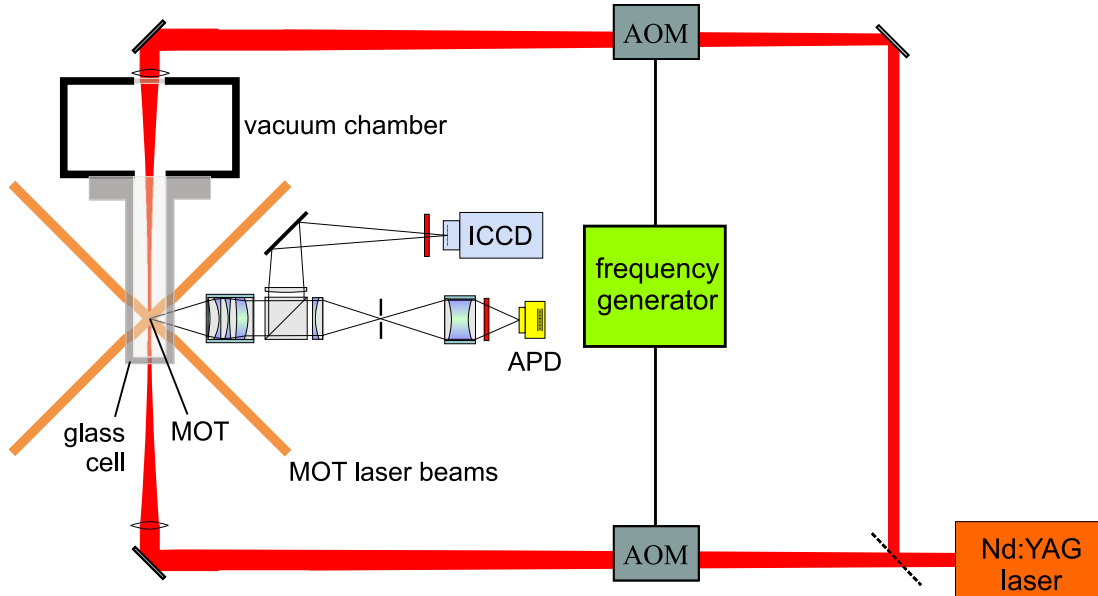


Figure 1.13: Experimental setup of the optical conveyor belt. Each beam of the standing-wave dipole trap is frequency shifted by an acousto-optical modulator (AOM). Both AOMs are driven by a phase-synchronous dual frequency RF-generator.

Experimental implementation

To implement this scheme experimentally, we installed an acousto-optical modulator (AOM) in each beam of the dipole trap, see Figure 1.13. They are both set up in double pass configuration to compensate beam walk-offs during frequency shifts. For the stationary standing wave dipole trap both AOMs are operated at the same frequency of 100 MHz. For the transport it is essential to change their frequency difference in a phase-continuous way, since their relative phase is directly translated to the spatial phase of the dipole trap. Any phase discontinuity could lead to the loss of the atom. We therefore use a custom built dual frequency synthesizer (APE Berlin, DFD 100) which drives both AOMs and performs phase-continuous frequency sweeps as programmed via an RS232 interface. However, we found that remaining phase fluctuations of the two RF outputs on the order of 10^{-3} rad cause heating of the trapped atoms and reduce the lifetime in the trap from 25 s (see Section (1.2.3)) to about 3 s [57].

Using this setup we can transport a single atom over a distance as large as 1 cm with an efficiency of 80 % [14]. Since we monitor their relative phase and thus the total distance in units of λ by heterodyning the two AOM driving frequencies, we control this distance with an accuracy much smaller than $1 \mu\text{m}$. The maximum transportation distance is determined by the divergence of the Gaussian dipole trap laser beam. With increasing distance from the focus, the trap depth decreases. At a distance of 1.5 cm, gravity is stronger than the radial dipole force and pulls the atom out of the trap [23]. The minimum time required for a transport is limited by the maximum possible acceleration. If the accelerating force becomes stronger than the axial dipole force at typically $a_{\text{max}} = 5 \times 10^5 \text{ m/s}^2$ the atom

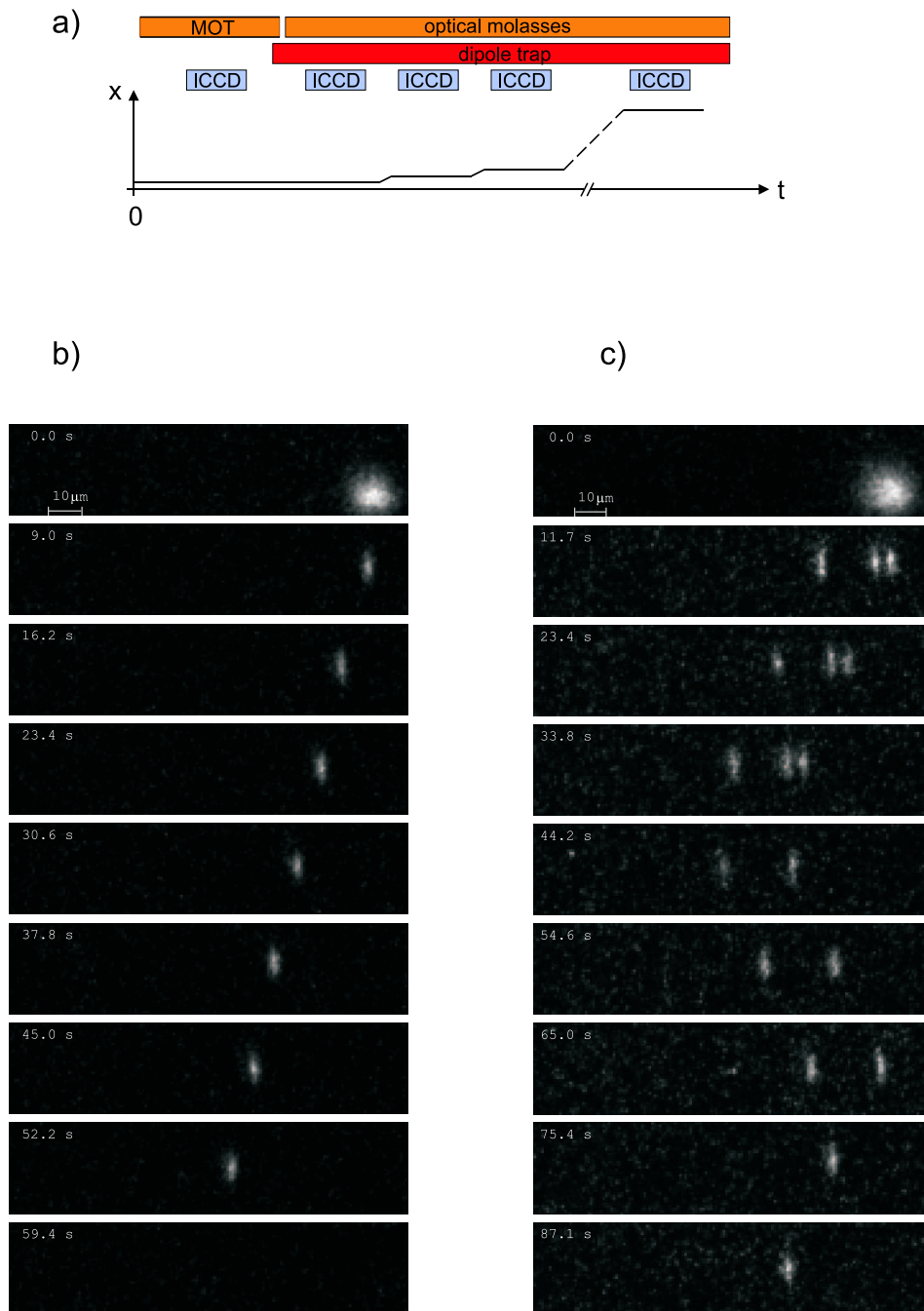


Figure 1.14: Continued imaging of the transport of single atoms. (a) Experimental sequence. Between successive images (exposure time: 1 s) the atoms are transported over a distance of $2 \mu\text{m}$. (b) Screenshots of the transport of a single atom, where only every fourth image is shown. (c) Synchronous transport of a string of three atoms. The direction of motion is changed twice. Here, every eighth image of the full movie presented in Reference [25] is shown. The exposure time per image was reduced to 0.5 s.

cannot follow the motion of the travelling standing wave any more. The finite bandwidth of the AOMs and a further heating effect due to abrupt changes of the acceleration limit the experimentally observed maximum acceleration to 10^5 m/s² [23, 48]. With these parameters, the transport of an atom over 1 mm only takes 200 μ s.

1.4.2 Imaging the controlled motion of a single atom

Combining our technique of imaging single atoms in the dipole trap with the optical conveyor belt we continuously image the transport of a single neutral atom [25]. An image sequence is recorded according to the scheme in Figure 1.14 (a). We first check the presence of one single atom in the MOT and take an image with an exposure time of 1 s. After transfer into the dipole trap we switch on the optical molasses and acquire the second image, again with an exposure time of 1 s. We then transport the atom over the distance of 2 μ m within 2 ms and take the next picture. This sequence of transport and imaging is repeated and yields a series of pictures of the same atom. The resulting “movie” (see Figure 1.14 (b)) shows the transport of the atom over a distance of 60 μ m within one minute and ends with the loss of the atom. The long lifetime of the atom in the trap demonstrates that the continuous molasses cooling effectively counteracts the heating mechanism due to AOM-phase noise.

We employed this technique to precisely calibrate the magnification of our imaging system. By comparing the positions of a single atom image on the ICCD chip before and after transport of the atom over the distance of 60 μ m, we determine the magnification to be 14.0 ± 0.1 .

A second movie shows the transport of a string of three trapped atoms, see Figure 1.14 (c). Here, we initiated the reversal of the transport direction by manually changing the sign of the relative detuning between the dipole trap laser beams. The average time before an atom is lost is of the order of 30 s which corresponds to the measured lifetime limited by background gas collisions [41, 63]. Both movies can be viewed online in Reference [25].

1.5 State preparation and detection

For quantum information processing (QIP) with atomic particles, long living internal atomic states serve as qubit states in which the quantum information is encoded. Therefore, efficient preparation and detection of these states are basic requirements for any QIP schemes.

The hyperfine ground states of cesium atoms are suitable candidates for qubit states. In order to tune the resonance frequency of the qubit transition via a magnetic field we choose the outermost Zeeman levels as qubit states (see Figure 1.15) which are denoted in the following as $|0\rangle = |F = 4, m_F = -4\rangle$ and $|1\rangle = |F = 3, m_F = -3\rangle$. The quantization axis is oriented along the dipole trap.

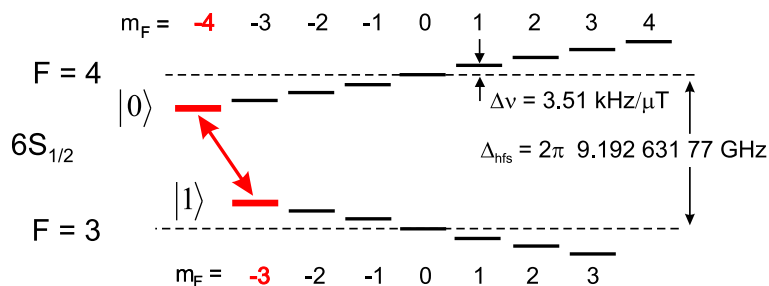


Figure 1.15: Zeeman splitting of the cesium ground state. By optically pumping the atom to the stretched Zeeman level $|F = 4, m_F = -4\rangle$, we can perform all coherent operations on the effective two-level system denoted by $|0\rangle$ and $|1\rangle$.

1.5.1 State preparation by optical pumping

Optical pumping laser

In all following experiments we initialize the trapped atoms in state $|0\rangle$ prior to any further manipulation of the internal states. For this purpose we optically pump the atoms into state $|0\rangle$ using a σ^- – polarized laser beam superposed with the dipole trap in x direction, see Figure 1.16. The optical pumping laser is resonant with the $|F = 4\rangle \leftrightarrow |F' = 4\rangle$ transition so that the final state $|F = 4, m_F = -4\rangle$ is a dark state. This ensures that not more photons are scattered during the optical pumping cycles than necessary to initialize the atom in $|0\rangle$.

The purity of the circular polarization of the optical pumping laser is the most critical parameter to maximize the population of the final state. Since the laser is coupled into the dipole trap axis by transmission through the last 45° mirror of the dipole trap laser, its polarization is polluted. We therefore precompensate its polarization before transmission through the mirror using a combination of a high-quality polarizer, a half- and a quarter-wave plate, such that its polarization right before entering the vacuum cell is circular to better than 10^{-4} .

The power ($P = 100$ nW) and pulse duration ($t = 1$ ms) of the optical pumping laser (spotsize $w_0 = 100$ μm) are optimized experimentally such that the atoms are not heated significantly during the pumping process. For this purpose we identify the threshold values when atoms get heated out of the trap and reduce the pulse duration to a tenth of its threshold value.

To avoid setting up an additional diode laser for optical pumping, we split off a part of the MOT cooling laser before its frequency is shifted near resonant to the $F = 4 \leftrightarrow F' = 5$ transition, see Section 1.1.2. Since it is stabilized to the $F = 4 \leftrightarrow F' = 3 - F' = 5$ – crossover resonance of the cesium spectroscopy, it is only 25 MHz blue detuned with respect to $F = 4 \leftrightarrow F' = 4$. Moreover, this detuning is partly compensated by the light shift of the D2 transition of the trapped atom.

Repumping laser

The MOT repumping laser, which is shined in along the dipole trap axis, is also used as a repumping beam during the optical pumping. It ensures that the atom is transferred back to the optical pumping cycle if it has decayed to the $F = 3$ ground state. It is typically operated at a power of $2.3 \mu\text{W}$. To ensure it is switched off not before the optical pumping laser has been switched off, we leave it on for another millisecond since the shutter closing time is of the same timescale.

Guiding field

We compensate the earth magnetic field and other DC-magnetic fields in the trapping region by minimizing the width of a Zeeman spectrum [64]. In addition, we apply a magnetic guiding field of $|\mathbf{B}_0| = 4 \text{ G}$ along the quantization axis (x) to counteract depolarization of the optically pumped atom due to remaining uncompensated DC components and AC fluctuations of magnetic fields. The guiding field shifts the $|0\rangle \leftrightarrow |1\rangle$ transition by $\delta_0/2\pi = (3g_3 - 4g_4)\mu_B/h \cdot |\mathbf{B}_0| = -9.8 \text{ MHz}$ with respect to the hyperfine transition frequency Δ_{hfs} , where μ_B denotes the Bohr-magneton, and $g_4 = -g_3 = 1/4$ the Landé factors. For this purpose we run a current of 10 A through the offset coil pair along the x direction, see Figure 1.3. To ensure that the noise and long-term drifts of the transition frequency remain smaller than 1 kHz, we use a low-noise current supply (Toellner TOE8851) with a current noise and stability of $< 10^{-4}$.

Note that we perform all experiments of internal state manipulation in a dipole trap with a depth lowered to $110 \mu\text{K}$. Such a shallow trap is required for efficient state-selective detection, see below. Furthermore, we have observed that changing the trap depth mixes the population of the Zeeman sublevels due to Raman transitions between degenerate Zeeman and vibrational levels $|m_F, n\rangle$ and $|m_F \pm 1, n \mp 1\rangle$ induced by the dipole trap laser [48]. To avoid this effect we must reduce the trap depth before optically pumping the atoms.

We can measure the quality of the achieved atomic polarization by performing spectroscopy on the $|0\rangle \leftrightarrow |1\rangle$ transition, see Sections 1.6.3 and 1.7, and find that the optical pumping efficiency is better than 99 %.

1.5.2 Single atom state-selective detection

After any experiment involving manipulation of the internal atomic states, we measure the final state of the atoms. To discriminate the atomic states, we apply a so-called “push-out” laser resonant with the $F = 4 \leftrightarrow F' = 5$ transition which removes all atoms in $F = 4$ from the trap while leaving those in $F = 3$ untouched. The laser is shined in along the z axis with a saturation parameter of $s_0 = I/I_0 = 3$, see Figure 1.16. Its radiation pressure force overcomes the radial dipole force and pushes atoms in $F = 4$ out of the trap within less than half a radial oscillation period ($\approx 350 \mu\text{s}$). Additionally, we decrease the trapping forces to facilitate the push-out process by lowering the dipole trap depth to $110 \mu\text{K}$.

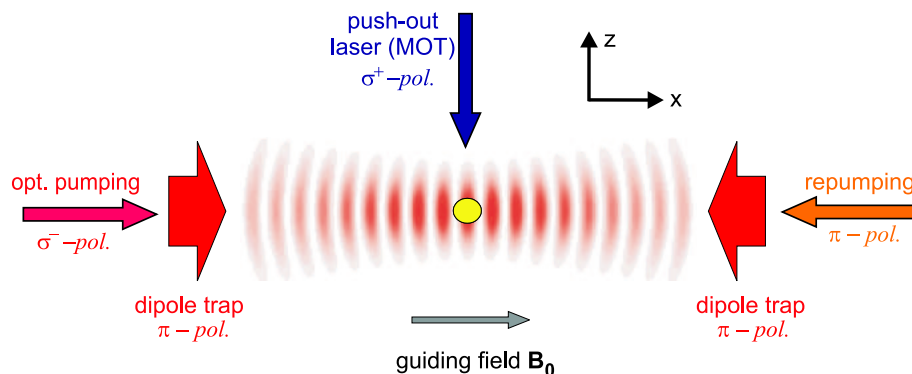


Figure 1.16: Geometry of laser beams for state preparation and detection. Optical pumping and repumping beams are aligned along the dipole trap axis. The applied guiding field inhibits depolarization of the atom. Note that the guiding field is rotated to the z axis before the state-selective push-out laser is applied.

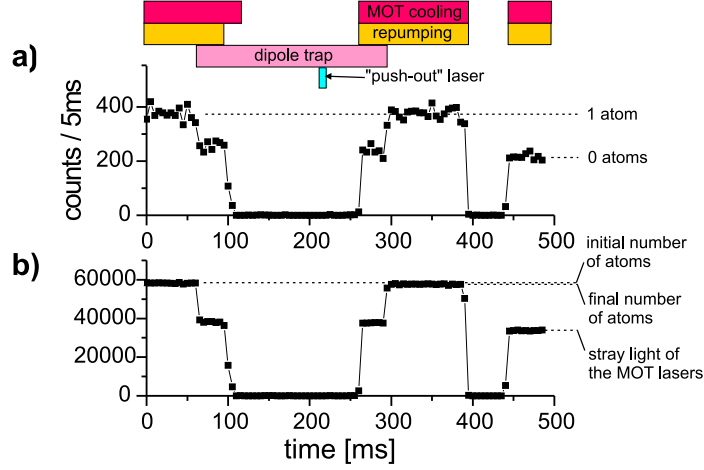
To ensure efficient discrimination between the two ground state levels, we choose the laser to be σ^+ polarized so that the atoms are optically pumped to the $|F = 4, m_F = 4\rangle \leftrightarrow |F' = 5, m_{F'} = 5\rangle$ transition from where they cannot spontaneously decay to $F = 3$. For this purpose, we rotate the quantization axis from x to z orientation by simultaneously switching off the guiding field \mathbf{B}_0 and applying a guiding field of 1.5 G along the z axis within 10 ms.

While in previous experiments we have used a separate push-out laser [48], we now, for simplicity, use the MOT cooling laser beam along the z axis. It is tuned to resonance and switched on for 500 μs using the AOM, see Section 1.1.2. At the same time, shutters block the retro-reflected beam and the other two MOT beams.

To test the efficiency of our state-selective detection scheme, we trap a single atom in the MOT, see Figure 1.17 I (a). During transfer of the atom into the dipole trap, we switch off the MOT repumping laser before the cooling laser so that the atom is optically pumped to state $F = 3$. After application of the push-out laser, the atom is transferred back into the MOT, where the fluorescence signal reveals its presence. In order to prepare the atom in $F = 4$ during transfer into the dipole trap we shine in the repumping laser longer than the cooling laser, see Figure 1.17 II (a). The atom is then removed from the trap by the application of the push-out laser.

If we add the signals of individual repetitions, we can infer the average state population by comparing the fluorescence levels in the MOT before and after the push-out process, see the parts (b) of Figure 1.17. We have optimized the power and pulse duration ($P = 30 \mu\text{W}$, $t = 500 \mu\text{s}$) of the push-out laser such that the survival probability of atoms prepared in $F = 4$ is smaller than 0.5 % whereas it is larger than 99 % for atoms prepared in $F = 3$.

I) Preparation in $F=3$



II) Preparation in $F=4$

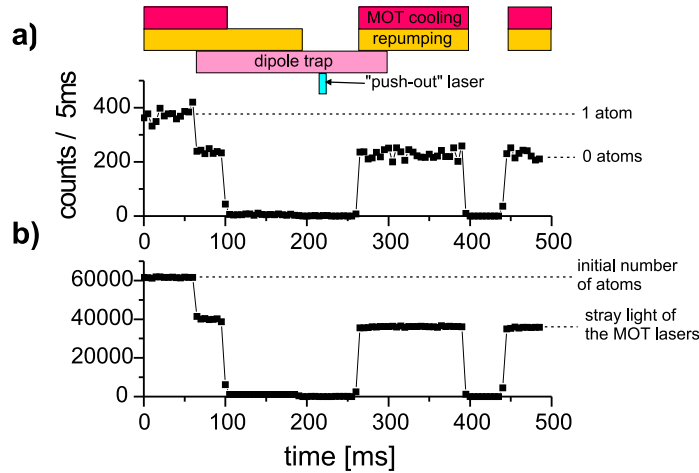


Figure 1.17: State-selective detection. While an atom prepared in state $F = 3$ survives the application of the push-out laser (I (a)), it is removed from the trap if it has been prepared in $F = 4$ (II (a)). I and II (b) show the sum of the signals of 157 and 167 repetitions with a single atom each.

1.6 Quantum state preparation using microwave radiation

In addition to the preparation of the energy eigenstates $|0\rangle$ and $|1\rangle$, quantum information processing (QIP) requires to accurately prepare desired quantum states $\alpha|0\rangle + \beta|1\rangle$, with $(\alpha, \beta) \in \mathbb{C}$, in order to use our single atoms as qubits. We demonstrate one-qubit rotations some of which are also referred to as Hadamard gate in the language of quantum information processing.

There are several possible techniques to perform coherent manipulation of the two hyperfine ground states. One option is the use of an optical two-photon Raman process

to resonantly couple the two ground states via a virtual excited level [64, 65]. An experimentally simpler solution, however, is the application of microwaves at the resonance frequency of the hyperfine transition to drive magnetic dipole transitions between the two states.

1.6.1 Bloch vector model

The interaction between the oscillating magnetic field component of the microwave radiation, $B_{\text{MW}} \cos \omega t$, and the magnetic dipole moment μ of the atom is well described by the Bloch vector model. The Bloch vector model is very convenient in the sense that the interaction dynamics between atom and field can easily be visualized on the Bloch sphere. Here, the position of the Bloch vector $\mathbf{u} \equiv (u, v, w)$ on a unit sphere characterizes the properties of the atomic dipole moment. The u and v components describe its coherent in-phase and in-quadrature components with respect to the driving field. w quantifies the population difference of the two atomic levels, with $w = -1$ ($w = +1$) corresponding to $|0\rangle$ ($|1\rangle$). In the reference frame rotating at the microwave frequency ω , the evolution of the Bloch vector is well approximated by the optical Bloch equations [51]:

$$\dot{\mathbf{u}} = -\boldsymbol{\Omega} \times \mathbf{u} \quad (1.18)$$

The torque vector $\boldsymbol{\Omega} \equiv (\Omega_{\text{R}}, 0, \delta)$ determines the dynamic properties of the system, where $\Omega_{\text{R}} = \mu B_{\text{MW}} / \hbar$ is the Rabi frequency and $\delta = \omega - \omega_0$ the detuning between the microwave frequency and the resonance frequency of the atomic hyperfine transition ω_0 .

In the case of monochromatic radiation with constant amplitude, the Bloch vector performs Rabi oscillations. After initialization in the state $\mathbf{u}_0 = (0, 0, -1)$, Equation (1.18) yields the time evolution of the population:

$$w(t, \delta) = -1 + \frac{2\Omega_{\text{R}}^2}{\Omega^2} \sin^2 \left(\frac{\Omega t}{2} \right), \quad (1.19)$$

where I have introduced the generalized Rabi frequency $\Omega = \sqrt{\Omega_{\text{R}}^2 + \delta^2}$.

A resonant microwave pulse ($\delta = 0$) rotates the Bloch vector around the u axis, see Figure 1.18 (a). In this case, Equation (1.19) simplifies to $w(t, 0) = -\cos \Omega_{\text{R}} t$ so that the rotation angle corresponds to the integral of the Rabi frequency over the pulse time t :

$$\theta(t) = \int_0^t \Omega_{\text{R}}(t') dt'. \quad (1.20)$$

Two special cases are worth mentioning, $\theta(t) = \pi/2$ and $\theta(t) = \pi$. A $\pi/2$ pulse rotates the initialized Bloch vector into the uv plane, see Figure 1.18 (b), and creates a symmetric superposition state. A π pulse induces a spin flip and is also used as a rephasing pulse in spin echo spectroscopy, see Section 2.4.4.

Finally, Figure 1.18 (c) shows a non-driven Bloch vector which freely precesses around the w axis.

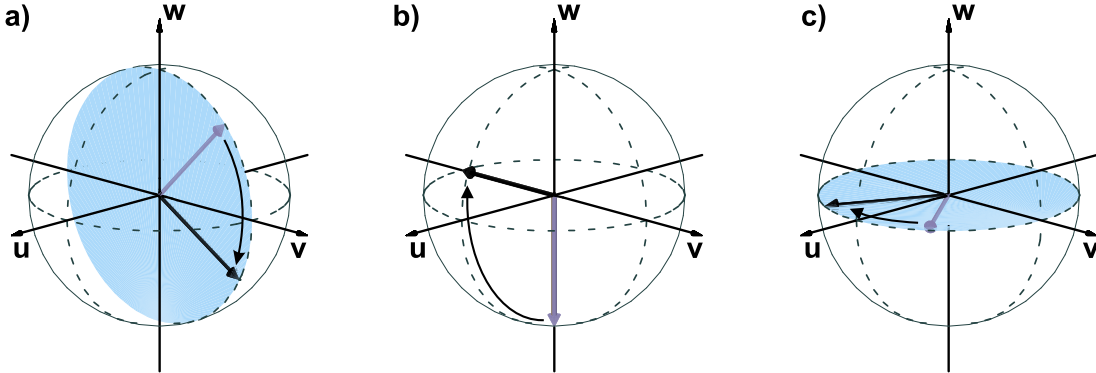


Figure 1.18: Bloch vector dynamics on the Bloch sphere. (a) Resonant driving corresponds to a rotation around the u axis. (b) A $\pi/2$ pulse rotates the Bloch vector from a perfectly polarized state into the uv plane corresponding to a superposition of states. (c) If the Bloch vector is not driven by the external field, it precesses freely around the w axis.

1.6.2 Experimental microwave setup

An overview of the experimental microwave setup is given in Figure 1.19.

Microwave source

Our synthesizer (Agilent 83751A, 0.01 - 20 GHz) has a specified accuracy of 10^{-11} and is locked to an external 10 MHz rubidium frequency standard (Stanford Research Systems, PRS10). It is remote controlled by a computer and has numerous features for its convenient use in spectroscopy applications. It can be operated in a stepped sweep mode such that the user can determine start and stop frequency and the number of steps. Whenever it receives a trigger pulse, the synthesizer increases the output frequency by a specific amount with a settling time of 10 ms. A pulse mode permits the generation of short square pulses (duration $> 2 \mu\text{s}$, rise/fall time $< 100 \text{ ns}$) with a duration determined by an external trigger pulse. Simultaneously, the synthesizer permits amplitude (AM) and frequency modulation (FM) using two analog input channels.

The output of the synthesizer (max. +15 dBm) is sent to a power amplifier (MA-Ltd., AM53-9-9.4-33-35), which amplifies the microwave signal by 36 dB up to a maximum output power of +38 dBm. An RF cable (loss -2 dB) guides the signal to the microwave antenna.

Microwave antenna

An optimal antenna is the most crucial aspect in order to maximize the microwave intensity I_{MW} at the position of the trapped atoms. In previous experiments [48] we used a bare SMA - X-band connector near the vacuum chamber and obtained a Rabi frequency of $\Omega_{\text{R}} = 2\pi \cdot 13.5 \text{ kHz}$. However, its size did not permit to place it between the MOT coils close to the glass cell. In order to increase the microwave intensity, we tested various

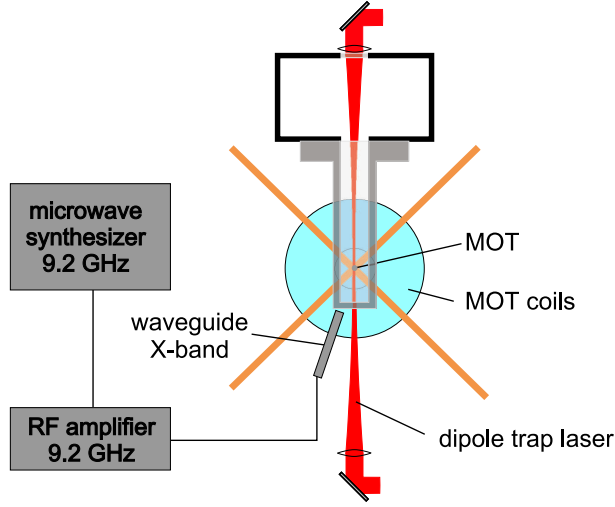


Figure 1.19: Setup for microwave spectroscopy. The microwave signal at 9.2 GHz is created by a synthesizer and amplified. An open X-band waveguide pointed towards the MOT is the most efficient antenna to maximize the microwave intensity at the position of the trapped atoms.

home-built antennas and measured the Rabi frequency $\Omega_R \propto \sqrt{I_{MW}}$. Placing the bare end of an RF cable close to the vacuum glass cell slightly increased I_{MW} by 20 %. A more significant improvement was the use of a truncated X-band waveguide flanged to an SMA – X-band connector. The diameter of the waveguide is small enough to fit between the MOT coils so that its end is placed only 1 mm away from the glass cell and is directed straight towards the MOT position, see Figure 1.19. Furthermore, its walls are sharpened at the end to reduce reflections [66]. Using this antenna increased I_{MW} by more than a factor of 4 and resulted in a Rabi frequency of up to $\Omega_R = 2\pi \cdot 32$ kHz.

In the experiments described below we use the following configuration: Synthesizer (+5 dBm) → short cable (−1 dB) → amplifier (+38 dBm output power) → short cable (−2 dB) → microwave antenna (+36 dBm, = 4.0 W).

1.6.3 Frequency calibration

Resonant driving of the states $|0\rangle$ and $|1\rangle$ requires a precise calibration of the atomic resonance frequency which is Zeeman shifted in the applied magnetic guiding field \mathbf{B}_0 . We therefore record a microwave spectrum around the estimated resonance frequency $\Delta_{\text{hfs}} + \delta_0$ using the experimental sequence depicted in Figure 1.20.

Experimental sequence

We operate the microwave synthesizer in stepped sweep mode where the start and stop frequency define the frequency interval to be scanned which we typically choose to be 400 kHz. The MOT loading time t_{low} at low B-field gradient, see Section 1.1, is set such that we load on average 5 atoms into the MOT. In addition, we optimize the parameters

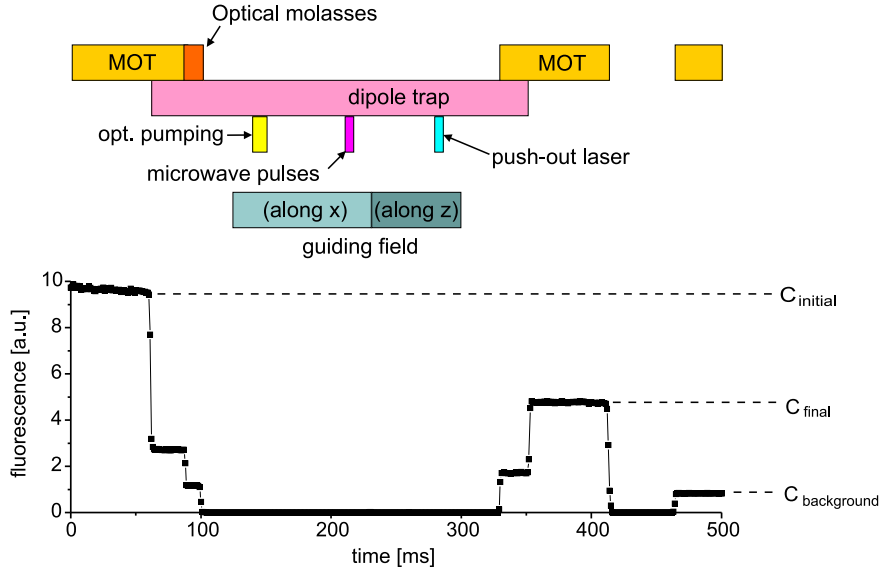


Figure 1.20: Experimental sequence used for microwave spectroscopy. A number of atoms is loaded and cooled in the dipole trap. After initialization by optical pumping they are exposed to one or several microwave pulses. The population transfer efficiency is measured by comparing the fluorescence level after state-selective detection C_{final} with the initial fluorescence C_{initial} . The fluorescence signal shows an average of 5 individual signals with a mean atom number of 5 per shot.

of the cooling laser for effective molasses cooling in the dipole trap, see Section 1.3.3.

After these preparatory steps we run the computer-controlled experimental sequence (Figure 1.20). It starts by loading of atoms into the MOT which are then transferred into the dipole trap. During transfer, the cooling laser power and detuning are switched to the molasses cooling regime. Before the atoms are optically pumped into $|0\rangle$, we lower the trap depth to $100 \mu\text{K}$ and switch on the guiding field B_0 along the x axis, see Section 1.5.1. We then apply a rectangular microwave pulse with a duration of $16 \mu\text{s}$ which corresponds to a π pulse for resonant driving. This time is found by iterative recording of spectra and Rabi oscillations, see below. For state-selective detection we rotate the quantization axis, apply the push-out laser, see Section 1.5.2, and transfer the remaining atoms back into the MOT. After recording the MOT fluorescence, we switch off the lasers and the magnetic field of the MOT for 50 ms to release all trapped atoms. Switching the MOT lasers back on allows us to measure their background stray light. This entire sequence is repeated 5 times before the microwave frequency is increased by 10 kHz.

For data analysis, the recorded fluorescence traces from the APD are added up in groups of 5, corresponding to the same microwave frequency. The resulting signal for one exemplary group is shown in Figure 1.20. The measured photon count rates C_{initial} , C_{final} , and C_{backgr} are used to infer the number of atoms before and after the experimental procedure, N_{initial}

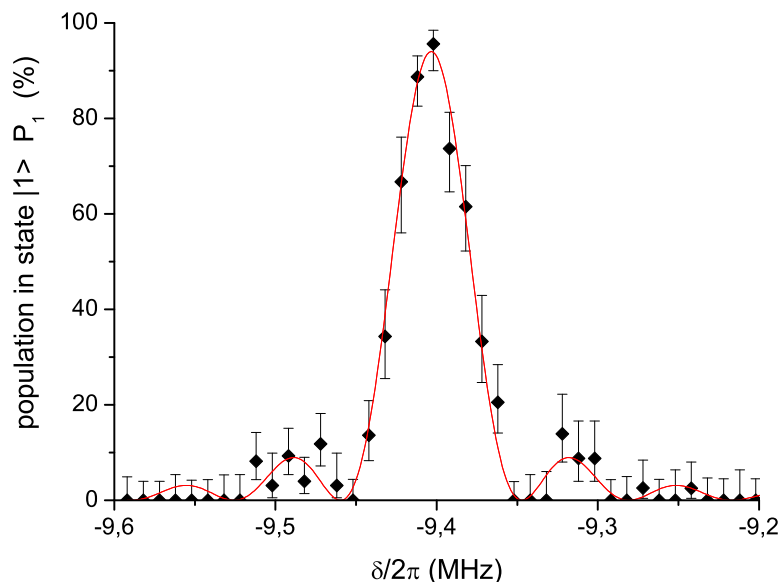


Figure 1.21: Fourier limited spectrum of a rectangular π pulse of $16 \mu\text{s}$ duration. Every data point shows the average population in state $|1\rangle$ of 5 shots with 5 atoms each. The solid line is a fit corresponding to Equation (1.23), with the fit parameters summarized in Table 1.1.

and N_{final} :

$$N_{\text{initial}} = \frac{C_{\text{initial}} - C_{\text{backgr}}}{C_{\text{1atom}}} \quad \text{and} \quad N_{\text{final}} = \frac{C_{\text{final}} - C_{\text{backgr}}}{C_{\text{1atom}}}, \quad (1.21)$$

where the fluorescence rate of a single atom, C_{1atom} , is measured independently. From the atom numbers we obtain the fraction of atoms transferred to state $|1\rangle$,

$$P_1 = \frac{N_{\text{final}}}{N_{\text{initial}}}. \quad (1.22)$$

The error of P_1 is calculated using 1σ -confidence limits [48, 67].

Figure 1.21 shows the Fourier-limited spectrum in a frequency interval of 400 kHz and with a step size of 10 kHz. The recording time is about 5 min. I have plotted the measured population transfer P_1 as a function of microwave detuning δ from the unshifted resonance Δ_{hfs} . The fit function is derived from Equation 1.19:

$$P_3(\delta) = P_{\text{max}} \cdot \frac{\Omega_{\text{R}}^2}{\Omega^2} \sin^2\left(\frac{\Omega t_{\text{pulse}}}{2}\right), \quad \text{with} \quad \Omega^2 = (\delta - \delta_0)^2 + \Omega_{\text{R}}^2. \quad (1.23)$$

As a fit result, we obtain the values summarized in Table 1.1. The shift of the peak position is determined to a precision of 10^{-4} and effectively measures the magnitude of the magnetic guiding field to be $|\mathbf{B}_0| = 3.84 \pm 0.04$ G using the trapped atoms as a

pulse duration	t_{pulse}	$15.9 \pm 0.4 \mu\text{s}$
Rabi frequency	$\Omega_{\text{R}}/2\pi$	$28 \pm 3 \text{ kHz}$
shift of peak position	$\delta_0/2\pi$	$-9.403 \pm 0.001 \text{ MHz}$
maximum population transfer	P_{max}	$97 \pm 5 \%$

Table 1.1: Fit parameters for the spectrum of Figure 1.21.

probe. Further effects contributing to a frequency shift such as differential light shifts, quadratic Zeeman shifts, and collisional shifts are two orders of magnitude smaller than the contribution of the linear Zeeman shift measured here. These effects were studied on the magnetically insensitive clock transition $|F = 4, m_F = 0\rangle \leftrightarrow |F = 3, m_F = 0\rangle$ in previous work [48].

We were able to significantly increase the resonant population transfer as compared to previous experiments. The two key improvements lie in the high optical pumping efficiency and the reduction of atom numbers to only ≈ 5 per shot. Previously, atom numbers up to 50 had caused atom losses by cold collisions [48].

The pulse duration inferred from the spectrum agrees well with the actually applied pulse duration of $t_{\text{pulse}} = 16 \mu\text{s}$. The fitted Rabi frequency is confirmed by recording Rabi oscillations.

1.6.4 Rabi rotations

The demonstration of Rabi rotations is the most perspicuous way of showing the preparation of quantum states. The experimental procedure is similar to the one used for recording a spectrum. The microwave frequency is fixed to the atomic resonance calibrated above, and we measure the population transfer as a function of the microwave pulse duration t_{pulse} . For the Rabi rotations shown in Figure 1.22, the sequence was repeated 5 times with 11 atoms on average per run before we increased the pulse duration by steps of $4 \mu\text{s}$. The fit function derived from 1.19 reads:

$$P_1(t_{\text{pulse}}) = P_{\text{min}} + \frac{P_{\text{max}} - P_{\text{min}}}{2} (1 - \cos(\Omega_{\text{R}} t_{\text{pulse}})) . \quad (1.24)$$

As above, $P_{\text{max}} = 89 \pm 1 \%$ measures the maximum population transfer achieved. It is slightly smaller than for the spectrum shown in Figure 1.21, which is probably due to the fact that we used more atoms per shot in this measurement than for recording the spectrum. With $P_{\text{min}} = 0.0_{-0.0}^{+1.8} \%$, however, the fringe contrast C is excellent:

$$C = \frac{P_{\text{max}} - P_{\text{min}}}{P_{\text{max}} + P_{\text{min}}} = 100.0_{-1.8}^{+0.0} \% . \quad (1.25)$$

From the fit we obtain a Rabi frequency of $\Omega_{\text{R}} = 2\pi \cdot (28.48 \pm 0.03) \text{ kHz}$ which agrees well with the Rabi frequency inferred from the spectrum of Figure 1.21. In the state vector representation of the two-level atom, the evolution of the wavefunction reads

$$|\psi(t_{\text{pulse}})\rangle = \cos(\Omega_{\text{R}} t_{\text{pulse}}/2)|0\rangle - i \sin(\Omega_{\text{R}} t_{\text{pulse}}/2)|1\rangle . \quad (1.26)$$

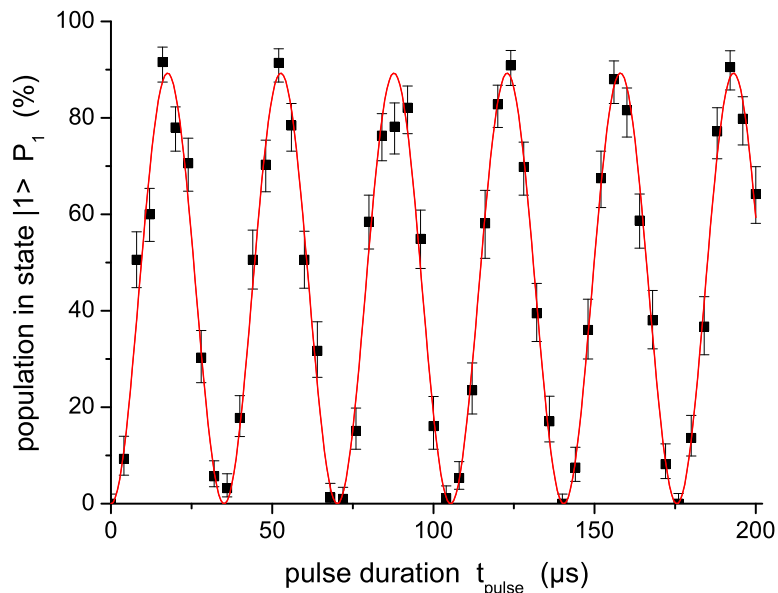


Figure 1.22: Rabi rotations between states $|0\rangle$ and $|1\rangle$ in a homogeneous magnetic offset field. Every data point shows the average population in state $|1\rangle$ of 5 shots with 11 atoms each. While the maximum detected population in $|1\rangle$, P_{\max} , is limited by atom losses due to cold collisions, the fringe contrast $C = 100^{+0.0}_{-1.8}$ % is excellent. The solid line is a fit according to Equation (1.24).

A $\pi/2$ pulse therefore transforms atoms which are initialized in state $|0\rangle$, into the symmetric superposition state $(|0\rangle - i|1\rangle)/\sqrt{2}$. This operation corresponds to a Hadamard gate in quantum information processing.

1.7 Robust spin flips by adiabatic population transfer

The coherent manipulation of the atomic hyperfine states by resonant microwave pulses (see Section 1.6) is straightforward and has successfully been implemented in our experimental system. However, if the experiment merely requires spin flips, adiabatic population transfer is more suitable. It is much more robust with respect to fluctuations of the atomic resonance frequency by, e. g., beam pointing instabilities, fluctuations of the intensity or the polarization of the trapping lasers, or perturbations by static and dynamic magnetic or electric fields. This insensitivity of adiabatic population transfer against the experimental conditions has been used and investigated in neutron beam experiments [68, 69]. We have studied this technique as an alternative to resonant coherent internal state manipulation of our trapped atoms [70].

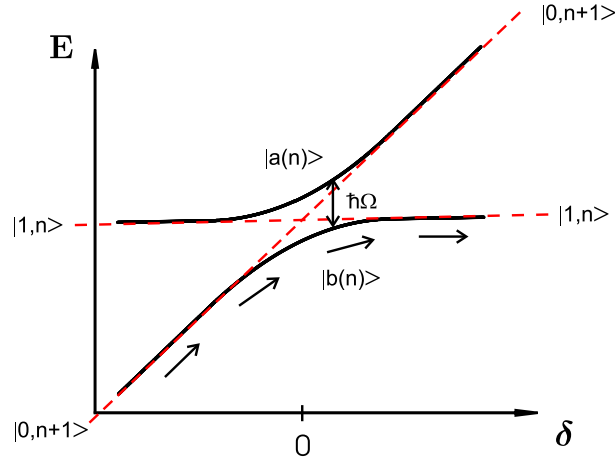


Figure 1.23: Adiabatic population transfer in the dressed state picture. The eigenstates $|a(n)\rangle$ and $|b(n)\rangle$ of the coupled atom – photon system do not intersect at the atomic resonance $\delta = 0$. By sweeping the microwave frequency from large negative to large positive detuning, a spin flip occurs because the wavefunction adiabatically follows the eigenstate $|a(n)\rangle$ or $|b(n)\rangle$.

1.7.1 Dressed state picture

The robustness of an adiabatic passage with respect to frequency fluctuations is achieved by sweeping the microwave frequency over a large interval across the atomic resonance. As long as the atomic resonance frequency lies within the sweep interval, the population transfer is successful. This scheme is visualized in Figure 1.23 using dressed states. Here, the two relevant atomic states $|0\rangle$ and $|1\rangle$ are “dressed” with the photon number states of the microwave field $|n\rangle$. The corresponding Schrödinger equation reads [52]:

$$i\hbar \frac{d}{dt} \Psi(t) = i\hbar \frac{d}{dt} \begin{pmatrix} c_a(t) |a(n)\rangle \\ c_b(t) |b(n)\rangle \end{pmatrix} = \frac{\hbar}{2} \begin{pmatrix} \Omega & 2i\dot{\theta} \\ -2i\dot{\theta} & -\Omega \end{pmatrix} \begin{pmatrix} c_a(t) |a(n)\rangle \\ c_b(t) |b(n)\rangle \end{pmatrix}, \quad (1.27)$$

with the eigenstates

$$\begin{pmatrix} |a(n)\rangle \\ |b(n)\rangle \end{pmatrix} = \begin{pmatrix} \sin \theta & \cos \theta \\ \cos \theta & -\sin \theta \end{pmatrix} \begin{pmatrix} |0, n+1\rangle \\ |1, n\rangle \end{pmatrix} \quad (1.28)$$

and the mixing angle $\theta(t) = \arctan(-\Omega_R(t)/\delta(t))/2$. The fact that the energies of these eigenstates are split by $\hbar\Omega$ so that the levels do not cross for $\delta = 0$, is also referred to as “anti-crossing”. Slow rotation of the mixing angle by sweeping the detuning from $\delta \ll 0$ to $\delta \gg 0$ causes the wavefunction to adiabatically follow the eigenstate. If the system is initially in state $|0, n+1\rangle$ it evolves to state $|1, n\rangle$ along $|b(n)\rangle$, see Figure 1.23. Vice versa, state $|1, n\rangle$ will evolve to state $|0, n+1\rangle$ along $|a(n)\rangle$. Thus, regardless of the initial state, a spin flip always occurs.

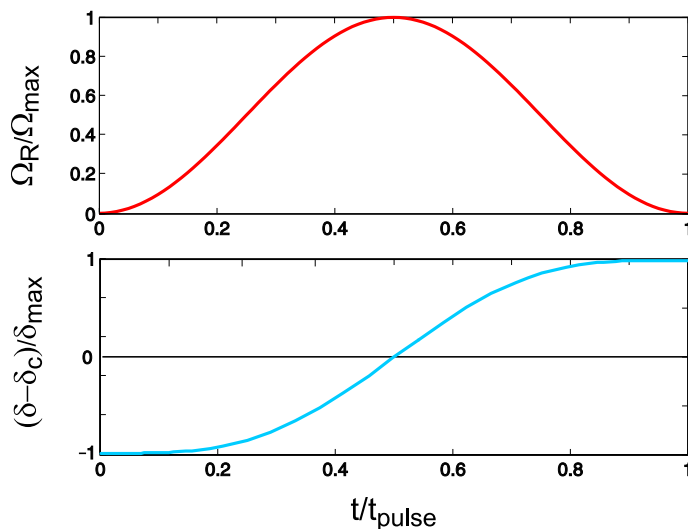


Figure 1.24: Microwave pulse shape for adiabatic population transfer. While the frequency detuning is symmetrically swept around a central detuning δ_c , the microwave intensity is increased and decreased.

Adiabaticity condition

The spin flip efficiency crucially depends on the adiabaticity of the frequency sweep. The interaction is adiabatic as long as the off-diagonal coupling term of the Hamiltonian in Equation (1.27) remains small compared to the level splitting between $|a(n)\rangle$ and $|b(n)\rangle$. Effectively, the change of the mixing angle must remain significantly smaller than the generalized Rabi frequency $\Omega(t) = \sqrt{\Omega_R^2(t) + \delta^2(t)}$ [71]:

$$f(t) = \frac{\dot{\theta}(t)}{\Omega(t)} = \frac{|\dot{\delta}(t)\Omega_R(t) - \delta(t)\dot{\Omega}_R(t)|}{2\Omega(t)^3} \ll 1, \quad (1.29)$$

where $f(t)$ is called adiabaticity function.

Consequently, for efficient population transfer the shape of the microwave pulse has to be tailored to fulfil the adiabaticity condition (1.29). For our experiment, we choose the pulse shape according to Reference [52]:

$$\Omega_R(t) = \Omega_{\max} \sin^2\left(\frac{\pi}{t_{\text{pulse}}} t\right) \quad (1.30)$$

$$\delta(t) = \delta_c + \text{sign}\left(t - \frac{t_{\text{pulse}}}{2}\right) \cdot \delta_{\max} \sqrt{1 - \sin^4\left(\frac{\pi}{t_{\text{pulse}}} t\right)} \quad (1.31)$$

The frequency sweep is symmetric with respect to the central detuning δ_c , which specifies the average frequency offset to the atomic resonance frequency. Simultaneously, we slowly increase and decrease the microwave intensity $I_{\text{MW}} \propto \Omega_R^2$, see Figure 1.24. The respective

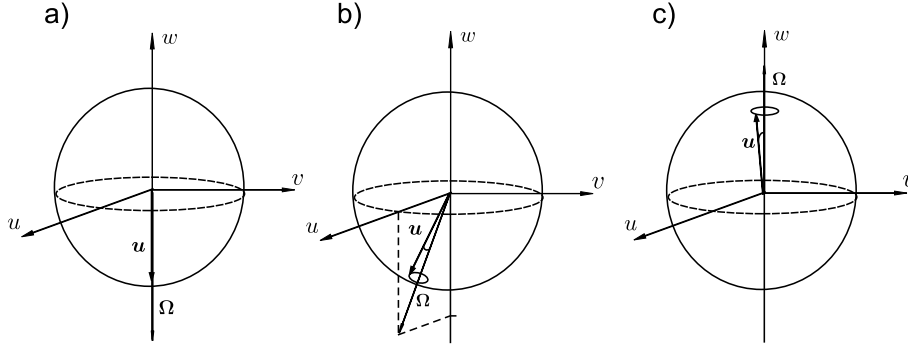


Figure 1.25: Adiabatic population transfer in the Bloch vector model, before (a), during (b), and after (c) the frequency sweep across the atomic resonance.

amplitudes are denoted δ_{\max} and Ω_{\max} , t_{pulse} is the duration of the microwave pulse. As I show in Figure 1.27 (b), this pulse shape fulfils the adiabaticity condition (1.29) over a wide range of detunings δ_c .

Bloch vector model

To show the conceptual difference between a resonant and an adiabatic spin flip, I visualize the adiabatic population transfer in the Bloch vector model. Suppose an atom is initialized in state $|0\rangle$ corresponding to $\mathbf{u}(t=0) = (0, 0, -1)$, see Figure 1.25 (a). For large negative detuning, the torque vector $\mathbf{\Omega}(t=0)$ is parallel to the Bloch vector. As the frequency is swept slowly across the atomic resonance, see Figure 1.25 (b), the Bloch vector quickly precesses around the torque vector and follows its rotation around the v axis, according to Equation (1.18). After the frequency sweep, both $\mathbf{\Omega}(t=t_{\text{pulse}})$ and $\mathbf{u}(t=t_{\text{pulse}}) = (0, 0, 1)$ point upwards corresponding to state $|1\rangle$, see Figure 1.25 (c). The better the adiabaticity condition is fulfilled the smaller the remaining opening angle of the precession cone of the Bloch vector will be.

1.7.2 Experimental setup for adiabatic frequency sweeps

The experimental setup for performing adiabatic spin flips is similar to the one described in Section 1.6.2. The frequency sweep is performed by external frequency modulation of the microwave signal. For this purpose, our microwave synthesizer would need to be unlocked from the 10 MHz Rubidium clock. Since its frequency drifts by several tens of kHz when it is unlocked, we use a second synthesizer with better frequency stability and operate it at 1 GHz (Rhode & Schwarz SML02, 9kHz...2.2GHz). Its output signal is mixed with the RF signal of our microwave source operated at 10.2 GHz such that their difference frequency matches the atomic resonance frequency of 9.2 GHz. We modulate the frequency of the microwave pulse by external modulation of the 1 GHz synthesizer. The amplitude modulation of the microwave pulse is performed by a PIN-diode attenuator (miteq, MPHT 910930-60-10) with an insertion loss of 3.2 dB at 10.2 GHz and a maximum attenuation of 60 dB.

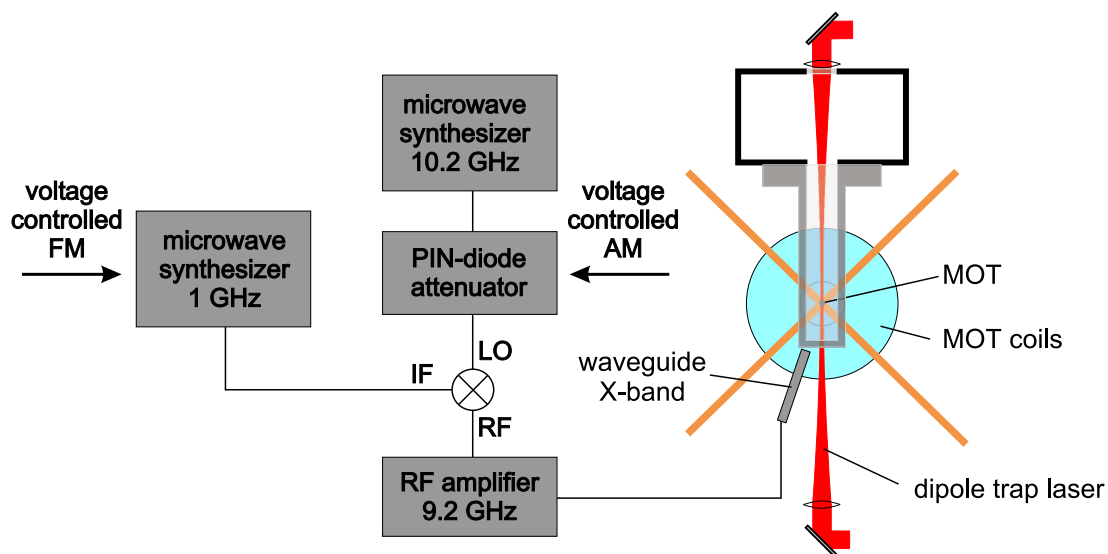


Figure 1.26: Setup for microwave spectroscopy using an adiabatic passage technique. The frequency modulation (FM) for the adiabatic frequency sweep is performed by an externally modulated synthesizer at 1 GHz whose signal is mixed with the microwave radiation at 10.2 GHz. The amplitude modulation (AM) is performed by a PIN-diode attenuator. Both FM- and AM-pulse shapes according to Equation (1.30) are controlled by the computer control.

As an RF mixer, we use a level-13 mixer (miteq M0812) in reverse mode, see Figure 1.26. Its low frequency IF output is used as an input for the 1 GHz signal (IF power = 8.4 dBm), the microwave signal at 10.2 GHz is fed into the LO port (LO power = 13.2 dBm), while the RF input serves as the high frequency output (RF power = 0.8 dBm) which is connected to the amplifier. The sum frequency at 11.2 GHz is not amplified due to the limited bandwidth of the amplifier. The difference frequency at 9.2 GHz is amplified to 37 dBm resulting in a microwave power of 35 dBm fed into the antenna. The remaining transmission of the carrier at 10.2 GHz has a power of -19 dBm (fed into the antenna) and is therefore negligible.

1.7.3 Spectrum of adiabatic population transfer

Experimental sequence

We record a spectrum to demonstrate adiabatic population transfer on our trapped cesium atoms. The experimental procedure is similar to the one for recording the Fourier-limited π -pulse spectrum shown in Section 1.6.3. A number of atoms is loaded into the dipole trap ($U_0 = 140 \mu\text{K}$), and initialized in $|0\rangle$. The shape of the applied microwave pulse corresponds to Equation (1.30), with the pulse parameters Ω_{\max} , δ_{\max} , and t_{pulse} given in Table 1.2.

Using our state-selective detection method, we now measure the population in state $|1\rangle$ as a function of the central detuning δ_c . For the spectrum shown in Figure 1.27 (a), $\delta_c/2\pi$

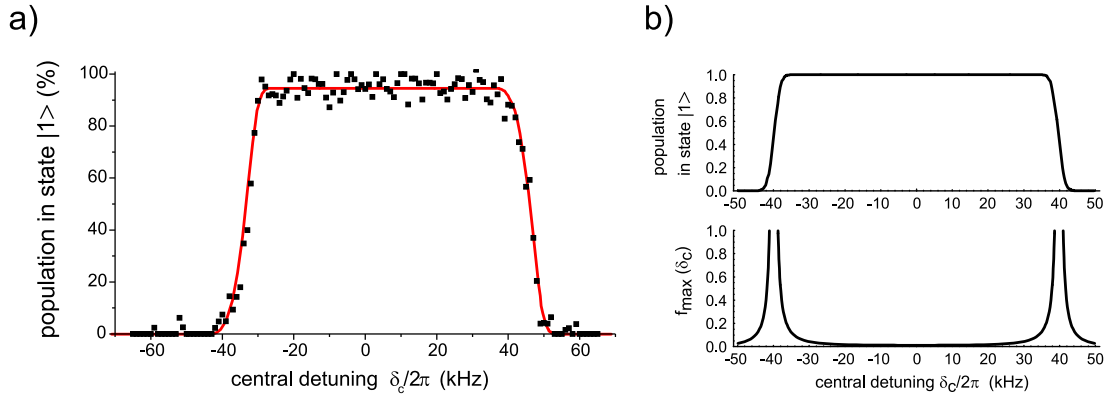


Figure 1.27: Adiabatic population transfer. a) Each data point shows the average population in state $|1\rangle$ of ten shots with five atoms each. The solid line shows the fit function according to Equation (1.35), derived from a numerical integration of the optical Bloch equations. The corresponding fit parameters are listed in Table 1.2. b) The top graph shows a numerically calculated spectrum for the parameters given in Table 1.2, but neglecting the energy distribution of the trapped atoms. Below, the corresponding adiabaticity function defined in Equation (1.32) is plotted for the same parameters. The two graphs illustrate that the adiabaticity condition is no longer fulfilled at the edges of the spectrum.

was stepped from -65 kHz to 65 kHz with a stepsize of 1 kHz and ten repetitions per step. We found that the phase noise of the microwave signal of the Agilent synthesizer is much larger in stepped sweep mode than it is in continuous wave mode. This property causes the slopes of the resulting spectrum to be less sharp. We therefore operate the synthesizer in continuous wave mode, in contrast to the experimental sequence presented in Section 1.6.3. In order to step the frequency, the synthesizer is reprogrammed by the computer control via GPIB for every step.

Results

The recorded spectrum is shown in Figure 1.27 (a). The wide plateau shows a population transfer efficiency $P_1 > 90\%$ for $-30\text{ kHz} < \delta_c/2\pi < 40\text{ kHz}$. It is constant for a large interval of the central detuning of the frequency sweep demonstrating robustness of the spin flip efficiency with respect to frequency drifts and fluctuations. This efficiency rapidly drops to 0 beyond this frequency interval. The asymmetry of the spectrum is due to an inhomogeneous broadening of the atomic resonance frequency, as discussed below.

At the edges of the spectrum the adiabaticity condition (1.29) is no longer fulfilled, as illustrated in Figure 1.27 (b). The upper part shows the expected population transfer from a numerical integration of the optical Bloch equations (1.18), with the pulse shape according to Equation (1.30) and the experimental parameters according to Table 1.2. Below, the maximum value of the corresponding adiabaticity function is plotted, defined

as:

$$f_{\max}(\delta_c) = \max_{t \in [0, t_{\text{pulse}}]} f(t, \delta_c). \quad (1.32)$$

While $f_{\max}(\delta_c)$ remains $\ll 1$ for a large frequency interval, it increases rapidly at the edges of the spectrum and demonstrates that the frequency sweep is no longer adiabatic as soon as $|\delta_c|$ approaches δ_{\max} . Quantitatively, the comparison of the two graphs in Figure 1.27 (b) shows that the population transfer efficiency drops below 90 % when $f_{\max}(\delta_c) > 0.5$ at $|\delta_c|/2\pi \geq 38$ kHz. When the central detuning δ_c becomes even larger than the amplitude δ_{\max} of the frequency sweep, the atomic resonance frequency is no longer crossed during the sweep so that no population transfer occurs.

As opposed to the ideal case of Figure 1.27 (b), the recorded spectrum of Figure 1.27 (a) has asymmetric edges. They arise from an inhomogeneous broadening of the atomic resonance frequency caused by the energy-dependent differential light shift $\hbar\delta_{\text{ls}} = \Delta E_0 - \Delta E_1$ of the individual trapped atoms, see Equations (A.7) and (A.8). Colder atoms spend more time in the bottom of the potential well, so that their differential light shift between state $|0\rangle$ and $|1\rangle$ is larger than for hotter atoms. The energy distribution of the atoms in our dipole trap obeys a three-dimensional Boltzmann distribution with probability density [57]:

$$p(E) = \frac{E^2}{2(k_{\text{B}}T)^3} \exp\left(-\frac{E}{k_{\text{B}}T}\right) \quad (1.33)$$

so that the distribution of the differential light shifts of the trapped atoms reads [72]:

$$\tilde{\alpha}(\delta_{\text{ls}}) = \frac{\beta^3}{2} (\delta_{\text{ls}} - \delta_{\text{ls,max}})^2 \exp[-\beta(\delta_{\text{ls}} - \delta_{\text{ls,max}})] \quad \text{with} \quad \beta(T) = \frac{2U_0}{k_{\text{B}}T\delta_{\text{ls,max}}}, \quad (1.34)$$

Preset pulse parameters		
maximum Rabi frequency	$\Omega_{\max}/2\pi$	28 kHz
amplitude of the frequency sweep	$\delta_{\max}/2\pi$	40 kHz
pulse duration	t_{pulse}	2 ms
Trap parameters		
potential depth	U_0/k_{B}	140 μK
maximum differential light shift (obtained from indep. measurement, Section 2.3.2)	$\delta_{\text{ls,max}}/2\pi$	12 kHz
Fit results		
atom temperature	T	40 μK
maximum population in state $ 1\rangle$	A	95 %
frequency shift	$\delta_{\text{corr}}/2\pi$	1.0 kHz

Table 1.2: Parameters for the spectrum of Figure 1.27 (a).

where T is the temperature of the atoms and $\delta_{\text{ls,max}}$ is the maximum differential light shift in the bottom of the potential well. Note that this equation is only valid in the harmonic approximation of the dipole potential.

In order to model the experimental data, the numerically obtained population transfer efficiency $P_1(\delta_c)$ has to be convoluted with the distribution of differential light shifts:

$$\tilde{P}_1(\delta_c) = \int_{\delta_{\text{ls,max}}}^0 \tilde{\alpha}(\delta_{\text{ls}}) P_1(\delta_c + \delta_{\text{ls}}) d\delta_{\text{ls}}. \quad (1.35)$$

The resulting transfer efficiency $\tilde{P}_1(\delta_c)$ is computed numerically and fitted to the data with two additional parameters, $A \cdot \tilde{P}_1(\delta_c + \delta_{\text{corr}})$. The amplitude A takes into account experimental imperfections during state preparation and detection while the frequency offset δ_{corr} corrects for a shift of the frequency center of the spectrum. This shift is due to the fact that the initial frequency calibration determines the atomic resonance frequency shifted by an average differential light shift which has not yet been accounted for in the numerical calculation. The solid line in Figure 1.27 (a) shows the resulting fit which agrees very well with the experimental data. The fit parameters are listed in Table 1.2.

According to an independent measurement of the differential light shift, see Section 2.3.2, $\delta_{\text{ls,max}}/2\pi = 11.9 \pm 0.7$ kHz for the given trap depth of $U_0 = 140$ μK . The assumption of these values leads to the given fit results. The value of the atom temperature of $T = 40$ μK obtained from the fit is compatible with the temperature measured in previous investigations. The excellent agreement of the theoretical curve with the experimental data shows that our model works very well.

1.8 Conclusion

We have developed a number of tools to control both internal and external degrees of freedom of single neutral atoms. A high-gradient MOT allows us to cool and to capture single cesium atoms the exact number of which we infer from their fluorescence light. They can be transferred with high efficiency into a standing wave dipole trap which provides sub-micrometer localization along its axis and the possibility to transport the atoms over distances up to a centimeter. Molasses cooling in the dipole trap enables us to cool the trapped atoms and to image them by an intensified CCD camera. The current limitations of our cooling technique are set by the multi-mode characteristics of our Nd:YAG dipole trap laser. It induces multi-photon processes together with the molasses lasers and pumps the atom out of the cooling cycle. Nevertheless, careful alignment and properly chosen laser parameters allow us to continuously observe a single trapped atom for half a minute, merely limited by collisions with atoms from the background vapor. The refinement of this technique made it possible to image the controlled motion of a single atom and a string of atoms for the first time.

Initialization and detection of internal atomic hyperfine states is performed by optical pumping and by the application of a state-selective push-out laser, respectively. Both

techniques can reliably be applied to a single or more atoms at a time and have efficiencies exceeding 99 %. For the coherent manipulation of the internal states we use microwave radiation to drive the hyperfine ground state transition on the stretched Zeeman sublevels. Rabi oscillations with excellent fringe visibility demonstrate the preparation of quantum superposition states. Adiabatic passages provide an alternative technique to flip the spin of the atomic qubit. This technique proves to be more robust against frequency drifts than resonant population transfer.

Chapter 2

Experimental realization of a neutral atom quantum register

2.1 Introduction

A quantum register is an essential building block of a quantum computer. It consists of a well known number of qubits each of which can be prepared in a desired quantum state. Write and read operations on a quantum register are performed by coherent one-qubit rotations of individually addressed qubits and by state-selective measurements.

In our case, a string of neutral atoms trapped in different potential wells of the dipole trap serves as quantum register. In an experimental geometry similar to ours, a linear Paul trap, individual ions are coherently manipulated using a tightly focused laser beam [5]. With a spatial addressing resolution of $10\ \mu\text{m}$, selection between different ion qubits is achieved by deflecting it with an acousto-optic deflector. Clouds of neutral atoms have been trapped in a CO_2 -laser optical lattice [73] and in arrays of optical microtraps [74], where a focussed laser beam is also used to address individual trapping sites.

I will present an alternative technique for the individual addressing of atom qubits which works reliably at an addressing resolution as small as $2.5\ \mu\text{m}$. Coherent manipulation of the qubits is performed using microwave radiation as demonstrated in Section 1.6. The individual qubits are selected by application of a linear magnetic field gradient along the trap axis which causes the resonance frequency of the qubit transition to be position dependent. By tuning the microwave frequency accordingly, we spectroscopically resolve the trapped atoms and demonstrate coherent read and write operations on this quantum register. In a different context, a similar technique is routinely used in NMR imaging where magnetic field gradients are applied in order to obtain spatially resolved information on the spectral properties of, e. g., human tissue [75].

The coherence time of the quantum register indicates how long the fragile superposition states survive. It thus sets the time limit for useful quantum computations. A detailed analysis of the coherence properties reveals a coherence time of $600\ \mu\text{s}$ which is two orders of magnitude larger than our operation time of a Hadamard gate.

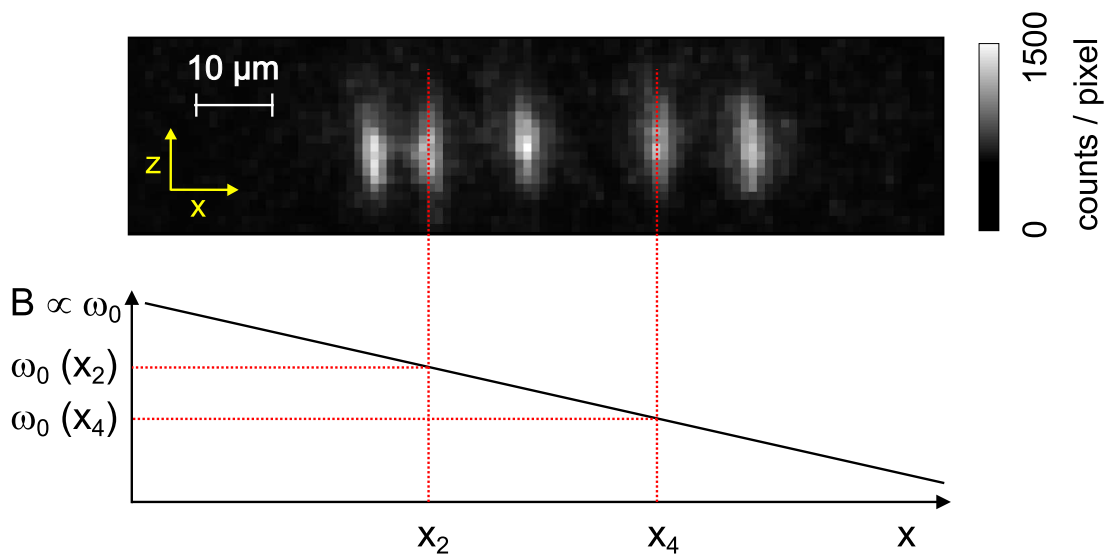


Figure 2.1: Image of a string of five trapped atoms. A magnetic field gradient introduces a position dependent atomic resonance frequency. As an example, addressing of the second and the fourth atom of the string requires knowing the respective resonance frequencies $\omega_0(x_2)$ and $\omega_0(x_4)$.

2.2 Calibration of the position dependent atomic resonance

The position-selective manipulation of the trapped atoms requires precise knowledge about the respective atomic resonance frequencies. In preparation for all single atom addressing experiments presented in this chapter we therefore perform a calibration measurement which determines the resonance frequencies of the trapped atoms as a function of their position along the trap axis.

2.2.1 Magnetic field

Figure 2.1 shows an image of a string of five single atoms trapped in different potential wells of our standing wave dipole trap. It is the same image already depicted in Figure 1.11. In order to spectroscopically resolve these atoms we apply an inhomogeneous magnetic field which introduces a position dependent $|0\rangle \leftrightarrow |1\rangle$ transition frequency. For this purpose we use the MOT coils which produce a quadrupole magnetic field $\mathbf{B}_{\text{quad}}(\mathbf{r})$ whose magnitude increases linearly from the center. In order to avoid state mixing between the atomic Zeeman levels, we additionally apply a homogeneous guiding field \mathbf{B}_0 along the trap axis, see Section 1.5.1. The total magnetic field therefore has the form

$$\mathbf{B}(\mathbf{r}) = \begin{pmatrix} B_x \\ B_y \\ B_z \end{pmatrix} = \mathbf{B}_0 + \mathbf{B}_{\text{quad}}(\mathbf{r}) = \begin{pmatrix} B_0 \\ 0 \\ 0 \end{pmatrix} + B' \cdot \begin{pmatrix} x \\ y \\ -2z \end{pmatrix}, \quad (2.1)$$

where B' denotes the magnitude of the gradient field. Since the dipole trap is aligned onto the MOT which runs close to the zero point of the quadrupole field ($x = y = z = 0$),

the dipole trap is on the axis ($y = 0, z = 0$) so that the transition frequency between $|0\rangle \equiv |F = 4, m_F = -4\rangle$ and $|1\rangle \equiv |F = 3, m_F = -3\rangle$ of the trapped atoms increases linearly with x :

$$\omega_0(x) = \Delta_{\text{HFS}} + \delta_0 + \omega'x . \quad (2.2)$$

Here, the frequency shift due to the homogeneous magnetic guiding field is labelled δ_0 , and the magnitude of the position dependent frequency shift is denoted by $\omega' = (3g_3 - 4g_4)\mu_B B'/\hbar$. A guiding field of $|\mathbf{B}_0| = 4$ G causes a frequency shift of $\delta_0/2\pi = -9.8$ MHz, while the gradient field of typically $B' = 1.5$ mG/ μm results in a shift of $\omega'/2\pi = 3.7$ kHz/ μm .

2.2.2 Experimental sequence

For a precise calibration of $\omega_0(x)$ we use trapped atoms as a probe. Initially, we determine δ_0 by recording a spectrum in the homogeneous magnetic field \mathbf{B}_0 , see Section 1.6.3. Then, we measure ω' in the gradient field by loading a large atom cloud into the dipole trap, initializing it in state $|0\rangle$, and applying a microwave π pulse with a fixed frequency ω_{MW} . After state-selective detection the atoms only remain trapped at the position that was resonant with the microwave pulse. By repetition of this measurement at different microwave frequencies we calibrate the position as a function of the microwave frequency, $x(\omega_{\text{MW}})$, from which we can infer ω' and δ_0 .

In the first step, we load a large number of about 50 atoms into the dipole trap. After the transfer from the MOT, their spatial distribution only extends over the MOT size of roughly 10 μm diameter. We broaden their distribution within the dipole trap to $2\sigma_{\text{tof}} = 60$ μm by switching off one of the two trap laser beams for 1 ms, see Section 1.3.4. Under continuous illumination by the optical molasses we then image the trapped atoms with an integration time of 500 ms, see Figure 2.2 (a). Due to the large number of atoms, the average separation between individual atoms is too small to be resolved. In order to cool the trapped atoms as long as possible, the molasses lasers are switched off only after the CCD chip has been read out which takes 400 ms. Now we switch on the magnetic field $\mathbf{B}(\mathbf{r})$. To create the gradient field we run a current of 1.3 A through the MOT coils which corresponds to roughly one tenth of the current during MOT operation. After initializing the atoms in state $|0\rangle$ by optical pumping, we apply a microwave π pulse with a pulse duration of $t_{\text{pulse}} = 200$ μs at the frequency $\Delta_{\text{HFS}} + \delta_0$. The state-selective push-out laser then removes all atoms from the trap that have remained in $|0\rangle$. A subsequently taken image with an exposure time of 500 ms, see Figure 2.2 (b), indeed reveals the presence of atoms in an area of 3 μm diameter. Its center corresponds to the position $x = 0$, according to Equation (2.2).

For a better signal-to-noise ratio we repeat this sequence 20 times and add up all initial and all final images. To analyze the resulting two images we follow the procedure introduced in Section 1.3.4. After suitably clipping the images to minimize the background noise, we bin the pixels of the pictures along the vertical z direction to obtain histograms for the intensity distribution along the trap axis x . The resulting histogram of the initial image shows a homogeneous distribution over the entire trapping region (Figure 2.2 (a)). In

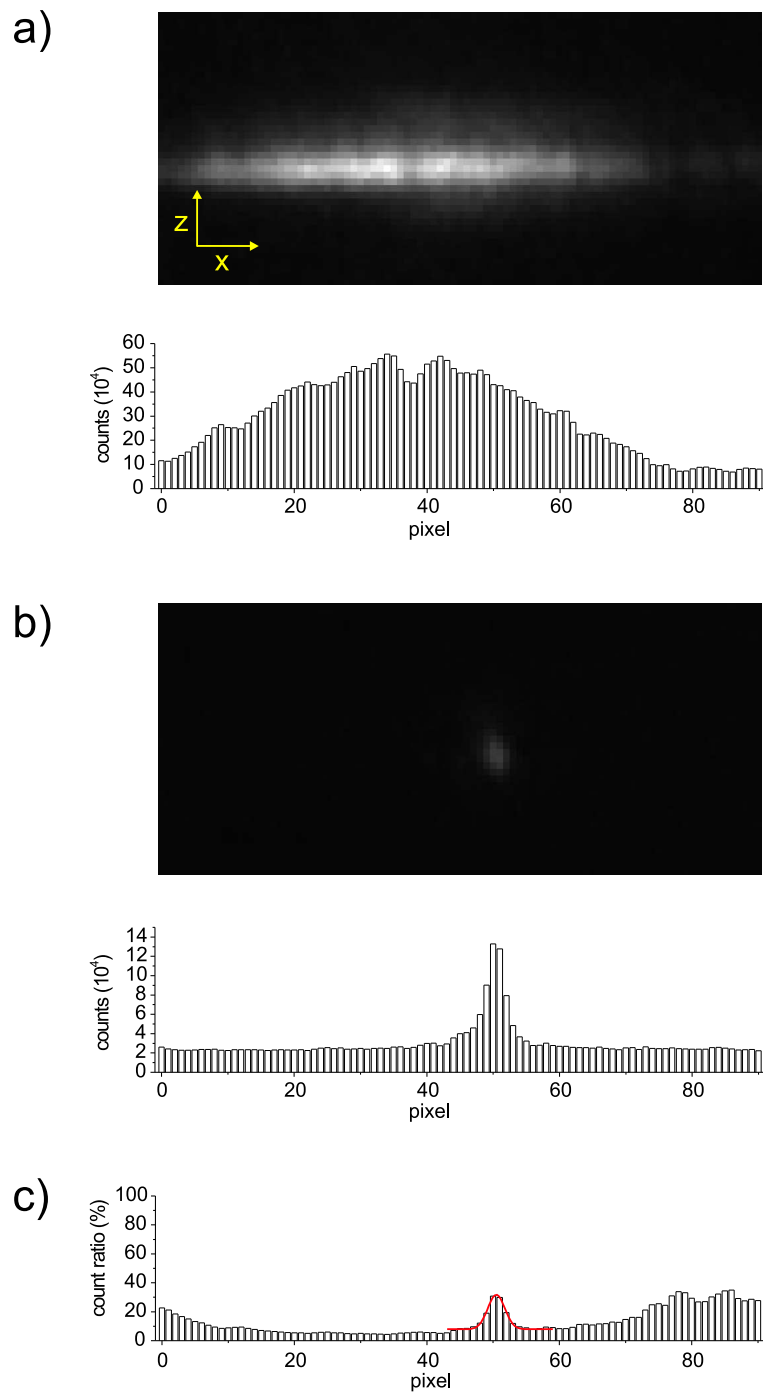


Figure 2.2: Image analysis for frequency calibration. a) The picture shows 20 added images (exposure time: 0.5 s) of an atom cloud in the dipole trap of 50 atoms each. b) This picture shows 20 added images after application of a π pulse and state-selective atom removal from the trap. Only the atoms resonant with the microwave pulse are left. The histograms in (a) and (b) show the respective binned intensity distributions. c) Division of the second histogram (b) by the initial distribution (a) yields the normalized intensity distribution. The line is a Gaussian fit according to Equation (2.3).

order to normalize the atom distribution after state-selective detection (Figure 2.2 (b)) onto the initial distribution of atoms, we divide the histogram of the final image by the one of the initial image.

The resulting intensity distribution (Figure 2.2 (c)), corresponds to a convolution of a Fourier-limited π pulse spectrum (Figure 1.21) with the intensity distribution of a single atom image (Figure 1.10 (b)). We determine its center x_c by fitting the same Gaussian function as in Equation (1.15):

$$I(x) = B + A \exp\left(-\frac{(x - x_c)^2}{2\sigma_x^2}\right) \quad (2.3)$$

The resulting fit parameters are listed in Table 2.1.

position	x_c	50.5 ± 0.1 pixel
width	σ_x	1.3 ± 0.1 pixel
offset	B	7.9 ± 0.4 %
amplitude	A	24 ± 1 %

Table 2.1: Fit results for the normalized intensity distribution of Figure 2.2 (c), according to Equation (2.3).

The π pulse time and the corresponding microwave power of the Fourier-limited pulse were chosen such that the width of the intensity distribution σ_x is not significantly broader than the width of a single atom image in the dipole trap $\sigma_x(DT) = 1.24 \pm 0.16$ pixel. The $1/\sqrt{e}$ -width of the respective pulse spectrum in frequency space is 1.9 kHz and corresponds to $w_{\text{spec}} = 0.5$ pixel using the calibration result below. The expected width of the intensity distribution $\sigma_x = \sqrt{\sigma_x(DT)^2 + w_{\text{spec}}^2} = 1.3 \pm 0.2$ pixel agrees well with the measured width of $\sigma_x = 1.3 \pm 0.1$ pixel.

Due to the fact that the spectral pulse width is smaller than the width of a single atom image, the amplitude of the normalized intensity distribution is small. The resonance frequency of atoms trapped at a site which is, e. g., two pixels away from x_c , is detuned from the microwave frequency far enough so that no spin flip occurs. However, their fluorescence still contributes to the histogram counts of Figure 2.2 (a) at the position x_c . This additional background of the reference image significantly decreases the amplitude of the normalized intensity distribution.

2.2.3 Result

To measure the position as a function of the atomic resonance frequency we repeat the entire procedure described above for different microwave frequencies. The result is plotted in Figure 2.3 and reveals a purely linear dependence, as expected. From the slope of the linear fit we infer the position-dependent frequency shift to be $\omega'/2\pi = 3.480 \pm 0.007$ kHz/pixel = 3.71 ± 0.03 kHz/ μm . The magnetic field gradient is therefore $B' = -1.51 \pm 0.01$ mG/ μm

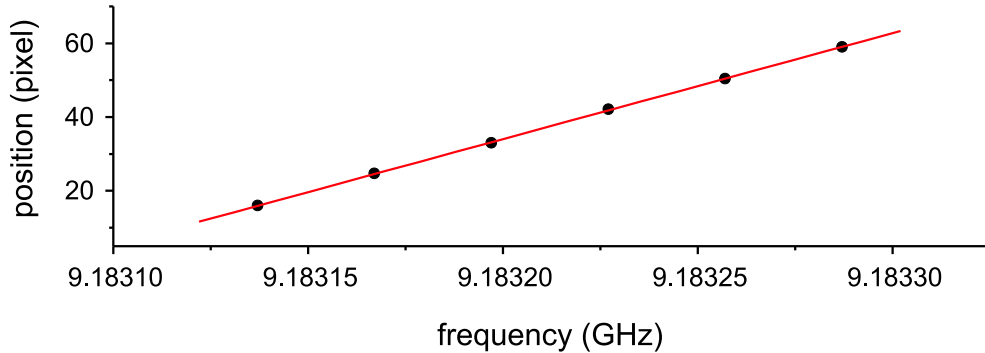


Figure 2.3: Calibration of the atomic resonance frequencies. Each data point shows the center position of a fitted intensity distribution as in Figure 2.2 (c). The error bars are too small to be displayed here. From the slope of the linear fit we infer $\omega'/2\pi = 3.71 \pm 0.03$ kHz/ μm .

which is compatible with the expected gradient of -1.4 ± 0.1 mG/ μm , calculated from the applied current of 1.3 ± 0.1 A [54].

2.3 Position-selective quantum state preparation

The manipulation of the quantum register requires the addressing of individual atoms within a string of trapped atoms. Since each time new atoms are loaded from the MOT, they are located at random positions. We therefore implement a computerized feedback scheme which determines the resonance frequencies of the atoms and programs the microwave source accordingly.

2.3.1 Addressing of a single atom

To carry out single qubit operations on the quantum register, we first take an image of the trapped atom string. The image is then automatically analyzed by a computer program such that the positions of all optically resolved atoms are determined. Using the results of a previously performed calibration measurement, the resonance frequency of the atom to be addressed is calculated and sent to the microwave source. The microwave radiation now interacts only with the selected atom while leaving the neighboring atoms untouched. A schematic overview of the experimental setup is shown in Figure 2.4.

Image analysis

In order to determine the positions of the atoms in the register, we analyze their images by a computer program written by one of my co-workers, Yevhen Miroshnychenko. Figure 2.5 (a) shows a typical picture with three trapped atoms (exposure time: 0.5 s). First, the image is binned vertically to yield the intensity distribution along the trap axis, see Figure 2.5 (b). In the resulting histogram, the positions of all atoms are identified using the following algorithm. We initially define a threshold value ($N_{\text{thr}} = 18000$ in this case)

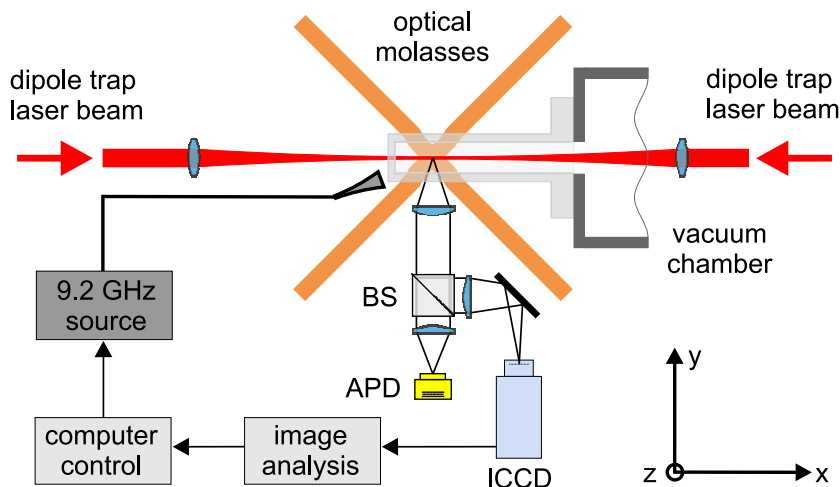


Figure 2.4: Experimental setup for single atom addressing. While the trapped atoms are illuminated by the optical molasses, an ICCD image is acquired. Subsequent analysis of this image determines the positions of the atoms and their resonance frequencies. The microwave source is then accordingly programmed by the computer control so that coherent manipulation of a selected atom qubit can be performed.

for the minimum number of counts per pixel column above background noise, and a value for the half-width of a histogram peak ($w_{\text{peak}} = 3$). First, the highest histogram bar above N_{thr} is identified, in this illustration at the position $\tilde{x}_1 = 73$. Now, all histogram values from $\tilde{x}_1 - w_{\text{peak}}$ to $\tilde{x}_1 + w_{\text{peak}}$ are set to zero, see Figure 2.5 (c). These two steps are repeated until all bars are smaller than N_{thr} , see Figure 2.5 (e). In this way, two further peaks are identified at $\tilde{x}_2 = 59$ and $\tilde{x}_3 = 49$, see Figures 2.5 (c) and (d). To make sure that a detected fluorescence peak at position \tilde{x}_c corresponds to exactly one atom rather than two or more atoms, the total number of counts within each fluorescence peak $N_{\text{tot}} = \sum_{\tilde{x}_i=\tilde{x}_c-w_{\text{peak}}}^{\tilde{x}_c+w_{\text{peak}}} N(\tilde{x}_i)$ is calculated, where $N(\tilde{x}_i)$ denotes the number of counts in column \tilde{x}_i . Since N_{tot} is typically $(1.5 \pm 0.22) \cdot 10^6$ for a single atom, we discard peaks with N_{tot} larger than $1.9 \cdot 10^6$. For the case of exactly two atoms, I calculate from the width of the atom distribution of $2\sigma_{\text{tof}} = 60 \mu\text{m}$, that such an atom pair is optically not resolved in 6 % of the cases.

In a next step, the positions of all optically resolved atoms are determined with higher precision. For this purpose, the computer program calculates the center of mass x_c for every fluorescence peak:

$$x_c = \frac{1}{N_{\text{tot}}} \sum_{\tilde{x}_i=\tilde{x}_c-w_{\text{peak}}}^{\tilde{x}_c+w_{\text{peak}}} \tilde{x}_i N(\tilde{x}_i). \quad (2.4)$$

For this illustration, the scheme yields the values $x_1 = 72.9 \pm 0.1$ pixel, $x_2 = 58.7 \pm 0.1$ pixel, and $x_3 = 49.0 \pm 0.1$ pixel. The precision of $\Delta x_c = \pm 0.1$ pixel is sufficient for all experiments described in this thesis. This error is calculated by applying the law of error propagation to Equation (2.4), where $N(\tilde{x}_i)$ is replaced by the number of photons

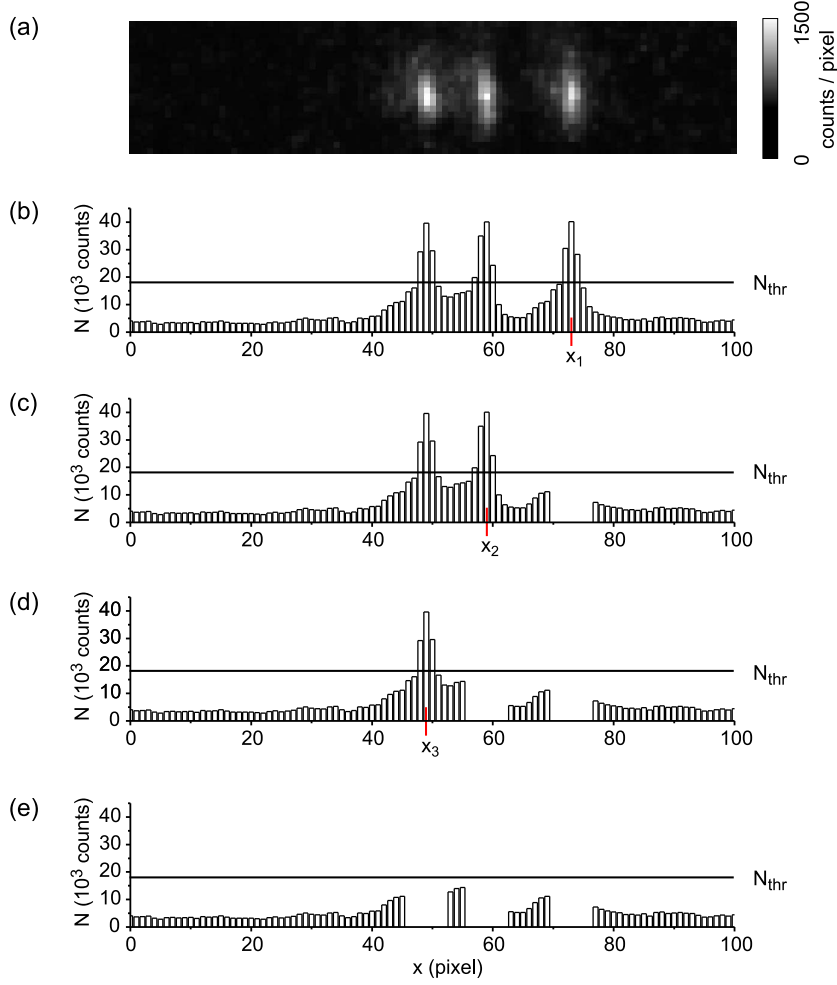


Figure 2.5: Image analysis of a three atom string. To determine the positions of the atoms along the trap axis, their image (a) is binned vertically. In the resulting histogram (b) the largest bar (\tilde{x}_1) above a threshold value of $N_{\text{thr}} = 18000$ is identified. Then, the histogram values from $\tilde{x}_1 - w_{\text{peak}}$ to $\tilde{x}_1 + w_{\text{peak}}$ are set to zero (c) and the procedure is repeated until all bars are smaller than N_{thr} (d, e).

$N' = N(\tilde{x}_i)/390$ counts/photon, see Section 1.3.1. For N' , Poissonian statistics then yields an error of $\Delta N' = \sqrt{2N'}$ where the factor of two takes into account the additional noise due to the amplification by the multi-channel electron multiplier of the ICCD [76].

Feedback to the microwave source

In this illustration we choose to address the second atom of the string. For this purpose, the computer calculates the resonance frequency $\omega(x_2)$ corresponding to the second peak of the histogram, using Equation (2.2). The position dependent frequency shift ω' has been calibrated as described in Section 2.2 and the position x_2 has been determined from

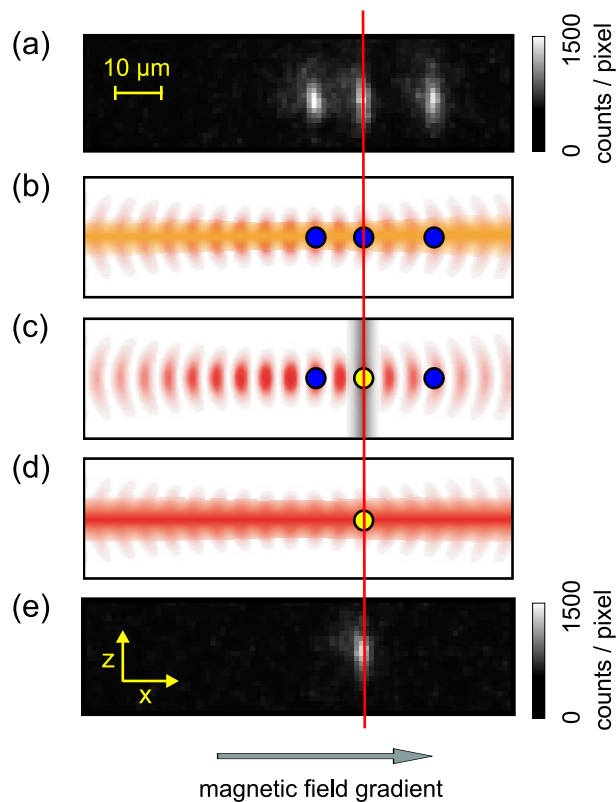


Figure 2.6: Addressing an individual atom. (a) Image of a string of three atoms. (b) Initialization of the register in $|000\rangle$ by optical pumping. (c) A π pulse at the resonance frequency of the second atom switches the register to state $|010\rangle$. (d) The push-out laser removes all atoms in $|0\rangle$ from the trap. (e) A final image reveals the presence of the middle atom in the trap. The period of the standing wave dipole trap in (b) – (d) is stretched for illustration.

the fit above.

The entire automated procedure described so far is performed by the camera computer which controls and reads out the ICCD and analyzes the acquired images. It sends the resulting number $\omega(x_2)$ to the central control computer. This computer is responsible for the timing of the entire experimental procedure, see Section 1.1.2. It programs the microwave source to change its frequency to $\omega(x_2)$ via a GPIB-interface. Now the synthesizer is ready to create a microwave signal at that frequency whenever it receives a trigger pulse.

After an image of the trapped atoms has been taken by the ICCD, it takes a total time of roughly 400 ms until the microwave source is programmed to the new frequency. Most of this time is needed for read-out of the CCD-chip and transfer of the data to the camera computer. For the area of $22 \times 100 \text{ pixel}^2$ shown in Figure 2.5 (a), the data transfer takes 300 ms. Binning and determination of the atom positions and the corresponding

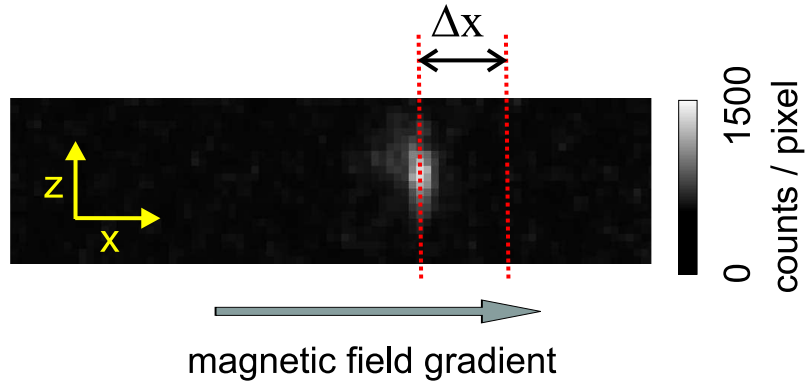


Figure 2.7: Measurement of the addressing resolution. A single atom in the dipole trap is subjected to a π pulse. The microwave frequency is set such that it is resonant with a position at the distance Δx away from the atom.

frequencies only requires 5 ms. Transmission of this information to the control computer takes another 20 ms, and another 50 ms are needed to program the microwave synthesizer. To ensure that all of these steps are completed before the experimental procedure is continued, we usually wait for 600 ms after exposure until the trapped atoms are subjected to any microwave pulses. During this time, we continuously cool the atoms with the optical molasses.

Addressed spin flip

To illustrate our addressing scheme, we now perform a spin flip on the center atom of the string (Figure 2.6 (a)). After the optical molasses has been switched off, we apply the magnetic field $\mathbf{B}(\mathbf{r})$ of Equation (2.1) and lower the dipole trap to 100 μK . Then the optical pumping laser is shined in along the trap axis to initialize the register in $|000\rangle = |0\rangle_1 |0\rangle_2 |0\rangle_3$, where the subscript denotes the atom number (Figure 2.6 (b)). A microwave π pulse flips the spin of the center atom (Figure 2.6 (c)) and thus switches the register state to $|010\rangle$. For state-selective detection the push-out laser removes all atoms remaining in state $|0\rangle$ from the trap (Figure 2.6 (d)). Now we switch off the magnetic field and increase the trap depth to its initial value. Under continuous illumination by the optical molasses, we take a second picture with an exposure time of 0.5 s. As expected, atom 2 is present in Figure 2.6 (e), while atoms 1 and 3 have been removed.

2.3.2 Addressing resolution

Experimental sequence

In order to characterize the performance of this addressing scheme we determine its resolution, i. e. the minimum distance between adjacent atoms necessary for selective addressing. For this purpose, we trap only one atom at a time in our dipole trap. After initializing the atom in state $|0\rangle$ and determining its position and resonance frequency ω_0 , we apply a π pulse to the atom (Figure 2.7). We detune the frequency of this microwave pulse

ω_{MW} from ω_0 and record the population transfer from $|0\rangle$ to $|1\rangle$ as a function of this detuning $\delta = \omega_{\text{MW}} - \omega_0$, which corresponds to a position offset $\Delta x = \delta/\omega'$ according to Equation (2.2). After application of the microwave pulse, we subject the atom to the state-selective push-out laser. In contrast to the illustration in Figure 2.6, we do not reveal the presence or absence of the atom by acquiring a second image, but by transferring it back to the MOT where we detect its fluorescence. Detection in the MOT is much faster and therefore saves hours of measurement time since many repetitions are required for good statistics.

Microwave pulse

The microwave pulse has a Gaussian shaped envelope resulting in a Rabi frequency of

$$\Omega_{\text{R}}(t) = \Omega_{\text{max}} \exp\left(-\frac{(t - t_{\text{pulse}}/2)^2}{2\sigma_{\tau}^2}\right), t = 0..t_{\text{pulse}} \quad (2.5)$$

For fixed pulse width $2\sigma_{\tau}$ and pulse duration t_{pulse} , we initially optimize the maximum amplitude Ω_{max} to fulfil the π pulse condition $\int_0^{t_{\text{pulse}}} \Omega_{\text{R}}(t') dt' = \pi$. This is accomplished by fine-tuning the microwave power to achieve a maximum population transfer close to 100 %. The amplitude modulation is externally controlled via the AM input of the Agilent microwave synthesizer. Since its dynamic range is only 20 dB, the total pulse duration t_{pulse} is chosen such that $\Omega_{\text{R}}(0) = \Omega_{\text{R}}(t_{\text{pulse}}) = \Omega_{\text{max}}/10$.

We choose a Gaussian rather than a rectangular pulse shape as above because the frequency spectrum of this pulse falls off exponentially from the carrier frequency. The sharp edges of a rectangular pulse produce sinc-like AM sidebands whose amplitudes fall off quadratically.

Results

The result of this measurement is shown in Figure 2.8 (a)–(c) for different durations of the microwave pulse. For every data point we performed a total of 100 runs. Due to the Poissonian distribution of atom numbers initially captured by the MOT, on average 37 % of all experimental runs are actually performed with exactly one atom when the MOT loading time is optimized to capture one atom on average. All single atom events are post-selected, so that every data point is obtained from roughly 40 single atom measurements.

The measured data for resonant addressing show that for a pulse width of up to $2\sigma_{\tau} = 35.4 \mu\text{s}$, the maximum population transfer efficiency is $P_{\text{max}} = 98.7_{-3.0}^{+1.1}$ %. This number is obtained by averaging the two central data points of the spectra in Figure 2.8 (a) and (b). This efficiency includes all experimental imperfections: losses during transfer of the atom between the two traps and during illumination of the atom in the dipole trap, imperfect state initialization by optical pumping, and erroneous detection of the atomic state.

Due to the narrowing Fourier spectrum of the corresponding π pulses, the spatial interval of significant population transfer decreases with increasing pulse duration. A pulse of length $2\sigma_{\tau} = 70.7 \mu\text{s}$, see Figure 2.8 (c), swaps the state of an atom at one position while

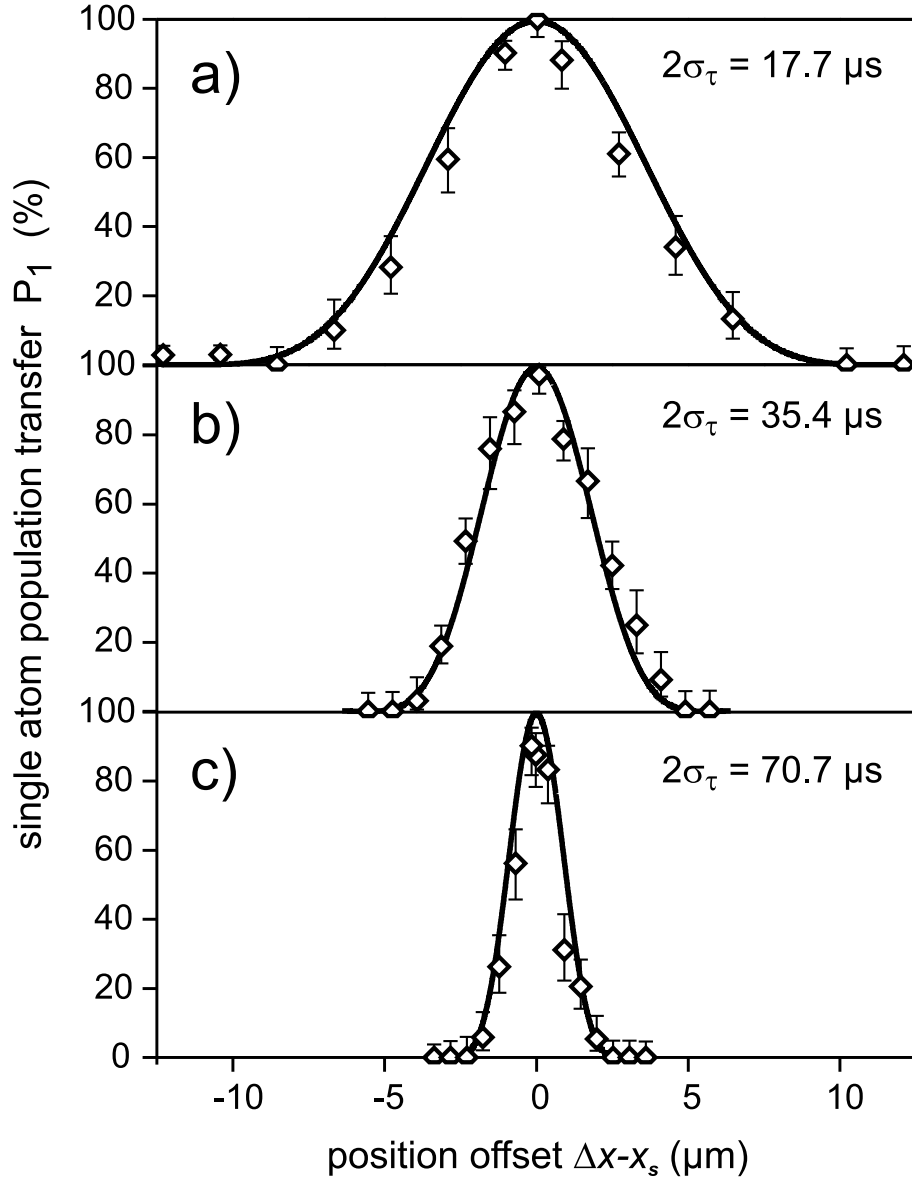


Figure 2.8: Resolution of our single atom addressing scheme. The data points show the population transfer efficiency of an atom being exposed to a microwave π pulse resonant with a position Δx away from the calculated atom position. Each point consists of approximately 40 single atom events. Resonant addressing reveals a spin flip efficiency of close to 100 %. The measured data are in good agreement with a numerical calculation (solid lines). The pulse parameters and the results of the calculation are listed in Table 2.2.

an atom trapped at a site $2.5 \mu\text{m}$ away remains in its initial state with a probability of $100_{-2.7}^{+0} \%$.

Since the functional shape of the spectra cannot be derived analytically, we numerically integrate the optical Bloch equations (1.18) with the time-dependent torque vector $\mathbf{\Omega}(t) \equiv (\Omega_R(t), 0, \delta)$, according to Equation (2.5). The solid lines in Figure 2.8 show the result of this simulation with no adjusted parameters and demonstrate that the measured spectra are in very good agreement with the theoretical prediction.

The shape of the spectra is close to Gaussian. We therefore define the spectral width $\sigma_{\Delta x}$ as the position offset where the population transfer has decreased to $P_1(\sigma_{\Delta x}) = P_{\max}/\sqrt{e}$. It corresponds to the width $\sigma_\delta = \omega' \sigma_{\Delta x}$ in frequency space. The respective values for all three spectra are summarized in Table 2.2.

The addressing resolution is a measure for how close two atoms can be brought together such that the spin of one atom is flipped while the population transfer of the neighboring atom is negligible. We therefore define the addressing resolution σ_{add} as the position offset with $P_1(\sigma_{\text{add}}) = 0.1 \%$. For the narrow spectrum shown in Figure 2.8 (c), the addressing resolution is as small as $2.5 \mu\text{m}$.

The predominant limitation for the addressing resolution are slow drifts of the intensity and the polarization of the dipole trap laser beams which change the atomic resonance frequency by up to 1 kHz/h corresponding to $0.3 \mu\text{m/h}$. Their origin will be discussed in detail below. Since the presented spectra were recorded without intermediate calibration

Figure		2.8 (a)	2.8 (b)	2.8 (c)
microwave pulse				
pulse duration	t_{pulse}	38 μs	76 μs	152 μs
pulse width	$2\sigma_\tau$	17.7 μs	35.4 μs	70.7 μs
peak Rabi frequency	$\Omega_{\max}/2\pi$	22.4 kHz	11.2 kHz	5.6 kHz
spectrum				
spectral width, in space	$\sigma_{\Delta x}$	3.5 μm	1.7 μm	0.87 μm
$\hat{=}$ spectral width, in frequency	$\sigma_\delta/2\pi$	12.8 kHz	6.4 kHz	3.2 kHz
addressing resolution	σ_{add}	10.2 μm	5.1 μm	2.5 μm
position shift	x_s	1.1 μm	2.1 μm	3.4 μm
$\hat{=}$ frequency shift	$\delta_s/2\pi$	3.9 kHz	7.7 kHz	12.6 kHz
maximum population transfer (obtained from individual data points)	P_{\max}	$100_{-5}^{+0} \%$	$98_{-5}^{+2} \%$	$90_{-8}^{+5} \%$

Table 2.2: Summary of the microwave pulse parameters and the results of the numerical calculation for the spectra in Figure 2.8.

measurements of the atomic resonance frequency during the 10-hour data acquisition time, their centers have to be corrected for a position shift of x_s which corresponds to a frequency shift of $\delta_s = \omega' x_s$. At the present stage, operation of the quantum register at the resolution of $2.5 \mu\text{m}$ therefore requires a calibration measurement every two hours.

We have demonstrated reliable addressing of single atoms with high efficiency. Limited by drifts of the atomic resonance frequency, an addressing resolution of up to $2.5 \mu\text{m}$ can be achieved, with the drawback of long spin flip times of $70.7 \mu\text{s}$. However, since the spectra are Fourier limited, the single qubit gate operation time is inversely proportional to the addressing resolution. Therefore, if the addressing resolution is required to be only $10 \mu\text{m}$, the speed of the gate operation is increased by a factor of four to $17.7 \mu\text{s}$.

Experimental limitation: vector light shift

The drifts of the atomic resonance frequency are caused by slow variations of the intensity and the polarization of the dipole trap laser beams. They result in a drift of the vector component of the light shift of the atomic states. Since it linearly depends on the Zeeman state m_F according to Equation (A.8), it affects the atomic resonance frequency for our microwave transition.

We measured the fraction of circularly polarized light in our dipole trap by performing spectroscopy on the qubit transition for different trap depths. If there is an intensity imbalance between right and left circularly polarized light the total intensity reads:

$$I_{\text{tot}} = I_{\pi} + \varepsilon I_{\sigma\pm}, \quad (2.6)$$

with I_{π} denoting the intensity of the linearly polarized light and $\varepsilon I_{\sigma\pm}$ the fraction of either right or left circularly polarized light, with $\varepsilon \ll 1$. It causes the light shift to be m_F dependent according to Equation (A.8):

$$\Delta E(m_F) = \Delta E_{\pi} + \varepsilon \Delta E_{\sigma\pm}(m_F). \quad (2.7)$$

The resulting differential light shift of the qubit transition $\Delta E_{\text{diff,tot}}$ therefore has a scalar contribution $\Delta E_{\text{diff,sc}}$ arising from the linearly polarized trapping light, and a vectorial contribution $\Delta E_{\text{diff,vec}}$ from the circular polarization:

$$\Delta E_{\text{diff,tot}} = \Delta E_{\text{diff,sc}} + \varepsilon \Delta E_{\text{diff,vec}} \quad (2.8)$$

$$\text{with } \Delta E_{\text{diff,sc}} = \Delta E_{\pi}(F=4) - \Delta E_{\pi}(F=3), \quad (2.9)$$

$$\Delta E_{\text{diff,vec}} = \Delta E_{\sigma\pm}(F=4, m_F=-4) - \Delta E_{\sigma\pm}(F=3, m_F=-3). \quad (2.10)$$

According to Equation (A.7), the scalar differential light shift in a π -polarized trap of 1 mK amounts to $\Delta E_{\text{diff,sc}}/h = -3 \text{ kHz}$. A purely σ^+ -polarized dipole trap of the same depth yields a differential light shift of $\Delta E_{\text{diff,vec}}/h = -3.4 \text{ MHz}$, according to Equation (A.8).

Figure 2.9 shows the measured atomic resonance frequency as a function of the total trapping laser power P . The data are obtained by recording Fourier-limited spectra of the

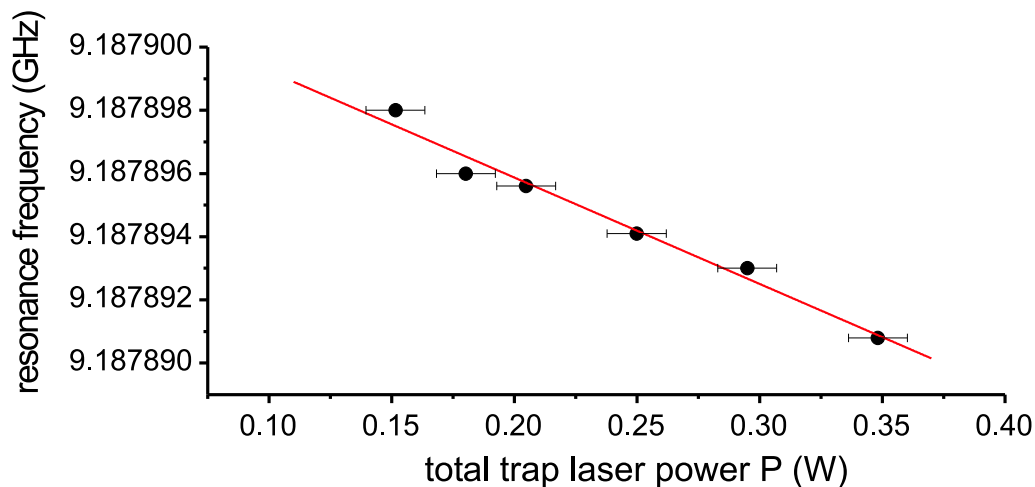


Figure 2.9: Measurement of the differential light shift of the qubit transition. We record Fourier-limited spectra with a π pulse time of $200 \mu\text{s}$ for different trapping laser powers. Here, the atomic resonance frequencies obtained from this measurement are plotted. The total differential light shift obtained from the linear fit is dominated by the circularly polarized contributions of the trapping laser beams.

$|0\rangle \leftrightarrow |1\rangle$ transition with a π -pulse time of $200 \mu\text{s}$ in a homogeneous magnetic guiding field of 2 G. The linear fit has a slope of $-34 \pm 2 \text{ kHz/W}$ and therefore yields a differential light shift of $\Delta E_{\text{diff,tot}}/h = -85 \pm 5 \text{ kHz}$ in a trap of 1 mK, see Section 1.2.2. Since the scalar contribution $\Delta E_{\text{diff,sc}}$ is negligible, the vectorial part $\varepsilon \Delta E_{\text{diff,vec}}/h$ dominates the total differential light shift. Our measurement therefore yields a σ^+ -polarized fraction of the total intensity of $\varepsilon = 2.4 \pm 0.1 \%$.

In our setup, both trapping laser beams are linearly polarized using Glan-laser polarizers with a measured extinction ratio of 10^{-3} , but the measured circularly polarized component in the trap is much larger. Most likely, this effect is caused by birefringence of both the glass cell and the window of the vacuum chamber, and by a small angle between the polarization vectors of the two counter-propagating trapping beams. Moreover, the 8 mm aperture of the polarizers does not allow us to place them into the expanded trapping beam close to the vacuum chamber. Therefore, the three mirrors and three lenses between the polarizers and the glass cell also contribute to the degradation of the polarization.

We typically perform our experiments in a lowered trap of $100 \mu\text{K}$. In such a trap, a change of the circularly polarized intensity of 1 % results in a drift of the atomic resonance frequency of 3.4 kHz. However, during a measurement sequence, we initially observed drifts of up to 20 kHz/h. We identified the central polarizing beam splitter cube, which separates the Nd:YAG laser beam into the two trapping beams, as a likely source of these drifts. It is operated at its damage threshold of $I_{\text{thr}} = 2 \text{ kW/cm}^2$. Since it consists of two prisms which are connected by a possibly birefringent glue, a temperature change due to the high laser power could cause phase shifts of the output polarizations. In addition to polarizing each trapping laser beam with Glan-laser polarizers, we counteract these phase

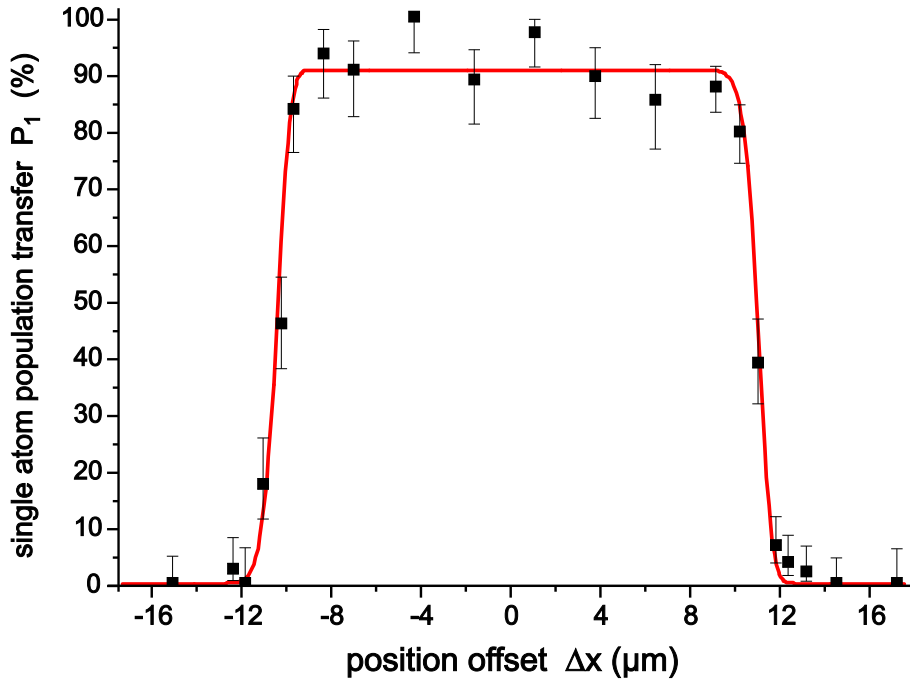


Figure 2.10: Adiabatic spin flip of single register qubits. The spectrum shows the population transfer of a single atom via an adiabatic passage as a function of the position offset Δx along the trap axis. Every data point is obtained from about 40 single atom measurements. The solid line shows the result of a numerical calculation according to Equation (1.35). The parameters are summarized in Table 2.3.

shifts by placing wave plates into each arm and aligning them for maximum transmission through the polarizers every three hours during a measurement. These improvements reduce the frequency drifts to the tolerable value of 1 kHz/h. A long-term improvement would be the replacement of the polarizing beam splitter cube by a non-polarizing beam splitter plate with a larger damage threshold.

2.3.3 Position-selective adiabatic population transfer

While it is essential to improve the experimental hardware such that the drifts of the atomic resonance frequency are reduced, it is advantageous to use a technique which is intrinsically more robust. As presented in Section 1.7, adiabatic passages provide an alternative way of effectively flipping the spin of an atom while being much less sensitive to frequency drifts than resonant population transfer.

Experimental sequence

We combine our addressing technique of Section 2.3.1 with the technique of adiabatic population transfer presented in Section 1.7 to demonstrate a robust way to perform spin flips of individual qubits of our quantum register [70]. As before, a single atom in the

dipole trap is imaged and initialized in state $|0\rangle$. Now, in the magnetic field gradient B' , we apply an adiabatic frequency sweep, with the pulse shape of Equation (1.30) and the pulse parameters of Table 1.2. We then record the single atom population transfer P_1 as a function of the central detuning δ_c , which corresponds to a position offset $\Delta x = \delta_c/\omega'$ along the trap axis.

Spectrum of a single qubit spin flip by an adiabatic passage

The recorded spectrum is shown in Figure 2.10. As above, every data point is obtained from 100 repetitions of the experimental sequence, from which we post-select roughly 40 measurements with exactly one atom present. As expected, the spectrum has a broad plateau with a spin flip efficiency above 90 %. At the edges, this efficiency rapidly drops to zero. While the addressing resolution $\sigma_{\text{add}} \approx 13 \mu\text{m}$ is comparable to the one of the π -pulse spectrum in Figure 2.8 (a), the regime of high-efficiency population transfer extends over an interval of $18 \mu\text{m}$ and is much larger than for resonant spin flips with the same addressing resolution. Considering typical total measurement times of 20 hours, the demonstrated technique is therefore robust against the observed frequency drifts of 1 kHz/h.

Trap parameters		
potential depth	U_0/k_B	85 μK
maximum differential light shift (obtained from indep. measurement, Section 2.3.2)	$\delta_{\text{ls,max}}/2\pi$	7.2 kHz
Fit results		
atom temperature	T	25 μK
maximum population in state $ 1\rangle$	A	91 %
frequency shift	$\delta_{\text{corr}}/2\pi$	3.3 kHz

Table 2.3: Fit parameters for the spectrum of Figure 2.10.

While the parameters for the microwave pulse are identical to the ones of the recorded spectrum of an adiabatic passage in a homogeneous magnetic guiding field (Section 1.7), the trap parameters are slightly different, see Table 2.3. Assuming a lower atom temperature of $T = 25 \mu\text{K}$ due to the lowered trap depth, I have plotted the expected theoretical curve (solid line) into the spectrum of Figure 2.10, according to Equation (1.35). It agrees very well with the experimental data. The reduction of the maximum population in the final state $|1\rangle$, see Table 2.3, as compared to the measurements presented in Section 2.3.2 is probably due to imperfect state initialization. Unless the optical pumping laser used for initialization is circularly polarized with a purity of $1 - 10^{-4}$, the optical pumping efficiency to state $|0\rangle$ drops significantly below 100 %. Since its polarization has not been optimized for several months before the measurement presented here, it is probable that it causes the reduced maximum population in the final state. As in Section 2.3.2, the frequency shift δ_{corr} takes into account that the initial frequency calibration determines

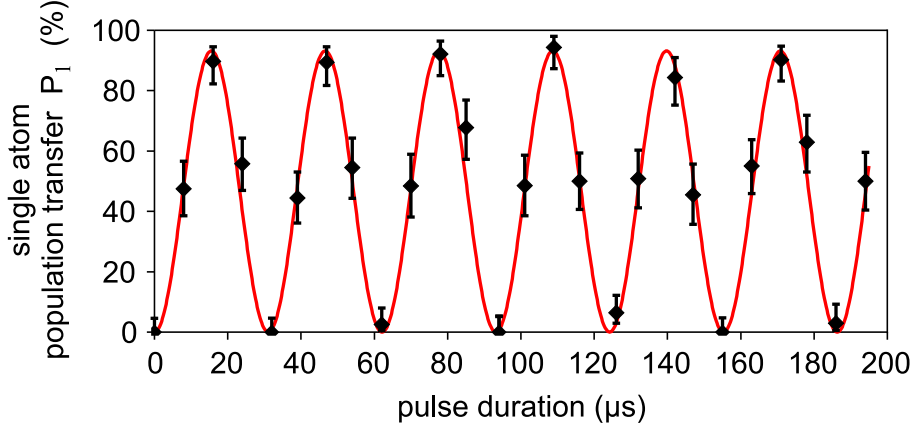


Figure 2.11: Demonstration of qubit rotations of individually addressed single atoms. Each point shows the averaged population transfer of approximately 40 single atom events. The Rabi oscillations have an excellent contrast of $C = 99.1^{+0.9}_{-3.7}\%$.

the atomic resonance frequency shifted by an average differential light shift which is not considered in the numerical calculation.

2.3.4 Rabi rotations

To demonstrate the preparation of quantum register states we perform arbitrary qubit rotations. Similar to the measurement of the addressing resolution in Section 2.3.2, we trap, image, and initialize one atom qubit in state $|0\rangle$. This time, for experimental simplicity, we apply a resonant square microwave pulse of duration t_{pulse} and measure the transfer probability to state $|1\rangle$. It is plotted in Figure 2.11 as a function of t_{pulse} . Since we perform 100 experimental runs for each pulse duration, every data point is deduced from approximately 40 single atom events after post-selection.

The signal shows Rabi oscillations of the population between states $|0\rangle$ and $|1\rangle$. As in Section 1.6.4, it is fitted using the following function:

$$P_1(t_{\text{pulse}}) = P_{\min} + \frac{P_{\max} - P_{\min}}{2} (1 - \cos(\Omega_R t_{\text{pulse}})) . \quad (2.11)$$

The Rabi frequency of $\Omega_R/2\pi = 32.2 \pm 0.1$ kHz is slightly larger than for the measurement presented in Section 1.6.4 which is due to the fact that the position of our microwave antenna was readjusted between the two measurements. The maximum detected population in state $|1\rangle$ is equal to $P_{\max} = 93 \pm 2$ % and again includes all experimental imperfections. With $P_{\min} = 0.4^{+1.0}_{-0.4}$ %, the contrast is excellent:

$$C = \frac{P_{\max} - P_{\min}}{P_{\max} + P_{\min}} = 99.1^{+0.9}_{-3.7} \% . \quad (2.12)$$

We hereby demonstrate reliable single qubit rotations on our quantum register. The operation time of the Hadamard gate is equal to $\tau = \pi/(2\Omega_R) = 8 \mu\text{s}$. Note, however, that such a fast gate operation time comes at the cost of a lower Fourier-limited addressing resolution. For a reasonable addressing resolution of $\sigma_{\text{add}} = 10 \mu\text{m}$, the gate operation time increases to $\tau = 19 \mu\text{s}$, according to Table 2.2.

2.3.5 Multi-atom addressing

In the demonstrated register operations so far, only one individual atom was addressed. For the implementation of a scalable register, any number of atoms must be selectively manipulated once or several times. After characterizing the performance of our quantum register in the previous sections, I will here, giving two examples, illustrate the addressing of multiple atoms and discuss the current limitations.

Addressing of two individual atom qubits

In the first example, we perform a spin flip operation of two atoms on a five-qubit quantum register to prepare the register state $|01010\rangle$. For this purpose, we trap five atoms in our dipole trap. Again, one arm of the trap is switched off for 1 ms in order to increase the spatial distribution of the atoms sufficiently to resolve all individual atoms. We then take a picture (Figure 2.12 (I.a)) of the atom string to determine the resonance frequencies of atoms 2 and 4. This time, the microwave synthesizer is programmed in stepped sweep mode (see Section 1.6.2), with the start and stop frequencies equal to the frequencies of atom 2 and 4, respectively. Now the register is initialized in state $|00000\rangle$ (Figure 2.12 (I.b)). A Gaussian microwave π pulse with a pulse length of $2\sigma_\tau = 35.4 \mu\text{s}$ and a corresponding addressing resolution of $\sigma_{\text{add}} = 5 \mu\text{m}$ as shown in Figure 2.8 (b), flips the spin of atom 2 (Figure 2.12 (I.c)). Then the synthesizer frequency is stepped to the stop frequency within a settling time of 10 ms. Whenever its frequency is changed, the synthesizer needs to perform a levelling pulse for 1 ms to calibrate its output power. In order not to disturb atom 4, which is resonant with the new microwave frequency, we use the PIN-diode attenuator before the microwave amplifier which is able to attenuate this pulse by 60 dB at 9.2 GHz. After performing the levelling pulse we switch the attenuator to full transmission and apply a π pulse to flip the spin of atom 4. The register is now prepared in its final state $|01010\rangle$ (Figure 2.12 (I.d)). For state detection, we apply the push-out laser, which removes atoms 1,3, and 5 (Figure 2.12 (I.e)). A final image indeed reveals the presence of atoms 2 and 4 (Figure 2.12 (I.f)).

Currently, the maximum number of addressable qubits is, for technical reasons, limited to two. All coherent qubit manipulations are performed in a dipole trap lowered to a depth of 100 μK using the AOMs. Thermal drifts of the AOMs cause the dipole trap beams to misalign unless the trap depth is increased to the standard value of 0.8 mK after 50 ms. Therefore, all microwave pulses have to be applied within this time frame. Since it takes 70 ms to program the microwave synthesizer, it has to be set to the respective atom frequency before the dipole trap is lowered. The stepped sweep mode allows us to transmit two individual frequencies to the synthesizer at the same time and to switch

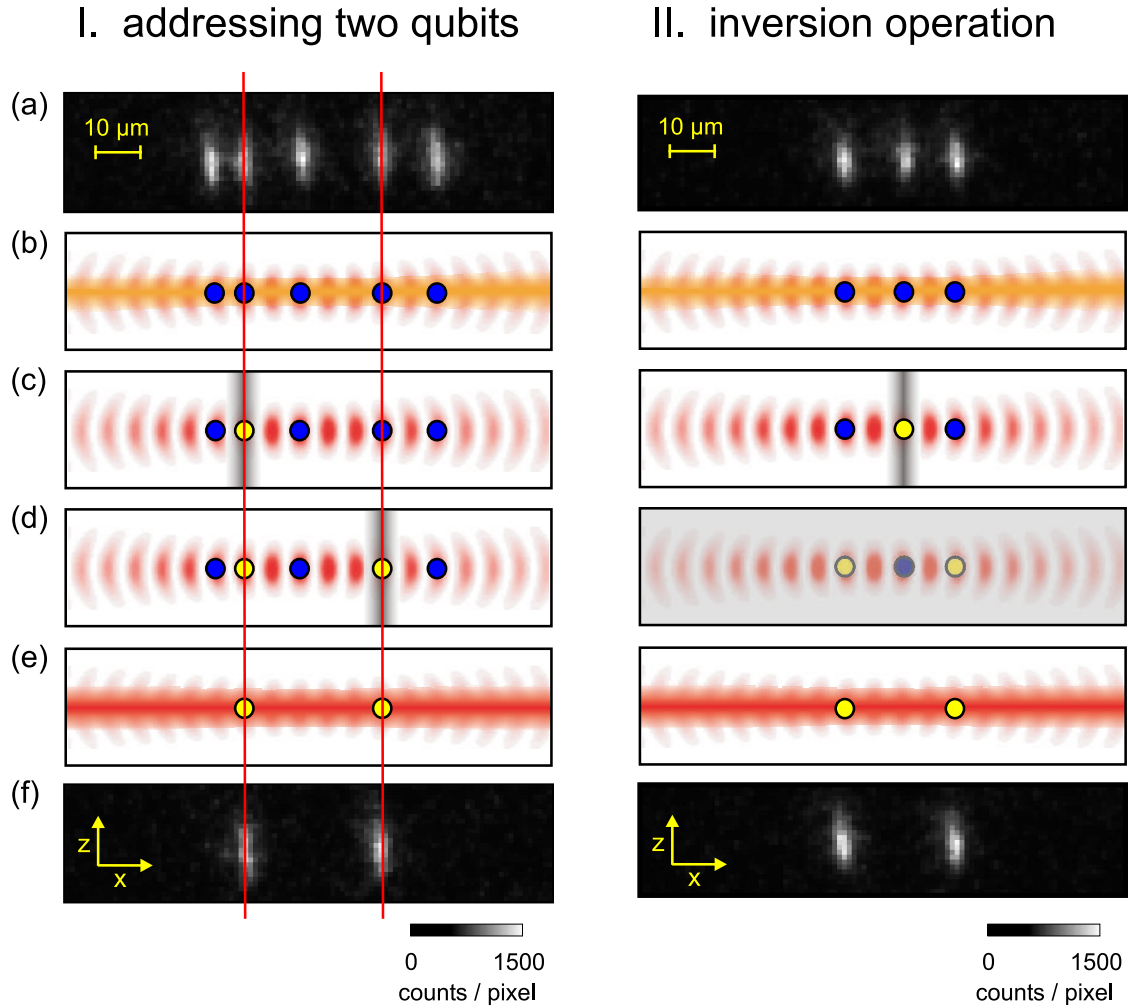


Figure 2.12: Two schemes for manipulating more than one atom of the quantum register. I. Preparation of the state $|01010\rangle$ by addressing two atoms. (a) Image of a five-atom quantum register. (b) Initialization in $|00000\rangle$ by optical pumping. (c) Application of a π pulse at the resonance frequency of atom 2. (d) Application of a π pulse at the resonance frequency of atom 4. (e) The state-selective push-out laser removes all atoms in state $|0\rangle$. (f) A final image reveals the presence of the remaining atoms in the trap. II. Inversion of the quantum register. (a) Image of three atoms. (b) Initialization in state $|000\rangle$. (c) Application of a π pulse to flip the spin of atom 2. (d) The application of a π pulse at the resonance frequency in the homogeneous guiding field B_0 performs an inversion operation of the entire quantum register. (e) and (f) as above.

between these frequencies within 10 ms via a trigger pulse. This technical limitation could easily be overcome by replacing the microwave synthesizer or by controlling the dipole trap power via an electro-optical modulator which does not show the undesired thermal drifts.

Inversion operation of the quantum register

In the second example, we perform a spin flip on an individual atom in combination with an inversion operation on the entire quantum register. Here, we trap three atoms in the dipole trap (Figure 2.12 (II.a)). The microwave synthesizer is programmed in stepped sweep mode as above, with the start frequency corresponding to the resonance frequency of atom 2, and the stop frequency being equal to the qubit resonance frequency in the homogeneous magnetic guiding field B_0 . We initialize the three atom register in $|000\rangle$ (Figure 2.12 (II.b)) and perform a spin flip on the second atom (Figure 2.12 (II.c)), similar to Section 2.3.1. Now, we switch off the magnetic field gradient, $B' = 0$, and wait for 40 ms to let eddy currents decay. The microwave synthesizer is triggered to switch to the stop frequency. Now we apply a square π pulse with a duration of $t_{\text{pulse}} = 19 \mu\text{s}$ which inverts the entire register from state $|010\rangle$ to state $|101\rangle$ (Figure 2.12 (II.d)). Application of the state-selective push-out laser removes the center atom (Figure 2.12 (II.e)) while atoms 1 and 3 remain trapped as shown in a final image (Figure 2.12 (II.f)).

2.3.6 Scalability

In the current stage, our quantum register should easily allow us to work with up to ten qubits. However, in order to scale its size to a larger number of qubits, it is necessary to implement several technical improvements.

Since the positions of the individual atom qubits are random, the probability that all atoms be sufficiently separated to be optically resolved, decreases with increasing qubit numbers. To circumvent this statistical limitation, it would be advantageous if the qubits could be evenly spaced. The size of the quantum register would then be limited by the minimum separation to optically resolve two neighboring atoms, which is currently $3 \mu\text{m}$. With the qubits populating every sixth trapping site, several hundred optically resolved qubits could be trapped within the trapping region which is given by the Rayleigh range of the trapping laser beams of currently $z_0 = 800 \mu\text{m}$. We are currently setting up a second conveyor belt, perpendicular to the existing one (see Section 3.2). This should allow us to place each atom of the quantum register into a desired potential well and would distribute the atoms evenly in the trapping region.

Once such a large neutral atom quantum register can be handled experimentally, the implementation of other trap geometries to increase the trapping region could push the qubit numbers even higher. An easy way would be to increase the laser power or the Rayleigh range of the trapping laser. A more difficult option would be the use of a standing wave trap made of Bessel beams which have the property to diverge more slowly than Gaussian beams. This would ensure homogeneous trap properties over a larger region.

With increasing register size, the requirement of selective manipulation of all qubits becomes increasingly difficult to fulfil. Therefore, the addressing speed should be increased such that the microwave frequencies can be switched from one qubit to another one within a few microseconds. Additionally, it would be desirable to perform several single qubit gates in parallel rather than the current serial procedure. For this purpose, several mi-

crowave signals at the respective qubit frequencies could be applied at the quantum register simultaneously.

Most importantly, all computations including read and write operations of the quantum register and two-qubit gate operations, which have yet to be implemented (see Section 3.1), must be performed within the coherence time of the quantum register. Its current coherence time of 600 μs (see Section 2.4) must be increased to make a larger quantum register feasible.

2.4 Coherence properties

A quantum register stores quantum states including superposition states. However, superposition states are very fragile because coupling to the environment causes dephasing, i. e. the loss of the known phase relationship between the quantum states of the qubits and the microwave field. Their resulting evolution from pure quantum states to a statistical mixture of states is called decoherence and sets the upper limit as to how long quantum information can be stored and processed.

2.4.1 Crosstalk

Our addressing technique of the quantum register requires a magnetic field gradient so that two qubits with a separation of Δx will inevitably acquire a phase of $\Delta\varphi(t) = \Delta x \omega' t$ between the states $|0\rangle$ and $|1\rangle$ within a time t . Since this phase difference is known and can be accounted for in possible gate operations, it does not cause decoherence of the quantum register.

A second effect changes the phase relation between the register qubits in a known and predictable way. The application of a microwave pulse at the resonance frequency of one qubit induces a coherent phase shift $\Delta\varphi$ on adjacent atoms. It is caused by non-resonant interaction with the detuned microwave pulse and is not negligible even if the separation of the qubits is large enough to prevent measurable population transfer. In the far-off resonant limit $\delta \gg \Omega_{\text{R}}$, the phase shift can be approximated [51]:

$$\Delta\varphi = \int_{-\infty}^{\infty} \frac{\Omega_{\text{R}}(t)^2}{2\delta} dt. \quad (2.13)$$

If a microwave π pulse with the Gaussian pulse shape $\Omega_{\text{R}}(t)$ of Equation (2.5), is applied with a detuning of $\delta = \omega' \Delta x$, Equation (2.13) yields:

$$\Delta\varphi = \frac{\pi^{\frac{3}{2}}}{4\sigma_{\tau}\delta}. \quad (2.14)$$

The general case requires the numerical integration of the optical Bloch equations (1.18). Figure 2.13 (b) shows the resulting phase shift as a function of the position offset for the addressing spectrum of Figure 2.8 (c). For illustration and comparison, the addressing spectrum is presented again in Figure 2.13 (a), where the solid line indicates the calculated

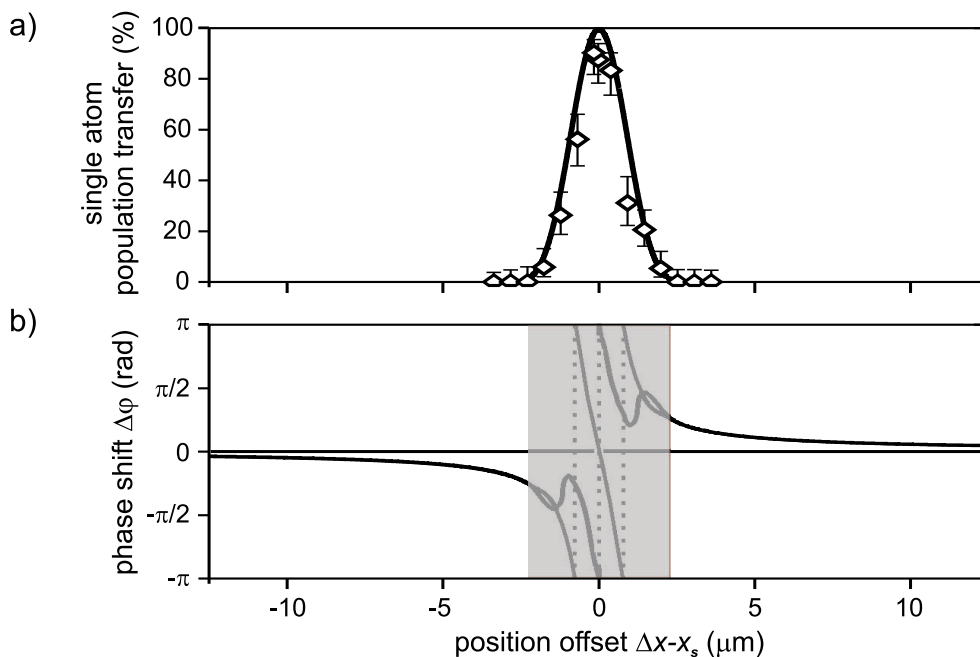


Figure 2.13: Coherent phase shift induced by non-resonant interaction with a microwave pulse. a) Single atom addressing spectrum of Figure 2.8 (c). The solid line shows the population transfer calculated from a numerical integration of the optical Bloch equations. b) Coherent phase shift inferred from the same calculation, for the two initial conditions $\mathbf{u}_0 = (0, 1, 0)$ and $\mathbf{u}_0 = (1, 0, 0)$. In the shaded area the phase shift between states $|0\rangle$ and $|1\rangle$ cannot be properly defined because significant population transfer occurs. At a position offset corresponding to the addressing resolution of $2.5 \mu\text{m}$, the phase shift is $\Delta\varphi = 0.2\pi$.

population transfer.

The phase shift plotted in Figure 2.13 (b) is inferred from the same calculation, with Bloch vectors initialized in state $\mathbf{u}_0 = (0, 1, 0)$ and $\mathbf{u}_0 = (1, 0, 0)$. In the shaded area around the atomic resonance, the phase cannot be properly defined because significant population transfer occurs. For large detuning, the phase shift is independent of the initial state \mathbf{u}_0 and exhibits the $1/\delta$ -relation of Equation (2.14). A second atom separated by the addressing resolution of $\sigma_{\text{add}} = 2.5 \mu\text{m}$ from the addressed atom acquires a phase shift of $\Delta\varphi = 0.2 \cdot \pi$, independent of \mathbf{u}_0 .

Since this coherent phase shift is known, it can be taken into account in future gate operations. If desired, it could also be reversed for this specific qubit by an appropriate microwave pulse with opposite detuning.

2.4.2 Optical Bloch equations with damping

Our following investigations show that the relevant timescales for the decoherence of our quantum register are set by dephasing mechanisms which cause the register qubits to lose

their known phase relation. For a formal description of spin relaxation and dephasing within the Bloch vector model, damping terms are added to the optical Bloch equations for an ensemble of atoms [51]:

$$\begin{aligned}\langle \dot{u} \rangle &= \delta \langle v \rangle - \frac{\langle u \rangle}{T_2} \\ \langle \dot{v} \rangle &= -\delta \langle u \rangle + \Omega_R \langle w \rangle - \frac{\langle v \rangle}{T_2} \\ \langle \dot{w} \rangle &= -\Omega_R \langle v \rangle - \frac{\langle w \rangle - w_{\text{st}}}{T_1},\end{aligned}\tag{2.15}$$

where $\langle \dots \rangle$ denotes the ensemble average. The population w decays to a stationary value w_{st} at the rate T_1 , which is called longitudinal relaxation time. The transverse dephasing time T_2 can be divided into two different contributions:

$$\frac{1}{T_2} = \frac{1}{T_2'} + \frac{1}{T_2^*}.\tag{2.16}$$

The homogeneous decay time T_2' governs the dephasing due to incoherent interactions that affect all atoms in the same way. The inhomogeneous dephasing time T_2^* measures the transverse lifetime due to inhomogeneous effects which assign each atom its own individual resonance frequency and cause macroscopic polarization damping of the ensemble. We will see in the following sections that there is an essential difference between these two types of dephasing. While inhomogeneous dephasing is usually reversible by spin echo pulses, homogeneous dephasing, e. g. due to random magnetic field fluctuations, cannot be reversed.

2.4.3 Ramsey spectroscopy in a magnetic guiding field

In previous experiments we have extensively studied the dephasing mechanisms of the magnetically insensitive $|F = 4, m_F = 0\rangle \leftrightarrow |F = 3, m_F = 0\rangle$ transition of the cesium atoms in our dipole trap [48]. However, the addressing scheme of the quantum register presented in this thesis requires the use of magnetically sensitive Zeeman states in a magnetic field. Not surprisingly, the greater sensitivity of the qubits to their environment shortens the dephasing times. For a detailed analysis of the limiting effects I first consider the dephasing mechanisms of the atoms in a homogeneous guiding field B_0 before studying the coherence properties of the quantum register in the inhomogeneous magnetic quadrupole field.

Ramsey spectroscopy, which was introduced in the context of magnetic resonance experiments [77, 78], is the standard technique to study dephasing mechanisms. It measures the total transverse dephasing time T_2 by free induction decay [79]. In the Bloch vector picture, an atom prepared in state $\mathbf{u}_0 = (0, 0, -1)$ is transferred to the uv plane by a $\pi/2$ pulse whose frequency ω is slightly detuned with respect to the atomic frequency ω_0 , see Figure 2.14. After free precession at the frequency $\delta = \omega - \omega_0$ during the time τ_R a second $\pi/2$ pulse rotates the Bloch vector around the u axis. A projection measurement onto the w axis reveals fringes at the frequency δ . The frequency spread of an

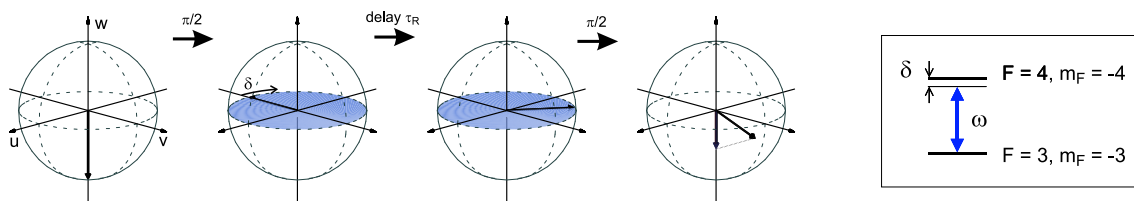


Figure 2.14: Ramsey spectroscopy. A $\pi/2$ pulse with a frequency detuning δ from the atomic resonance rotates the Bloch vector from $w = -1$ into the uv plane. After a delay time τ_R of free precession at the frequency δ , the phase of the Bloch vector is measured by application of a second $\pi/2$ pulse and subsequent projection measurement onto the w axis.

atomic ensemble $\Delta\omega_0$ causes the Ramsey fringes to decay within $T_2^* \approx 1/\Delta\omega_0$. We will see that $T_2^* \ll T_2'$ so that the total transverse dephasing time is governed by inhomogeneous dephasing mechanisms, $T_2 \approx T_2^*$.

Experimental parameters

The experimental sequence and the chosen parameters for this measurement are similar to the recording of Rabi oscillations, see Section 1.6.4. Here, instead of varying the duration of the microwave pulse, we record the final population in state $|1\rangle$ as a function of the delay τ_R in between two $\pi/2$ pulses of $t_{\pi/2} = 8 \mu\text{s}$ duration. The microwave frequency is chosen to be off-resonant by $\delta/2\pi = 10 \text{ kHz}$ which is small enough compared to the Rabi frequency of $\Omega_R/2\pi = 30 \text{ kHz}$ to reasonably remain in the limit of resonant pulses. The applied magnetic guiding field is $B_0 = 2 \text{ G}$ and the trap depth is $100 \mu\text{K}$. The resulting data are plotted in Figure 2.15.

Results – Inhomogeneous dephasing

The timescale for the decay of the Ramsey fringes in Figure 2.15 of roughly $300 \mu\text{s}$ is noticeably shorter than the dephasing time of 4.4 ms which was obtained for the magnetically insensitive transition studied in the thesis of Stefan Kuhr [48]. There, the dominating dephasing mechanism was identified to be the inhomogeneous broadening of the atomic resonance frequency due to the energy dependent differential light shift of the individual trapped atoms, see also Section 1.7.3. I will show in the following that the observed dephasing in Figure 2.15 is caused by the same mechanism. As the vectorial contribution to the light shift of the outer Zeeman transition is much larger than the scalar contribution (see Section 2.3.2), the dephasing times are correspondingly shorter. I therefore adopt the model developed in the thesis of Stefan Kuhr [48] for our case.

Note, however, that this model is a simplified classical model, in which the atomic motion in the trap is neglected. We recently learned that a full quantum mechanical treatment is required, as done in Reference [80], in order to fully account for the observed dephasing. A first estimate shows that the additional quantum mechanical effects are of the same order of magnitude as the classical dephasing effects considered below [81]. We believe,

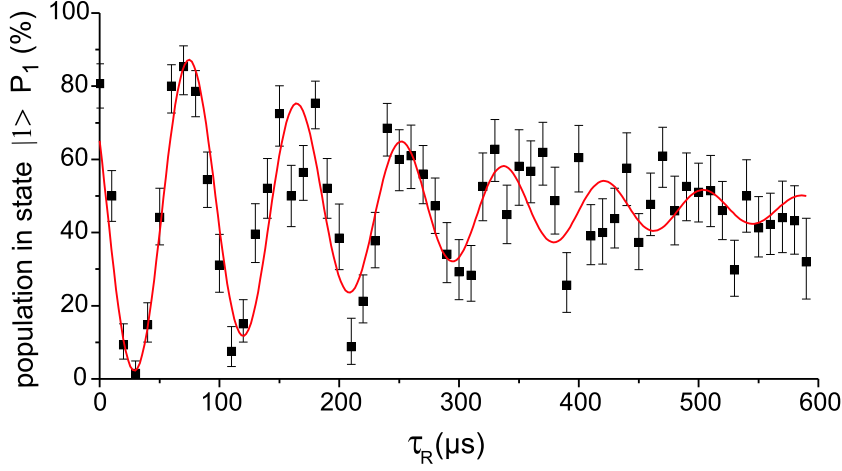


Figure 2.15: Decay of Ramsey fringes due to inhomogeneous broadening of the atomic resonance frequency. The data points show the measured population in state $|1\rangle$ as a function of the time delay τ_R between the two $\pi/2$ pulses. Every data point is averaged over 10 experimental runs with about 5 atoms each. The fit according to Equation (2.21) reveals an inhomogeneous dephasing time of $T_2^* = 270 \pm 25 \mu\text{s}$.

though, that these quantum effects are completely reversible and do not affect the spin echo analysis presented in Section 2.4.5. The full quantum mechanical treatment of the dephasing mechanisms in our trap is subject to future investigations.

In the classical model, the distribution of the differential light shifts of the trapped atoms is derived from their Boltzmann energy distribution. The shape of the Ramsey fringes $w_{\text{inh}}(\tau_R)$ is the Fourier-Cosine transform of this light shift distribution [72], see Equation (1.34):

$$w_{\text{inh}}(\tau_R) = \alpha(\tau_R, T_2^*) \cos[\delta\tau_R + \kappa(\tau_R, T_2^*)], \quad (2.17)$$

with a time-dependent amplitude $\alpha(\tau_R, T_2^*)$ and phase shift $\kappa(\tau_R, T_2^*)$:

$$\alpha(\tau_R, T_2^*) = \left(1 + 0.95 \left(\frac{\tau_R}{T_2^*}\right)^2\right)^{-3/2} \quad \text{and} \quad \kappa(\tau_R, T_2^*) = -3 \arctan\left(0.97 \frac{\tau_R}{T_2^*}\right). \quad (2.18)$$

The inhomogeneous dephasing time T_2^* is defined as the $1/e$ -time of the amplitude $\alpha(\tau_R, T_2^*)$:

$$\alpha(T_2^*) \stackrel{!}{=} e^{-1} \quad \Rightarrow \quad T_2^* = \sqrt{e^{2/3} - 1} \beta = 0.97\beta, \quad (2.19)$$

with the temperature-dependent coefficient

$$\beta = \frac{2U_0}{k_B T \delta_{\text{ls,max}}}. \quad (2.20)$$

Again, $\delta_{\text{ls,max}}$ denotes the maximum differential light shift for an atom in the bottom of the potential well. These relations hold as long as the atoms are cold enough to be in the

harmonic region of the trap.

The data in Figure 2.15 are therefore fitted using the following function which is obtained from Equations (2.17) and (2.19):

$$P_1(\tau_R) = A \cdot \alpha(\tau_R, T_2^*) \cos[\delta\tau_R + \kappa(\tau_R, T_2^*) + \varphi] + B. \quad (2.21)$$

In addition to the amplitude A and offset B , a phase φ is introduced because the Bloch vector also precesses during the application of the two $\pi/2$ pulses while the model only considers free precession during the time τ_R . The resulting fit parameters are listed in Table 2.4.

Fit results		
fringe amplitude	A	$45.1 \pm 2.1 \%$
fringe offset	B	$46.6 \pm 1.0 \%$
detuning	$\delta/2\pi$	$12.5 \pm 0.1 \text{ kHz}$
phase offset	φ	$1.15 \pm 0.08 \text{ rad}$
dephasing time	T_2^*	$270 \pm 25 \mu\text{s}$

Table 2.4: Fit results for the Ramsey fringes of Figure 2.15.

From temperature measurements in the dipole trap we know that in a trap of depth $U_0 = 0.1 \text{ mK}$ the temperature of the atoms is $T = 22 \pm 6 \mu\text{K}$ [54]. Equations (2.19) and (2.20) therefore allow us to infer the differential light shift $\delta_{\text{ls,max}}/2\pi = 5.2 \pm 1.4 \text{ kHz}$ from the measured dephasing time T_2^* . This result is smaller than the spectroscopically measured differential light of $|\Delta E_{\text{diff,tot}}/h| = 8.5 \pm 0.5 \text{ kHz}$ for $U_0 = 0.1 \text{ mK}$ presented in Section 2.3.2. This indicates that the actual trap depth for this measurement might have been smaller than assumed, for example due to slight misalignment of the trapping laser beams.

The measured detuning is slightly larger than the actually applied detuning of $\delta = 10 \text{ kHz}$. This is probably due to the fact that the Ramsey fringes were not acquired immediately after the spectroscopic calibration of the atomic resonance frequency ω_0 . The drifts of the atomic resonance frequency of 1 kHz/h increased the detuning between the two measurements.

The measured phase offset φ due to the Bloch vector precession during the two $\pi/2$ pulses roughly confirms the pulse duration $t_{\pi/2} = \varphi/2\delta = 7.3 \pm 0.5 \mu\text{s}$.

2.4.4 Spin echo spectroscopy in a magnetic guiding field

Inhomogeneous dephasing can be reversed by applying a π pulse between the two $\pi/2$ pulses. The Bloch vectors dephase due to the slightly different precession frequencies of different atoms. If the π pulse is applied at the time τ_π after the first $\pi/2$ pulse, they will rephase at $2\tau_\pi$, see Figure 2.16. This phenomenon is referred to as a spin echo and was first implemented in magnetic resonance experiments [82]. Nowadays, this technique

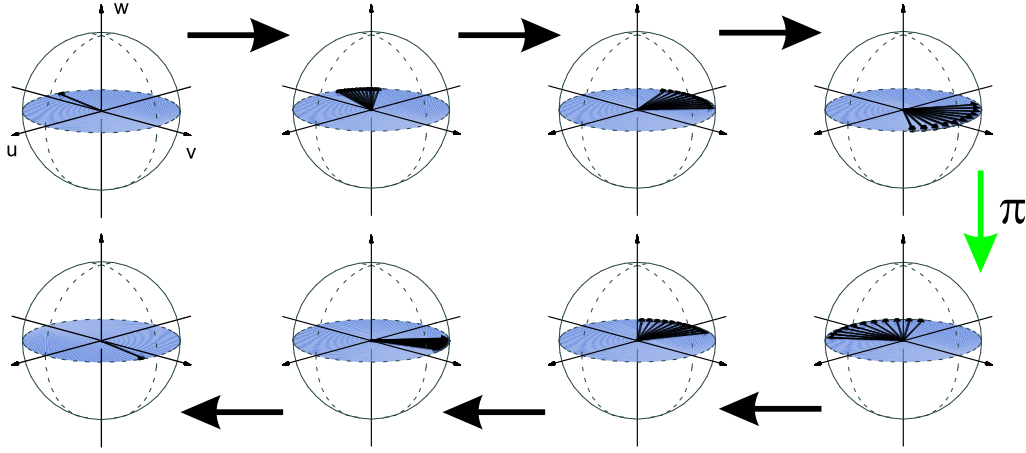


Figure 2.16: Spin echo. The dephasing Bloch vectors are rephased by the application of a π pulse between the two Ramsey $\pi/2$ pulses.

has also been applied to atoms captured in dipole traps [17, 83].

To measure the homogeneous transverse dephasing time T_2' of the trapped atoms in the magnetic offset field B_0 we performed spin echo spectroscopy for various times τ_π . As the contrast of the spin echo fringes decreases with increasing τ_π we infer T_2' from their envelope.

Experimental parameters

The experimental parameters are identical to the ones used in the previous section. The spin echos are recorded in a trap of depth $U_0 = 100 \mu\text{K}$, in a magnetic guiding field of 2 G, and with a microwave detuning of $\delta/2\pi = 10 \text{ kHz}$.

Results

The recorded spin echo signals are shown in Figure 2.17 (a). Each spin echo signal belongs to a separate measurement with fixed τ_π . While the Ramsey fringes of Figure 2.15 decay within $T_2^* = 270 \mu\text{s}$, the spin echo contrast decreases on a longer timescale.

The shape of the spin echo signals is very similar to the Ramsey signal [17]. However, for simplicity, I have neglected T_2^* in Equation (2.21) to yield the following fit function:

$$P_1(t) = -A \cdot \cos[\delta(t - 2\tau_\pi) + \phi] + B. \quad (2.22)$$

Here, the phase shift ϕ accounts for slow systematic phase drifts during the spin echo sequence. The contrast is defined by:

$$C = \frac{P_{\max} - P_{\min}}{P_{\max} + P_{\min}} = \frac{A}{B}. \quad (2.23)$$

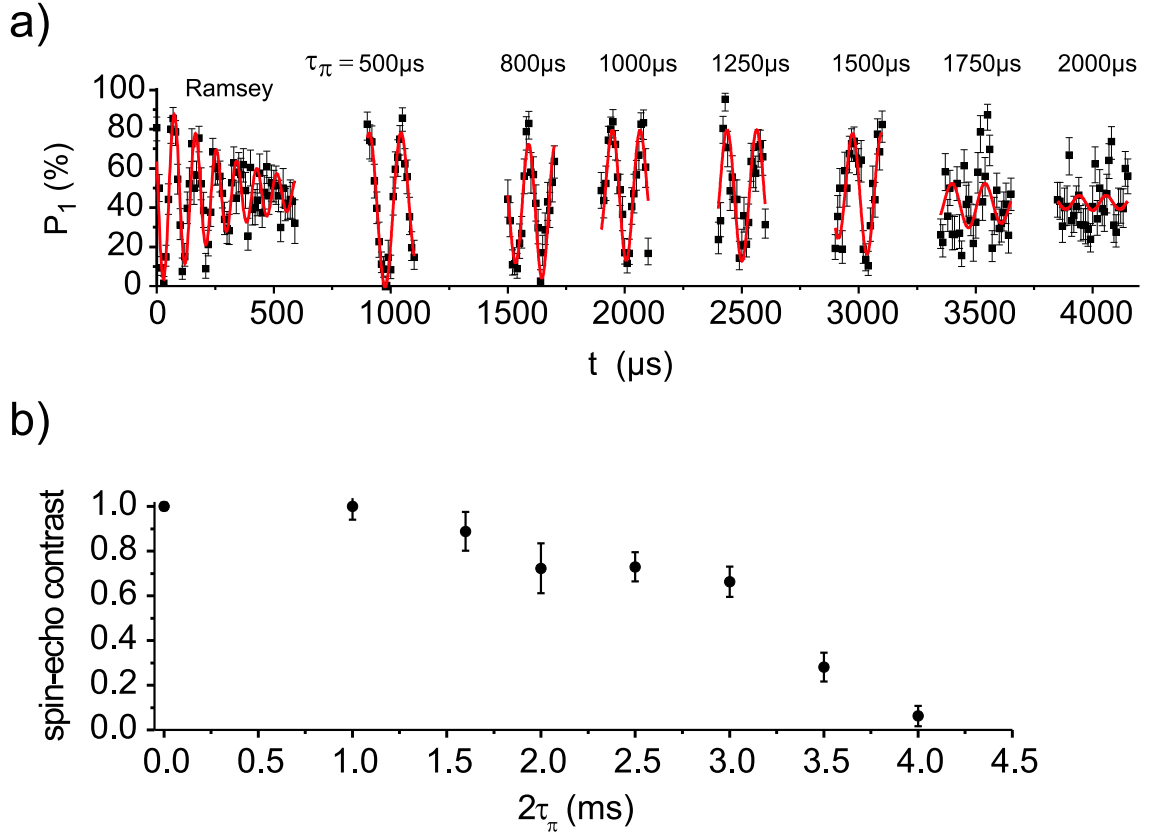


Figure 2.17: (a) Spin echo fringes in a magnetic guiding field. While the Ramsey signal decays quickly, the spin echo contrast decreases on a longer timescale. Every data point is obtained from 5 experimental runs with about 9 atoms each. The lines are fits according to Equation (2.22). (b) The spin echo contrast as a function of spin echo time $2\tau_\pi$ reveals a homogeneous dephasing time of $T_2' \approx 3.5$ ms.

The result is shown in Figure 2.17 (b) where I plotted the contrast as a function of the spin echo time $2\tau_\pi$. In analogy to T_2^* , we define the homogeneous dephasing time T_2' as the $1/e$ -time of the contrast:

$$C(2\tau_\pi = T_2') \stackrel{!}{=} C(0)e^{-1}. \quad (2.24)$$

From the data points I estimate a homogeneous dephasing time of $T_2' \approx 3.5$ ms.

2.4.5 Dephasing mechanisms in a magnetic guiding field

In the following I discuss the mechanisms that lead to the observed dephasing. So far, the detuning δ has been treated as time independent resulting in a rephasing of the precessing Bloch vectors at exactly $2\tau_\pi$. However, a time-varying detuning $\delta(t)$ results in a shift of the spin echo signal if the difference of the accumulated phases $\Delta\phi(\tau_\pi)$ before and after

the rephasing π pulse does not vanish:

$$\Delta\phi(\tau_\pi) = \int_{\tau_\pi}^{2\tau_\pi} \delta(t') dt' - \int_0^{\tau_\pi} \delta(t') dt'. \quad (2.25)$$

The time dependence of $\delta(t)$ is caused by, e. g., magnetic field and intensity fluctuations. Since the acquisition of a spin echo signal requires several repetitions of the experimental sequence, $\Delta\phi(\tau_\pi)$ will be different every time resulting in a decrease of the fringe contrast.

We express the phase difference (2.25) as an average detuning difference $\Delta\delta = \Delta\phi(\tau_\pi)/\tau_\pi$ and assume its probability distribution to be Gaussian:

$$p(\Delta\delta, \tau_\pi) = \frac{1}{\sigma_{\Delta\delta}(\tau_\pi)\sqrt{2\pi}} \exp\left(-\frac{(\Delta\delta)^2}{2\sigma_{\Delta\delta}(\tau_\pi)^2}\right), \quad (2.26)$$

with mean $\overline{\Delta\delta} = 0$ and variance $\sigma_{\Delta\delta}(\tau)^2$. The decay of the spin echo contrast $C(\tau_\pi)$ is given by an integral similar to the Fourier-Cosine transform of the distribution of fluctuations $p(\Delta\delta, \tau_\pi)$ [48]:

$$C(\tau_\pi) = C_0 \int_{-\infty}^{\infty} -\cos(\Delta\delta \tau_\pi) p(\Delta\delta, \tau_\pi) d\Delta\delta. \quad (2.27)$$

Performing the integration yields:

$$C(\tau_\pi) = C_0 \exp\left(-\frac{1}{2} \tau_\pi^2 \sigma_{\Delta\delta}(\tau_\pi)^2\right). \quad (2.28)$$

Magnetic field fluctuations

The observed homogeneous dephasing is most likely caused by magnetic field fluctuations of the guiding field. At the time when we recorded the Ramsey and spin echo measurements presented so far, we only possessed a noisier current supply (Elektro-Automatik, EA-PS 3016-10) to provide the guiding field along the trap axis. Since its relative current stability of $I_{\text{rms}}/I_0 = 10^{-3}$ was insufficient to measure spin echo fringes, we used a low-pass filter with a time-constant of 10 ms to increase the magnetic field stability in the frequency range above 100 Hz. This improvement allowed us to measure the spin echo fringes presented in Figure 2.17. According to Equations (2.24) and (2.28) the decay of the contrast yields a standard deviation for the average detuning difference of $\sigma_{\Delta\delta}(T_2') = 2\pi \cdot 130$ Hz, see Table 2.5.

The minimum relative current stability inferred from this result is therefore:

$$\frac{I_{\text{rms}}}{I_0} = \frac{B_{\text{rms}}}{B_0} = \frac{\sigma_{\Delta\delta}(T_2')}{\delta_0} = 2.5 \cdot 10^{-5}. \quad (2.29)$$

Fluctuations of the magnetic field caused by other devices in the vicinity of the atom trap remain to be investigated. Since the measured dephasing time already demonstrates that the magnetic field fluctuations are smaller than $B_{\text{rms}} = 50 \mu\text{G}$, it might be sensible to use the high sensitivity of the qubit transition itself as a probe for measuring and improving the magnetic field stability.

Beam pointing instability of the dipole trap laser

In previous work [72] we investigated the pointing stability of the two dipole trap laser beams. The fluctuating optical contrast of the standing wave due to beam pointing instabilities was identified as the dominant mechanism for the homogeneous dephasing time of $T_2' = 68$ ms of the magnetic field insensitive $|F = 3, m_F = 0\rangle \leftrightarrow |F = 4, m_F = 0\rangle$ transition.

The qubit transition investigated here is more sensitive to this effect due to non-vanishing contributions of circular light polarizations, see Section 2.3.2. Taking also into account the circular light shift, we expect a homogeneous dephasing time of $T_2' = 12$ ms.

Intensity fluctuations

Similarly to the beam pointing instabilities, intensity fluctuations of the dipole trap laser contribute to homogeneous dephasing. The resulting fluctuations of the trap depth cause fluctuations of the differential light shift and thus of the detuning between the microwave frequency and the atomic resonance frequency. Transferring the results from previous investigations [48] to the present case, the expected homogeneous dephasing time due to intensity fluctuations amounts to $T_2' = 23$ ms.

Further dephasing mechanisms

Other dephasing mechanisms such as elastic collisions, heating, and fluctuations of the microwave power and pulse duration have been investigated [48] and found to be several orders of magnitude weaker than the dominating dephasing effects discussed above.

An additional source of dephasing is the time-dependent differential light shift due to the oscillatory motion of the atoms in the trap. This effect is fully analyzed and discussed for the case of the modulation of the atomic resonance frequency in the magnetic field gradient

	Homogeneous dephasing time	Fluctuation amplitude
	T_2'	$\frac{\sigma_{\Delta\delta}(T_2')}{2\pi}$
measured	3.5 ms	130 Hz
Dephasing mechanisms		
magnetic field fluctuations	≥ 3.5 ms	≤ 130 Hz
beam pointing instability	12 ms	37 Hz
intensity fluctuations	23 ms	19 Hz

Table 2.5: Summary of the relevant irreversible dephasing mechanisms in a magnetic guiding field.

in Section 2.4.7. It causes a periodic decay and revival of the spin echo contrast at twice the radial oscillation frequency of the trapped atoms. For the value of the differential light shift $\delta_{\text{ls,max}}/2\pi = 8.5$ kHz in a trap of $U_0 = 100$ μK , as measured in Section 2.3.2, I would expect a periodic decay of the contrast by 22 %. However, since this effect is not observed in the measurement, I conclude that the differential light shift is $\delta_{\text{ls,max}}/2\pi = 5$ kHz as derived from the Ramsey fringes of Section 2.4.3 or even smaller. For these values, the periodic reduction of the contrast amounts to less than 10 %.

Finally, population relaxation of the two ground states, characterized by the decay time T_1 , which is caused by scattering of photons from the dipole trap laser, was also measured in our group [41]. In a trap of depth $U_0 = 100$ μK the resulting population decay time amounts to $T_1 = 86$ s and is completely negligible in this context.

I have summarized the measured and the expected homogenous dephasing times for the relevant dephasing mechanisms in Table 2.5, along with the fluctuation amplitude $\sigma_{\Delta\delta}$ at the respective time T_2' .

2.4.6 Spin echo spectroscopy in a magnetic field gradient

After analysis of the dephasing mechanisms of trapped atoms in a homogeneous magnetic guiding field, I now study the dephasing time in the inhomogeneous magnetic field gradient (2.1) because it determines the coherence time of the quantum register. Adding the quadrupole field to the guiding field gives rise to additional dephasing mechanisms. The coupling of external and internal degrees of freedom via the field gradient has the side effect that position fluctuations of the atoms translate into fluctuations of the qubit frequency. We will see in Section 2.4.7 that the radial oscillations of the atoms in the trap limit the coherence time of the quantum register. On a longer timescale, axial position fluctuations of the standing wave dipole trap constitute an additional dephasing mechanism.

A spin echo measurement of the quantum register is significantly more complicated and time consuming than the presented measurements in a magnetic guiding field, because it has to be performed on single atoms. After transfer from the MOT into the dipole trap, the atoms are distributed along the trap axis over at least 20 – 30 μm . At the gradient of $B' = -1.5$ mG/ μm , this corresponds to a frequency spread of up to 110 kHz which is much larger than the Rabi frequency. Ramsey or spin echo spectroscopy on such an atomic cloud will therefore fail. For this reason, we perform a spin echo measurement on single atoms only, combining our addressing technique presented in Section 2.3.1 with the spin echo technique demonstrated in Section 2.4.4.

Experimental sequence

A schematic overview of the experimental sequence is shown in Figure 2.18. We start by loading atoms into the MOT. The loading time has been optimized such that the average atom number is one. After transfer into the dipole trap we acquire an image of the atom and determine its position and resonance frequency. The magnetic gradient field $\mathbf{B}(\mathbf{r})$, see Equation (2.1), is switched on, with $B_0 = 4$ G and $B' = -1.5$ mG/ μm . After lowering

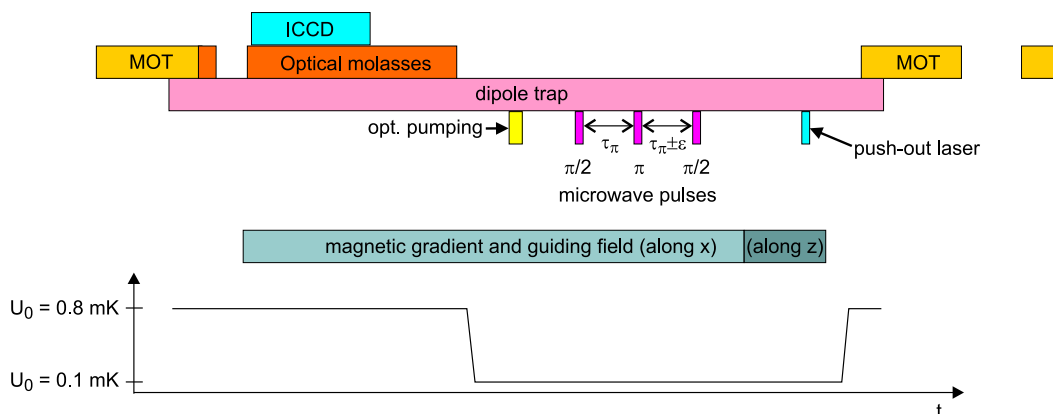


Figure 2.18: Experimental sequence for the spin echo measurement of the quantum register. After transfer from the MOT into the dipole trap, we image the atom with the ICCD. In the lowered trap, the atom is initialized by optical pumping and subjected to the resonant spin echo pulse sequence. State-selective detection is performed by application of the push-out laser and subsequent fluorescence detection in the MOT.

the trap depth to $100 \mu\text{K}$ and initializing the atom in state $|0\rangle$, we apply the first Ramsey $\pi/2$ pulse at $t = t_0$. For simplicity, the pulse shape is rectangular, with a pulse duration of $t_{\pi/2} = 8 \mu\text{s}$. The microwave frequency is tuned in resonance with the atomic frequency, $\delta = 0$, as discussed below. At $t = t_0 + \tau_{\pi}$, we apply the spin echo π pulse. Since complete rephasing is expected at $t = t_0 + 2\tau_{\pi}$, we then apply the final $\pi/2$ pulse and detect the state of the atom by subjecting it to the push-out laser and by subsequently transferring it into the MOT.

This sequence is repeated 100 times which takes a total acquisition time of five minutes. We post-select all experimental runs with exactly one atom present so that the resulting data point contains roughly 40 single atom events. The measurement of an entire spin echo signal as demonstrated in Section 2.4.4 is impossible due to the drifts of the atomic resonance frequency caused by the time-varying differential light shift over the long data acquisition time. We therefore infer the spin echo contrast by simply measuring the minimum P_{\min} of the spin echo signal. Since the resonant transfer efficiency including all experimental imperfections amounts to $100_{-5.1}^{+0.0} \%$, we set $P_{\max} = 1 - P_{\min}$. Thus, the contrast is equal to:

$$C = \frac{P_{\max} - P_{\min}}{P_{\max} + P_{\min}} = 1 - 2P_{\min}. \quad (2.30)$$

Although the spin echo minimum is expected at $t = t_0 + 2\tau_{\pi}$, homogeneous systematic frequency drifts lead to a small shift of this minimum. This effect was also observed in the spin echo signals recorded in the magnetic guiding field, see Figure 2.17, and was formally accounted for by an additional phase shift ϕ in Equation (2.22). In order to measure P_{\min} more precisely, we therefore acquire up to five data points around the minimum of the echo signal at $t = t_0 + 2\tau_{\pi} \pm \epsilon$, with ϵ being varied in steps of $30 \mu\text{s}$. In order to minimize the number of data points required to determine P_{\min} reasonably well, we apply

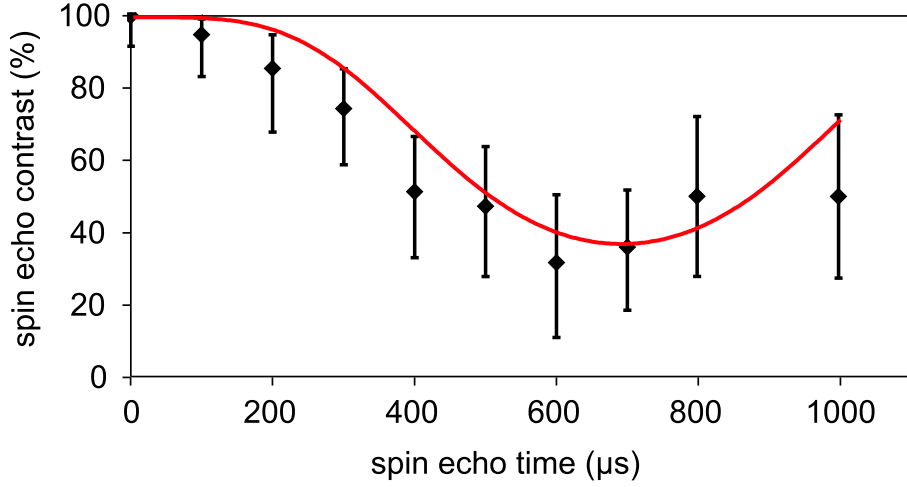


Figure 2.19: Spin echo contrast of the quantum register. Each data point is obtained from 40 single atom measurements of P_{\min} . The contrast is calculated according to Equation (2.30). The line is the result of the numerical calculation of Section 2.4.7 (Equation (2.42), Table 2.6).

a resonant pulse rather than a pulse which is detuned by $\delta/2\pi = 10$ kHz as done in the previous sections. In the resonant case, the spin echo signal $P_1(t)$ is the envelope of the spin echo fringes obtained for $\delta \neq 0$. Finding the minimum of this envelope requires less measurements than for the minimum of the spin echo fringes, which oscillate at the frequency δ .

The entire procedure described so far serves to measure the spin echo contrast for one fixed spin echo time $2\tau_\pi$ and takes roughly 30 min. Thus, the ten data points shown in Figure 2.19 require a total data acquisition time of five hours.

2.4.7 Dephasing mechanisms in a magnetic field gradient

While the contrast is larger than 80 % for a spin echo time of up to 200 μs , it drops to only 30 % on a timescale of 600 μs . In the following I analyze the underlying dephasing mechanisms.

Radial oscillations of the trapped atoms

The limiting dephasing mechanism of our quantum register are the radial oscillations of the trapped atoms which translate into oscillations of the qubit frequency via the magnetic field gradient. The following calculation shows that these periodic fluctuations can only partly be reversed by the spin echo pulse.

Let us first consider the modulus of the magnetic field (2.1):

$$|\mathbf{B}(\mathbf{r})| = \sqrt{(B_0 + B'x)^2 + B'^2(y^2 + 4z^2)}. \quad (2.31)$$

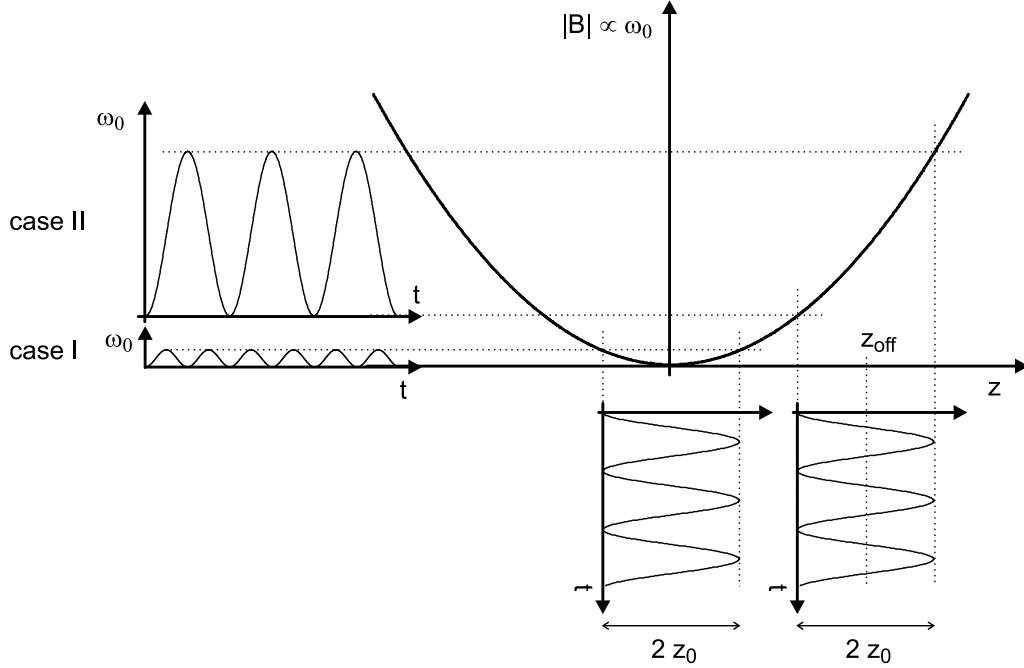


Figure 2.20: Modulation of the atomic resonance frequency ω_0 due to the radial oscillation (along z) of the atom in the dipole trap. If the trap is coaligned with the symmetry plane of the magnetic field ($z_{\text{off}} = 0$), the amplitude of the frequency modulation is small (case I). In the case of a misalignment ($z_{\text{off}} > z_0$), the modulation amplitude increases (case II) and the modulation occurs at half the frequency of case I.

Due to the large offset field B_0 along x , $(B_0 + B'x)^2 \gg B'^2(y^2 + 4z^2)$. A Taylor expansion of $|\mathbf{B}(\mathbf{r})|$ yields:

$$|\mathbf{B}(\mathbf{r})| \approx B_0 + B'x + \frac{B'^2}{2B_0}(y^2 + 4z^2). \quad (2.32)$$

While the modulus of the magnetic field is linear along the trap axis (x), it has a quadratic dependence in the y and z direction.

Let us now consider the radial oscillation (along the z direction) of an atom in the dipole trap, with oscillation frequency Ω_{rad} and amplitude z_0 . Since it is unlikely that the dipole trap is perfectly aligned along the symmetry plane of the magnetic field, we introduce a position offset z_{off} . The oscillation of the atom with an initial phase φ_0 then reads:

$$z(t) = z_{\text{off}} + z_0 \sin(\Omega_{\text{rad}}t + \varphi_0). \quad (2.33)$$

This oscillation results in a modulation of the atomic resonance frequency (see Figure 2.20)

according to Equation (2.32):

$$\begin{aligned}\omega_0(t) &= \frac{d\omega_0}{dB} |\mathbf{B}(\mathbf{r})| = \omega_0(x, y) + \zeta z^2(t), \\ \text{with } \zeta &= 2 \frac{d\omega_0}{dB} \frac{B'^2}{B_0} \\ \text{and } \frac{d\omega_0}{dB} &= \frac{(3g_3 - 4g_4)\mu_B}{\hbar} = 2\pi \cdot 2.45 \frac{\text{MHz}}{\text{G}}.\end{aligned}\quad (2.34)$$

The resulting difference of the accumulated phases $\Delta\phi(\tau_\pi, \varphi_0)$ before and after the spin echo pulse then reads:

$$\begin{aligned}\Delta\phi(\tau_\pi, \varphi_0) &= \int_{\tau_\pi}^{2\tau_\pi} \omega_0(t') dt' - \int_0^{\tau_\pi} \omega_0(t') dt' \\ &= \frac{1}{\Omega_{\text{rad}}} 8\zeta z_0 \cos(\Omega_{\text{rad}}\tau_\pi + \varphi_0) \sin^2\left(\frac{\Omega_{\text{rad}}\tau_\pi}{2}\right) \\ &\quad \times \left[z_{\text{off}} + z_0 \sin(\Omega_{\text{rad}}\tau_\pi + \varphi_0) \cos^2\left(\frac{\Omega_{\text{rad}}\tau_\pi}{2}\right) \right]\end{aligned}\quad (2.35)$$

In order to calculate the expected spin echo contrast following the lines of Section 2.4.5, we have to infer from Equation (2.35) the probability distribution of the average detuning difference $\Delta\delta(\tau_\pi) = \Delta\phi(\tau_\pi)/\tau_\pi$. For this purpose, we first calculate the corresponding probability distribution $p_E(\Delta\delta, \tau_\pi)$ for fixed atom energy E . Since $p_E(\Delta\delta)d\Delta\delta = p(\varphi_0)d\varphi_0$, we obtain:

$$p_E(\Delta\delta, \tau_\pi) = p(\varphi_0) \frac{d\varphi_0(\Delta\delta)}{d\Delta\delta}.\quad (2.36)$$

Here, $p(\varphi_0) = 1/(2\pi)$ is the homogeneous phase distribution. Since we have to compute the inverse function $\varphi_0(\Delta\delta)$, we consider two cases, see Fig. 2.20.

I) $z_{\text{off}} = 0$: We neglect the position offset in Equation (2.35) and thus assume perfect alignment of the dipole trap axis through the center of the magnetic field.

II) $z_{\text{off}} > z_0$: We assume that the misalignment is considerable so that the resulting position offset is generally larger than oscillation amplitude. In this case, we neglect the last term “ $z_0 \sin(\dots) \cos^2(\dots)$ ” of Equation (2.35).

Case II: $z_{\text{off}} > z_0$

Let us first consider case II as it turns out that it models the observed dephasing reasonably well. Computation of Equation (2.36) yields:

$$p_{E,\text{II}}(\Delta\delta, \tau_\pi) = \frac{1}{\pi \sqrt{\Delta\delta_0^2 - \Delta\delta^2}}, \quad |\Delta\delta| \leq \Delta\delta_0,\quad (2.37)$$

$$\text{with } \Delta\delta_0 = \frac{8\zeta z_0 z_{\text{off}}}{\Omega_{\text{rad}}\tau_\pi} \sin^2\left(\frac{\Omega_{\text{rad}}\tau_\pi}{2}\right)\quad (2.38)$$

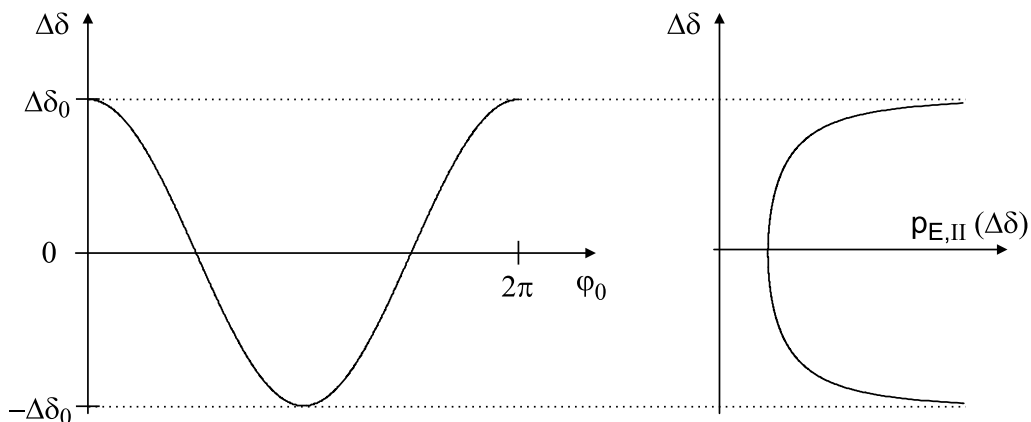


Figure 2.21: a) The average detuning difference $\Delta\delta$ is shown as a function of the initial phase φ_0 , according to Equation (2.35) and case II, see text. b) Corresponding probability distribution $p_{E,II}(\Delta\delta)$ according to Equation (2.37).

Both $\Delta\delta(\varphi_0)$ and its corresponding probability distribution $p_{E,II}(\Delta\delta)$ are shown in Figure 2.21.

The oscillation amplitude of the atom depends on its energy E . Restricting ourselves to the harmonic bottom of the potential well, so that $z_0^2 = 2E/m\Omega_{\text{rad}}^2$, we integrate $p_{E,II}(\Delta\delta, \tau_\pi)$ over the energy with the one-dimensional Maxwell-Boltzmann distribution

$$p_B(E) = \frac{1}{k_B T} \exp\left(-\frac{E}{k_B T}\right) \quad (2.39)$$

as a weighting factor. The resulting distribution $p_{II}(\Delta\delta, \tau_\pi)$ is Gaussian:

$$\begin{aligned} p_{II}(\Delta\delta, \tau_\pi) &= \int_0^\infty p_{E,II}(\Delta\delta, \tau_\pi) p_B(E) dE \\ &= \frac{1}{\sqrt{2\pi\sigma_{\Delta\delta}^2}} \exp\left(-\frac{\Delta\delta^2}{2\sigma_{\Delta\delta}^2}\right), \end{aligned} \quad (2.40)$$

with

$$\sigma_{\Delta\delta} = \sqrt{\frac{k_B T}{m}} \frac{8\zeta z_{\text{off}}}{\Omega_{\text{rad}}^2 \tau_\pi} \sin^2\left(\frac{\Omega_{\text{rad}} \tau_\pi}{2}\right). \quad (2.41)$$

We finally obtain the spin echo contrast by computing the integral of Equation (2.27):

$$C_{II}(\tau_\pi) = \exp\left(-\frac{\tau_\pi^2 \sigma_{\Delta\delta}^2}{2}\right). \quad (2.42)$$

Revivals of the spin echo contrast

Although the resulting contrast looks Gaussian, it is periodic in τ_π due to the periodicity of $\sigma_{\Delta\delta}$. Whether or not the spin echo pulse rephases the Bloch vectors therefore depends

on τ_π . If τ_π equals an integer multiple of the period of the frequency modulation $2\pi n/\Omega_{\text{rad}}$, perfect rephasing should be possible.

radial oscillation frequency	$\Omega_{\text{rad}}/2\pi$	1.45	kHz
lateral position offset	z_{off}	15	μm
atom temperature	T	50	μK

Table 2.6: Parameters of the contrast as inserted into Equations (2.41) and (2.42).

Assuming the parameters of Table 2.6, our model yields a contrast (solid line in Figure 2.19) which matches the measured data fairly well. Within the error bars the radial oscillation frequency Ω_{rad} corresponds to the frequency measured in Section 1.2, taking into account the lowered trap depth of $U_0 = 100 \mu\text{K}$. The assumed value for the lateral position offset z_{off} is taken from the observation that the MOT is usually displaced by $15 \mu\text{m}$ from the center of the magnetic quadrupole field along the x axis, which is measured as presented in Section 2.2. It seems possible that such a displacement is also present along the z axis, but we cannot directly measure it. Furthermore, we observed that the lateral misalignment of the dipole trap laser beams with respect to the MOT position can be as large as $10 \mu\text{m}$. The assumed atom temperature is rather high but still within the daily fluctuations of our experiment.

Although the magnetic field gradient in axial direction is much larger than in radial direction considered here, it does not significantly contribute to the observed dephasing because due to the high axial oscillation frequency, the phase difference $\Delta\phi(\tau_\pi, \varphi_0)$ of Equation (2.35) is always much smaller than 2π .

Since our model agrees well with the measured data it would be desirable to confirm the predicted revival of the spin echo contrast experimentally. Due to the considerable data acquisition time we have not yet pursued such a measurement. It seems to be more sensible to eliminate the observed dephasing mechanism before carrying out a second spin echo measurement with single atoms.

Similar revivals of the spin echo contrast have been observed in atom-optics billiards in the group of N. Davidson [80, 83]. In their system, dephasing is caused by the differential light shift induced by the near-resonant trapping lasers which form a “stadium” – an anharmonic dipole trap made by two laser beams which intersect at an angle. Partial revivals occur at timescales corresponding to the average collision time of the trapped atoms with the stadium walls, in analogy to the oscillation period in our trap.

Possible improvements

A possible way of decreasing the influence of the magnetic field gradient on the dephasing due to radial oscillations would be the alignment of the dipole trap axis along the z direction of the magnetic quadrupole field. The Taylor expansion of the magnetic field

modulus given in Equation (2.31) would then read:

$$|\mathbf{B}(\mathbf{r})| = B_0 + 2B'z + \frac{B'^2}{2B_0}(x^2 + y^2). \quad (2.43)$$

The quadratic dependence along the new radial direction (x, y) is thus reduced by a factor of four, cf. Equation (2.32). In addition, the gradient B' can be reduced by a factor of two to obtain the same gradient as before, which decreases the radial sensitivity by another factor of four. Thus, the lateral magnetic field dependence is reduced by a factor of 16. Further ways of increasing the coherence time of our quantum register include an increase of the magnetic guiding field B_0 and a reduction of the radial oscillation amplitude by further cooling of the atoms.

Case I: $z_{\text{off}} = 0$

Let us finally come back to case I of our model which considers oscillation of the atom about the symmetry plane of the magnetic field, with $z_{\text{off}} = 0$. Following the same calculations demonstrated above, it yields the contrast:

$$C_I(\tau_\pi) = \left[1 + \left(\frac{2\zeta k_B T \sin^2(\Omega_{\text{rad}}\tau_\pi)}{m\Omega_{\text{rad}}^3} \right)^2 \right]^{-\frac{1}{2}} \quad (2.44)$$

This function is also periodic, with half the period as $C_{II}(\tau_\pi)$. However, the reduction of the contrast amounts to less than 2 %. This effect does therefore not significantly contribute to the observed dephasing.

Axial position fluctuations of the dipole trap

There is a further dephasing mechanism which is peculiar to the magnetic field gradient. Optical phase fluctuations of the standing wave interference pattern translate into axial position fluctuations of the dipole trap. They cause a corresponding fluctuation of the atomic resonance frequency due to the linear magnetic field gradient along the trap axis.

In order to investigate this effect we interferometrically measure the optical phase fluctuations between the two trapping laser beams. The experimental setup is depicted in Figure 2.22 (a). The two trapping beams are overlapped on a beam splitter and focussed onto a photo diode. The two AOMs are set to slightly different frequencies causing the frequencies of the two beams to differ by 1.2 MHz. Using a lock-in amplifier, we thus measure the optical phase difference between the two trapping beams.

The resulting data traces show the optical phase difference between the two beams as a function of time. In order to receive a measure for the phase fluctuations in different frequency bands, we compute the Allan deviation defined as [84]:

$$\sigma_A(\tau) = \sqrt{\frac{1}{m} \sum_{k=1}^m \frac{(\bar{x}_{\tau,k+1} - \bar{x}_{\tau,k})^2}{2}}, \quad (2.45)$$

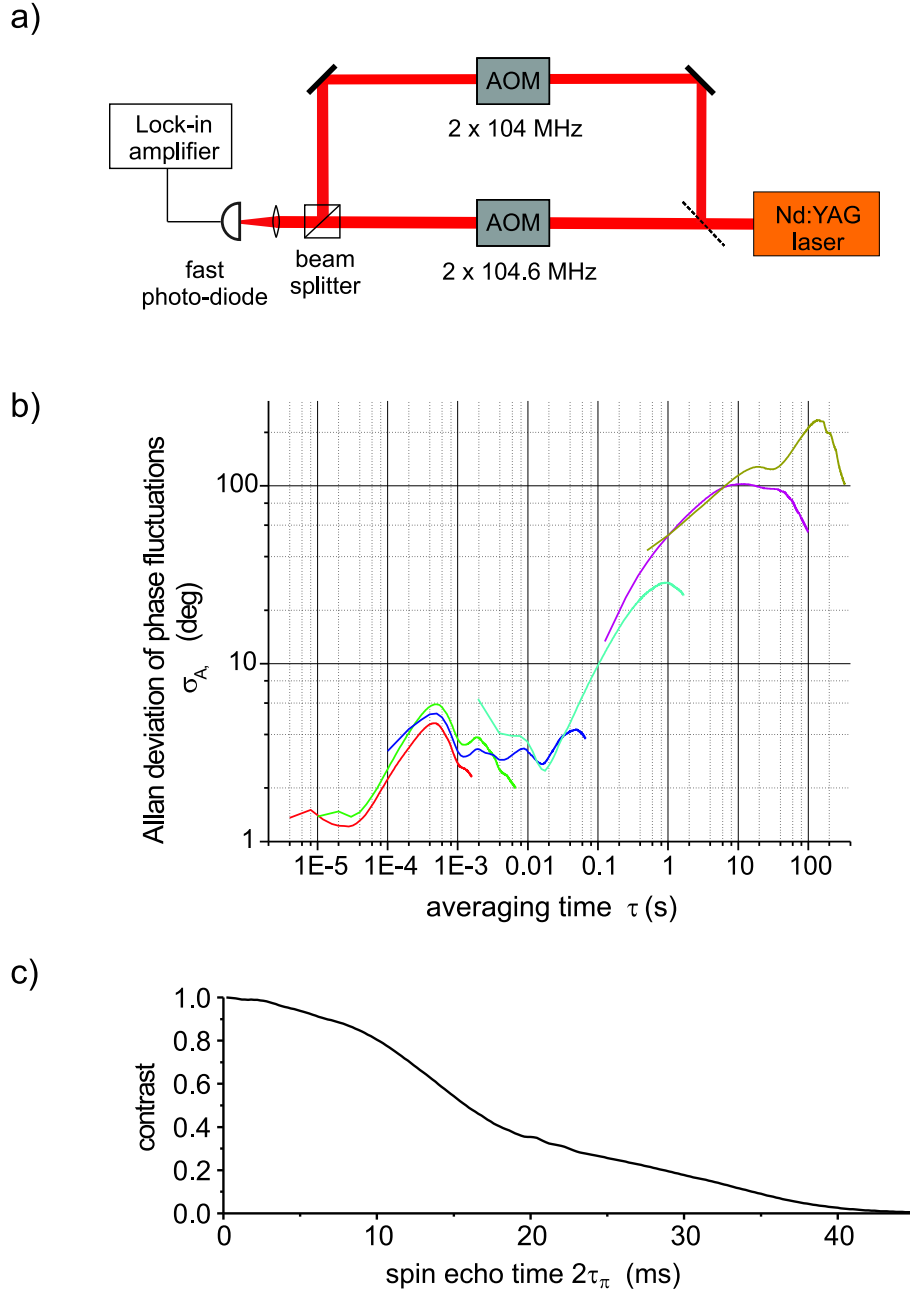


Figure 2.22: Measurement of axial position fluctuations of the dipole trap. (a) Experimental setup. The relative optical phase between the two trapping beams is measured interferometrically. (b) The Allan deviation of the phase fluctuations, calculated from the resulting data traces according to Equation (2.45), is plotted versus the averaging time on a logarithmic scale. (c) The expected spin echo contrast is shown as a function of the spin echo time according to Equations (2.28) and (2.46).

where $\bar{x}_{\tau,k}$ denotes the average of the relative phase over the k -th time interval τ . The result is shown in Figure 2.22 (b) as a function of the averaging time τ . For small averaging times $\tau < 0.01$ s, acoustic vibrations of the mirrors, which steer the trapping laser beams, probably cause the optical phase fluctuations in a frequency band of 100 Hz – 10 kHz. For larger averaging times, air flows across the optical table cause thermal changes of the optical path lengths and are most likely responsible for the observed phase fluctuations.

The Allan deviation of the phase fluctuations translates into fluctuations of the detuning $\sigma_{\Delta\delta}$:

$$\sigma_{\Delta\delta}(\tau) = \sqrt{2} \frac{\sigma_A(\tau)}{360^\circ} \frac{\lambda}{2} \omega'. \quad (2.46)$$

The factor of $\sqrt{2}$ arises because $\sigma_{\Delta\delta}(\tau)$ is the standard deviation of the difference of two detunings with standard deviation σ_A each. The expected decay of the spin echo contrast according to Equation (2.28) is plotted in Figure 2.22 (c) as a function of the spin echo time $2\tau_\pi$. The expected homogeneous dephasing time obtained from this graph is $T_2' = 21$ ms. This time is more than one order of magnitude larger than the dephasing time due to the radial oscillations of the trapped atoms and can therefore be neglected at the current stage of our experiment.

2.4.8 Discussion

All relevant dephasing times are summarized in Table 2.7.

Dephasing and relaxation times			limited by
inhomogeneous dephasing time in the guiding field $B_0 = 2$ G	T_2^*	$270 \pm 25 \mu\text{s}$	energy dependent light shift distribution of the atoms
homogeneous dephasing time in the guiding field $B_0 = 2$ G	T_2'	3.5 ms	magnetic field fluctuations
dephasing time in the magnetic field gradient $B' = -1.5$ mG/ μm	\hat{T}_2	600 μs	radial oscillation of the atoms in the magnetic field gradient
population relaxation time	T_1	86 s	scattering of photons from the dipole trap laser

Table 2.7: Overview of the dephasing and relaxation times in a dipole trap of $U_0 = 100 \mu\text{K}$.

The coherence time of our quantum register is limited by dephasing due to the radial oscillations of the atoms in the magnetic field gradient. This dephasing mechanism is caused by an inhomogeneous broadening of the atomic resonance frequency which is reversible by a spin echo pulse only for certain periodic delay times. Therefore, the corresponding dephasing time should not be associated with the standard T_2' or T_2^* times. I have instead labelled this time by \hat{T}_2 .

If this dephasing mechanism can be eliminated following the suggestions listed in Section 2.4.7, the coherence time of the quantum register will be limited by dephasing within the guiding field. The temperature distribution of the trapped atoms along with the contribution of the circular polarization to the differential light shift results in inhomogeneous dephasing denoted by T_2^* . However, this effect can be reversed by a spin echo pulse. The dominant homogeneous and irreversible dephasing (T_2') is most likely caused by magnetic field fluctuations.

In addition to decreasing or even eliminating the identified decoherence mechanisms, a possible way of increasing the coherence time of the quantum register is the transfer of the atoms to decoherence-free states between addressing operations. As one example, the population of the qubit state $|1\rangle$ corresponding to state $|F=3, m_F=-3\rangle$ could be buffered in the ancilla state $|F=4, m_F=-3\rangle$ by coherent population transfer at the respective resonance frequency. In this case, all fluctuations relating to magnetic field and circular light shift sensitivity are suppressed by a factor of 7. Experimentally more complicated but more effective, a coherent adiabatic transfer of the qubit states onto the magnetically insensitive $m_F=0$ states between computational operations of the quantum register would suppress all fluctuations by two orders of magnitude.

Despite the numerous possibilities to extend the coherence time of the quantum register, the currently limiting timescale of $\hat{T}_2 = 600 \mu\text{s}$ is still two orders of magnitude larger than the measured one-qubit gate operation time of the Hadamard gate ($8 \mu\text{s}$) and the expected two-qubit entanglement times ($900 \text{ ns} - 14 \mu\text{s}$), see Appendix B. It should thus be possible to perform many computational steps on the quantum register even within its current coherence time.

Chapter 3

Conclusion and outlook

I have presented the realization of a neutral atom quantum register which constitutes an essential building block of a quantum computer. This is a significant achievement on the route to quantum computing with neutral atomic particles. It fulfils all but one of the five criteria for building a quantum computer by DiVincenzo [26]: (1) a scalable physical system with well characterized qubits, (2) the ability to initialize the state of the qubits to a simple fiducial state, (3) coherence times that are significantly longer than the gate operation times, (4) a universal set of quantum gates, and (5) a qubit specific measurement capability.

(1) The quantum register consists of a string of an exactly known number of single atoms each of which is confined in the potential well of a standing wave optical dipole trap. The trap provides sub-micrometer localization and the possibility to transport the atoms along the trap axis. Molasses illumination in the dipole trap allows us to cool and continuously image the trapped atoms. The quantum information is encoded in the hyperfine ground states of the atom qubits. While the experiments described in this thesis have been performed with up to five qubits, the quantum register should be scalable to larger qubit numbers, see Section 2.3.5.

(2) and (5) State initialization and detection of the quantum register are performed by optical pumping and the application of a state-selective push-out laser, respectively. While the preparation and detection of the internal atomic states are performed with efficiencies compatible with 100 %, the control of motional states remains to be implemented. A possible way of preparing the oscillatory ground state of a trapped atom are Raman cooling techniques [85, 86, 87] which we have started to explore [64].

(3) Detailed analysis of the coherence properties of the quantum register reveals coherence times of 600 μ s. They are limited by dephasing due to the radial oscillations of the trapped atoms within the inhomogeneous magnetic field. Yet, they are two orders of magnitude larger than the demonstrated one-qubit gate operation times.

(4) While we have not yet realized a universal set of quantum gates, I have demonstrated reliable operation of one-qubit gates in this thesis. The application of a magnetic field gradient along the trap axis allows us to spectroscopically resolve the trapped atoms

and to perform selective coherent one-qubit operations on the quantum register. With an addressing resolution of $2.5 \mu\text{m}$ quantum information is thus written onto individual qubits. The demonstrated individual addressing of trapped neutral atoms constitutes a crucial step on the route to quantum computation with neutral atoms and is considered one of seven “trophies” in the neutral atom quantum computing road map [27].

The demonstration of a two-qubit quantum gate is essential to fulfil criterion (4). We have therefore designed our experimental setup to be compatible with the requirements to implement this next logical step – the realization of a two-qubit quantum logic gate via the exchange of photons between two atoms.

3.1 A cavity-QED quantum gate with neutral atoms

There is a plenitude of proposals of how to implement a two-qubit quantum gate with neutral atoms which suggest the coherent photon exchange of two atoms inside a high-finesse optical resonator [20, 88, 89, 90]. The experimental challenges for their realization are quite demanding. Although there has been a number of successes in optical cavity-QED research recently, including the transport of atoms into a cavity [91], trapping of single atoms inside a cavity [92], single photon generation [93, 94], feedback control of the atomic motion in a cavity [95, 96], and cooling of atoms inside a cavity [97, 98], the realization of a two-qubit quantum gate remains to be shown.

3.1.1 An optical high-finesse resonator for storing photons

Our goal is the deterministic placement of two atoms inside an optical high-finesse resonator. For this purpose, we have already set up and stabilized a suitable resonator [54], a photo of which is shown in Figure 3.1 (a), whereas the schematic in Figure 3.1 (b) illustrates the planned geometry. We plan to transport atoms from the MOT, which is a few millimeters away from the cavity, into the cavity mode using our optical conveyor belt.

Employing the imaging techniques and the image analysis presented in this thesis, we were recently able to control the position of the trapped atoms along the trap axis with a precision of 300 nm [58]. This should allow us to reliably place the atoms into the center of the cavity mode, which has a diameter of $10 \mu\text{m}$. Since the demonstrated one-qubit operations on the quantum register do not require optical access to the trapped atoms, they can even take place inside the cavity.

3.1.2 A four-photon entanglement scheme

One of the most promising schemes to create entanglement between two atoms was proposed by L. You et al. [99] and is the basis for the realization of a quantum phase gate [89]. It relies on the coherent energy exchange between two atoms stimulated by a four-photon Raman process involving the cavity mode and an auxiliary laser field. I have determined optimized theoretical parameters and calculated the expected fidelity according to this proposal for our particular experimental conditions, see Appendix B. With a maximum

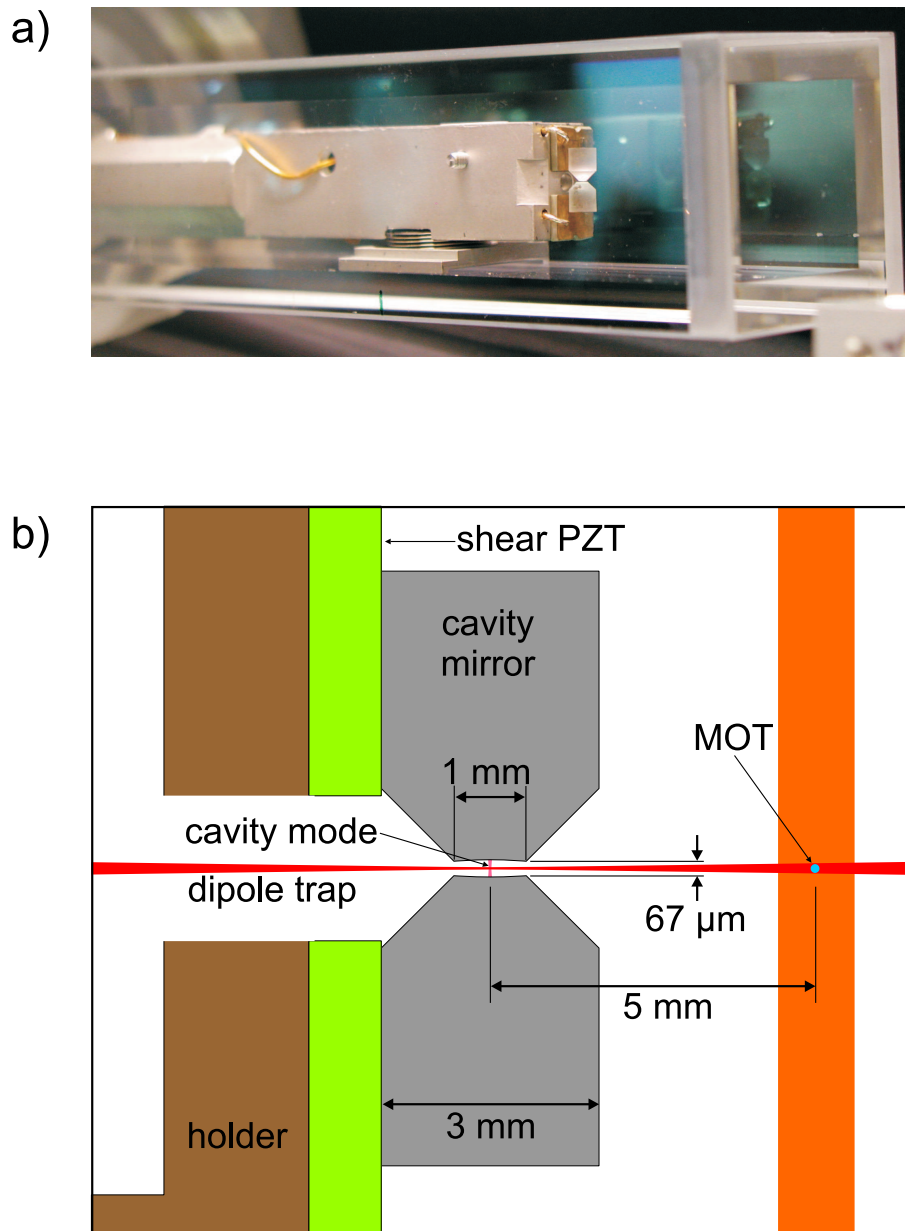


Figure 3.1: a) Picture of the high-finesse resonator which is set up in our laboratory. b) Planned experimental geometry for the deterministic transport of atoms from the MOT inside the cavity mode using our optical conveyor belt.

fidelity of $F = 85\%$, which can be expected from this calculation, the demonstration of entanglement and the implementation of a quantum gate seems feasible with our experimental apparatus.

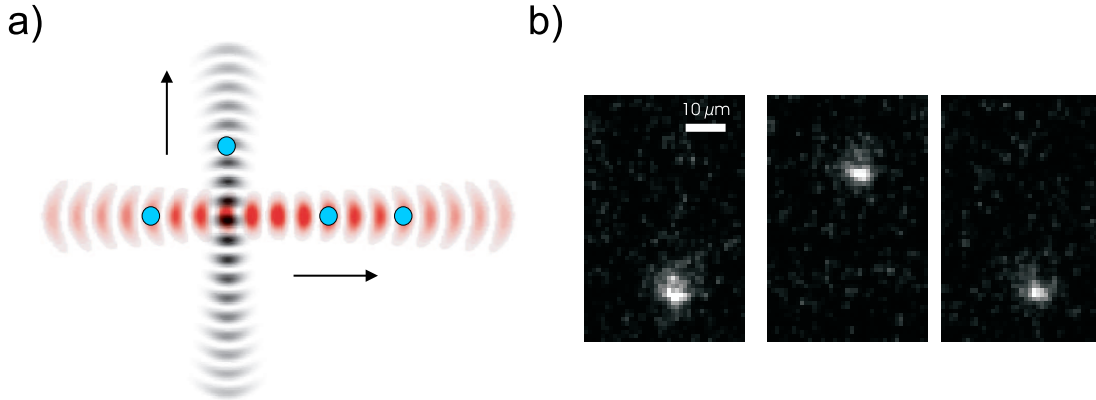


Figure 3.2: Single atom sorting with a vertical conveyor belt. a) Working principle. A selected atom is pulled out of the string of atoms, so that the horizontal conveyor belt can shift the relative position of the other atoms before the selected atom is placed back into the quantum register. b) First pictures of a single atom being transported up and down using the vertical conveyor belt.

3.2 Single atom sorting

In addition to the five DiVincenzo criteria for building a quantum computer, further requirements need to be fulfilled for fault tolerant computation. One of them demands that gates should act on any pair of qubits [100]. However, for the realization of a quantum gate by photon exchange, it is essential to simultaneously couple the two involved atoms to the same cavity mode. A two-qubit operation on an arbitrary pair of qubits of the quantum register therefore requires that these two atoms are placed next to each other, at a distance which is smaller than the diameter of the cavity mode.

In analogy to the proposed architecture for a large-scale ion trap quantum computer [101], our current efforts are directed towards the implementation of a “single atom sorting machine”. It should permit to sort the qubits of the quantum register in any desired order so that arbitrary pairs of qubits can be placed into the cavity mode. For this purpose, we have set up a second optical conveyor belt, oriented perpendicularly to the current dipole trap. It is designed to pull out a selected atom from the trapped atom string, see Figure 3.2 (a). Subsequent shifting of the quantum register with the horizontal conveyor belt moves all other atoms relative to the selected one. Finally, this atom shall be placed back into the quantum register, at the desired position. Figure 3.2 (b) demonstrates the first operation of the vertical conveyor belt, where a single atom is transported up and down over a few tens of micrometers.

As a further application, such a sorting device could create an atom string with equidistant spacing. This would overcome the current limitation to the size of the quantum register, where the atoms are loaded into random lattice sites, see also Section 2.3.5.

The focussing optics of this vertical dipole trap are designed such that the waist of the trapping laser beam is $w_0 = 7 \mu\text{m}$. The radial extent of the thermally distributed atom in

the trap is then $\sigma_{\text{rad}} = 1 \mu\text{m}$ so that the controlled placement of an atom into a desired potential well of the horizontal dipole trap might be possible. If this is accomplished, experiments studying collisional properties of two atoms trapped in the same potential well seem to be feasible.

3.3 A single-atom interferometer

An alternative route to produce entanglement could be offered by the implementation of a single atom interferometer. Here, the wavefunction of a single atom is coherently split and delocalized using spin-dependent trapping potentials [102]. At a certain wavelength between the D1 and the D2 transition (for cesium: $\lambda = 867.5 \text{ nm}$), the scalar and vectorial light shift interact such that one qubit state $|0\rangle$ is only trapped in a σ^+ -polarized trap while the other state $|1\rangle$ is only sensitive to a trap of opposite polarization σ^- . The polarization of the light field of two counter-propagating linearly polarized beams can be decomposed into a standing wave light field of purely σ^+ polarization and one of purely σ^- polarization. When the angle between the linear polarization vectors of these two trapping laser beams is rotated, the σ^+ and σ^- components of the standing wave are shifted into opposite directions and thus the direction in which a trapped atom is transported depends on its spin state. In case it is prepared in a superposition state $(|0\rangle + |1\rangle)/\sqrt{2}$, the wavefunction of the atom is coherently split. After application of a phase shift to one part of the wavefunction, subsequent merging of the wavefunction and application of a second $\pi/2$ pulse will lead to the observation of interference fringes. While a similar experiment has already been demonstrated with a large ensemble of atoms [18, 103], it remains to be shown with a single atom or with a few individually addressable atom qubits.

While this demonstration would be an impressive experiment per se, it might lead to further applications. As one example, the wavefunctions of two distant atoms could be brought into partial overlap depending on their spin states. The resulting spin-dependent collisional phase shift of the two wavefunctions could be used to implement a quantum phase gate and to produce entanglement between the two atoms [104]. In this context, it is essential to exactly know the distance of the two atoms so that the transport distance can be chosen such that their wavefunctions overlap maximally. Recent investigations have proven that we can determine the relative distance between two trapped atoms with a precision of better than 300 nm [58]. Since this precision exceeds the spacing of the potential wells of 532 nm, we know exactly by how many potential wells two atoms are separated.

Appendix A

Light shifts in multi-level atoms

I present a calculation for the light shifts of atomic levels due to the interaction of an atom with an off-resonant laser. From the general calculation I derive approximate formulas for the ground states of cesium.

A perturbative description of the interaction of the classical field $\mathbf{E}(t) = \mathbf{E}_0 \cos \omega t$ with a multi-level atom yields the light shift ΔE_i of the atomic level $|i\rangle$ with an eigenenergy of E_i and quantum numbers n, J, F, m [105]:

$$\Delta E_i = -\frac{1}{4} \sum_{n', J', F', m'} \frac{1}{\hbar \Delta'_{if}} \left| \langle n J I F m | \hat{\mathbf{d}} \cdot \mathbf{E} | n' J' I F' m' \rangle \right|^2. \quad (\text{A.1})$$

The sum covers all states $|f\rangle$ with quantum numbers n', J', F', m' and energies $E_f \neq E_i$, and $\hat{\mathbf{d}}$ is the atomic dipole operator. The effective detuning Δ'_{if} is defined as:

$$\frac{1}{\hbar \Delta'_{if}} := \frac{1}{\hbar(\omega_{if} - \omega)} + \frac{1}{\hbar(\omega_{if} + \omega)}, \quad (\text{A.2})$$

where $\omega_{if} = (E_f - E_i)/\hbar$ is the transition frequency between levels $|i\rangle$ and $|f\rangle$.

After expanding the interaction Hamiltonian $H = -\hat{\mathbf{d}} \cdot \mathbf{E}$ into spherical tensors we apply the Wigner-Eckart theorem [106] to eliminate the m dependence in Equation (A.1):

$$\Delta E_i = -\frac{1}{4} \sum_{n', J', F', m'} \frac{1}{\hbar \Delta'_{if}} |E_0|^2 \begin{pmatrix} F & 1 & F' \\ -m & -\mu & m' \end{pmatrix}^2 |\langle n J I F || d || n' J' I F' \rangle|^2. \quad (\text{A.3})$$

The 3-J symbol now contains the coupling strength between different m levels which depends on the polarization of the light field, $\mu = \pm 1 \leftrightarrow \sigma^\pm$ -pol., $\mu = 0 \leftrightarrow \pi$ -pol. The dipole matrix elements are further reduced by extracting the hyperfine coupling [107]:

$$\langle n J I F || d || n' J' I F' \rangle = \sqrt{(2F+1)(2F'+1)} (-1)^{J+I+F'+1} \begin{Bmatrix} J & F & I \\ F' & J' & 1 \end{Bmatrix} \langle n J || d || n' J' \rangle, \quad (\text{A.4})$$

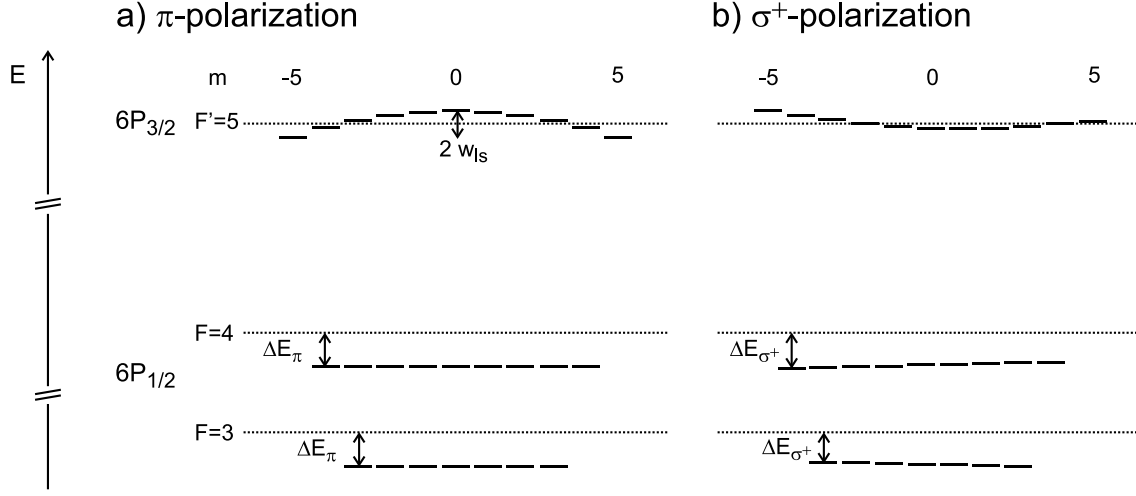


Figure A.1: Light shift of the Zeeman multiplicity of the two ground states and the $F' = 5$ – excited state of the D2 transition for pure π (a) and pure σ^+ polarization (b) of the electro-magnetic field. The maximum splitting of the Zeeman levels due to the tensorial contribution to the light shift of the excited state is denoted by $2w_{ls}$. The dotted lines show the unperturbed states. For illustration, the energy scale is interrupted twice.

where the curly brackets $\{ \}$ denote a 6-J symbol. After the elimination of both m and F dependence, the remaining dipole matrix elements are expressed as a function of the oscillator strengths f_{if} for the transitions $nJ \rightarrow n'J'$:

$$f_{if} = \frac{2m_e}{3\hbar e^2} \frac{\omega_{if}}{2J+1} |\langle nJ || d || n'J' \rangle|^2 \quad (\text{A.5})$$

which have been calculated and measured for many elements. (For cesium, see reference [108].) Putting together equations (A.3), (A.4), and (A.5), we receive a universal expression for the light shift of level $|i\rangle$ which only depends on its quantum numbers, the polarization of the light, and the respective oscillator strengths and transition frequencies to the other levels:

$$\Delta E(n, J, F, m, \mu) = -\frac{3e^2 I}{4mce_0} (2J+1)(2F+1) \sum_{n', J', F', m'} (2F'+1) \frac{f_{if}}{\omega_{if} \Delta'_{if}} \begin{pmatrix} F & 1 & F' \\ -m & -\mu & m' \end{pmatrix}^2 \left\{ \begin{matrix} J & F & I \\ F' & J' & 1 \end{matrix} \right\}^2 \quad (\text{A.6})$$

In our case of cesium atoms interacting with a far red-detuned light field, only the first excited states $6P_{1/2}$ and $6P_{3/2}$ (see Figure 1.4) significantly contribute to the light shift of the $6S_{1/2}$ ground state. Their oscillator strengths amount to 1/3 and 2/3, respectively, so that Equation (A.6) yields the following two equations for π and σ^\pm polarization:

$$\Delta E_\pi(\mathbf{r}) = -\frac{e^2}{12mce_0} \left[\frac{2}{\omega_{3/2} \Delta'_{3/2}} + \frac{1}{\omega_{1/2} \Delta'_{1/2}} \right] I_\pi(\mathbf{r}), \quad (\text{A.7})$$

$$\Delta E_{\sigma^\pm}(\mathbf{r}) = -\frac{e^2}{12m c \epsilon_0} \left[\frac{2 \pm g_F m_F}{\omega_{3/2} \Delta'_{3/2}} + \frac{1 \mp g_F m_F}{\omega_{1/2} \Delta'_{1/2}} \right] I_{\sigma^\pm}(\mathbf{r}). \quad (\text{A.8})$$

Here, the Landé factors $g_4 = -g_3 = 1/4$ have been introduced. The relation

$$\frac{1}{\Delta'_{J'}} = \frac{1}{\omega_L + \omega_{J'}} + \frac{1}{\omega_L - \omega_{J'}} \quad (\text{A.9})$$

defines the effective detuning $\Delta'_{J'}$ of the dipole trap laser from the ${}^6P_{J'}$ state. While the light shift for π polarization does not depend on the m_F sublevels (see Figure A.1 (a)), this degeneracy is lifted in the case of a circularly polarized light field (see Figure A.1 (b)). This effect is analogous to the Zeeman shift of the atomic levels in a magnetic field.

In the case of a perfectly linearly polarized dipole trap, Equation (A.7) yields the dipole potential:

$$U(\mathbf{r}) = \Delta E_\pi(\mathbf{r}) = \frac{\hbar \Gamma}{8} \frac{I_\pi(\mathbf{r})}{I_0} \frac{\Gamma}{\Delta'_{\text{eff}}}, \quad (\text{A.10})$$

using the approximation $\omega_0 = \omega_{3/2} = \omega_{1/2}$. The effective laser detuning

$$\frac{1}{\Delta'_{\text{eff}}} = \frac{1}{3} \left(\frac{2}{\Delta'_{3/2}} + \frac{1}{\Delta'_{1/2}} \right) \quad (\text{A.11})$$

takes into account both contributions from the $D1$ and the $D2$ lines. This result agrees well with the classically calculated dipole potential of Equation (1.7).

For the calculation of the light shift of the excited states, the simplifying assumptions for the ground states do not hold. First, their coupling both to the ground states and to higher excited states have to be considered. In addition, for states with angular momentum $J > 1/2$, Equation (A.6) yields a quadratic m_F -sublevel dependence, independent of the polarization of the field:

$$\Delta E(J > 1/2) = \alpha_{\text{sc}} + \alpha_{\text{vec}} m_F + \alpha_{\text{ten}} m_F^2, \quad (\text{A.12})$$

where α_{sc} , α_{vec} , and α_{ten} denote the scalar, vectorial, and tensorial contributions to the overall light shift. Again, if the electro-magnetic field is purely π polarized, the vectorial term vanishes, $\alpha_{\text{vec}} = 0$. In our case, the quadratic term in Equation (A.12) causes a splitting of the excited $6P_{3/2}$ state which results in an effective broadening of the D2 transition by $2w_{\text{ls}}$ (see Figure A.1 (a)). For $F' = 5$ and π polarization, $2w_{\text{ls}}$ amounts to 75 % of the ground state light shift ΔE_π for unpolarized atoms.

Appendix B

An entanglement scheme for two atoms in a cavity

The ability to create entanglement between two atoms demonstrates that the experimental control of their interaction is sufficient to also implement two-qubit quantum gates. Here, I sketch an entanglement scheme presented in Reference [99], which relies on the coherent energy exchange between two atoms coupled to the same mode of a high-finesse cavity, and determine optimized theoretical parameters for our particular experimental system.

B.1 Hamiltonian of a coupled atom-atom-cavity system

I consider two three-state atoms A and B with two ground state levels $|i\rangle_{A/B}$ and $|a\rangle_{A/B}$, and an excited state $|e\rangle_{A/B}$, with energies E_i , E_a , and E_e , respectively, see Figure B.1 (a). The ground state of the cavity is labelled $|0\rangle_C$, corresponding to an empty cavity, and its first excited state $|1\rangle_C$, with exactly one photon populating the cavity. All higher excited cavity states are neglected. In addition to the cavity field, an auxiliary laser field is required which can be shined in along the dipole trap axis, see Figure B.1 (b). Its frequency ω_L is off-resonant with respect to the $|i\rangle \leftrightarrow |e\rangle$ transition, with a detuning of $\Delta = \omega_L - (E_e - E_i)/\hbar$. The coupling strength of the laser beam to the atoms A and B is denoted by the resonant Rabi frequencies Ω_A and Ω_B , respectively. The cavity mode with a resonance frequency ω_C couples the states $|e\rangle$ and $|a\rangle$. The coherent coupling strength g between an atom and a one-photon cavity field is equal to [109]:

$$g = \sqrt{\frac{d^2\omega_0}{2\hbar\epsilon_0 V}}. \quad (\text{B.1})$$

Here, $d = \langle e | e\hat{r} | a \rangle$ is the electric dipole moment of the atom, V is the volume of the cavity mode, and ω_0 is the atomic resonance frequency. The auxiliary laser and the cavity field couple the two ground states $|i\rangle$ and $|a\rangle$ via a two-photon Raman transition, with a Raman detuning of $\delta = \omega_L - \omega_C - (E_a - E_i)/\hbar$.

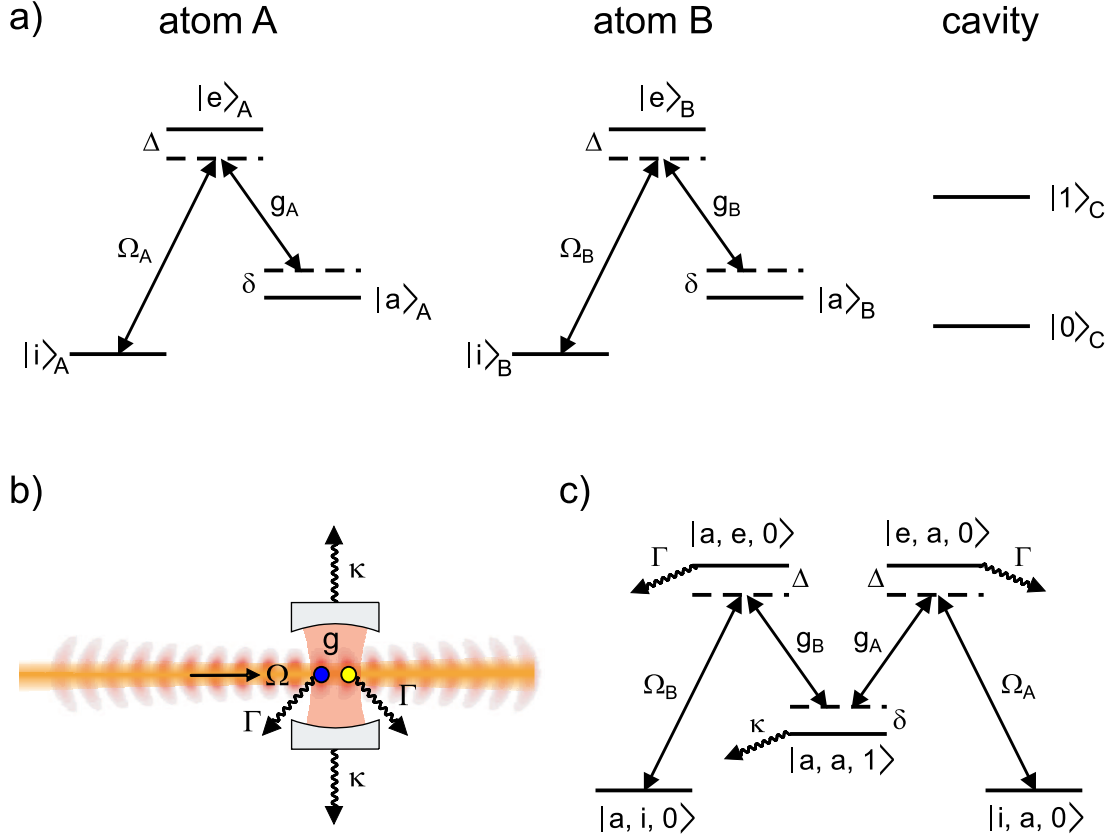


Figure B.1: Four-photon Raman resonance between two atoms and a cavity mode. a) Level scheme of both atoms and the cavity. b) Scheme of the experimental geometry. Two trapped atoms are placed inside the cavity mode (coupling constant g) and are illuminated by an auxiliary laser (coupling constant Ω). Γ denotes the spontaneous emission rate and κ the cavity decay rate. c) Relevant dressed states of the atom-atom-cavity system. The two states $|a, i, 0\rangle$ and $|i, a, 0\rangle$ are resonantly coupled by a four-photon Raman transition.

In the interaction picture, the Hamiltonian reads [99]:

$$\hat{H}_{\text{atom}} = \hbar\Delta \sum_{\mu=A,B} |e\rangle_{\mu} \langle e|_{\mu} \quad (\text{B.2})$$

$$\hat{H}_{\text{cavity}} = \hbar\delta \hat{c}^{\dagger} \hat{c} \quad (\text{B.3})$$

$$\hat{H}_{\text{int}} = \sum_{\mu=A,B} \left[\frac{1}{2} i\hbar\Omega_{\mu} |e\rangle_{\mu} \langle i|_{\mu} + i\hbar g_{\mu} \hat{c} |e\rangle_{\mu} \langle a|_{\mu} + h.c. \right] \quad (\text{B.4})$$

$$\hat{H} = \hat{H}_{\text{atom}} + \hat{H}_{\text{cavity}} + \hat{H}_{\text{int}}. \quad (\text{B.5})$$

Here \hat{c}^{\dagger} and \hat{c} are the photon creation and annihilation operators. The relevant dressed states of this atom-atom-cavity system are depicted in Figure B.1 (c). The states $|a\rangle_A |i\rangle_B |0\rangle_C := |a, i, 0\rangle$ and $|i, a, 0\rangle$ are resonantly coupled by a four-photon Raman

transition. Its effective four-photon Rabi frequency in the far off-resonant limit $|\Delta| \gg \Omega_\mu$, $|\delta| \gg g_\mu$, and $|\delta\Delta| \gg g_\mu^2$, reads:

$$\Omega_{\text{eff}} = \frac{\Omega_A \Omega_B g_A g_B}{2\Delta^2 \delta}. \quad (\text{B.6})$$

If the system is initially prepared in state $|a, i, 0\rangle$, a $\pi/2$ pulse coherently rotates it into the Bell state

$$\Psi_{\text{Bell}} = \frac{|a, i\rangle + i|i, a\rangle}{\sqrt{2}}, \quad (\text{B.7})$$

where the two atoms are maximally entangled.

B.2 Master equation approach to model dissipation

As soon as there is an excitation in the system, it is subject to dissipation, which destroys the coherence. If an atom is in the excited state, it spontaneously decays to the ground states at the rate Γ , see Figure B.1 (b) and (c). The excited cavity state $|1\rangle_C$ decays to the cavity ground state $|0\rangle_C$ at the rate κ , which includes all loss mechanisms such as cavity transmission through one of the mirrors, absorption, diffraction etc. Dissipation is formally introduced by the collapse operator [109, 110]:

$$\hat{C} = \sum_{\mu=A,B} \sqrt{\frac{\Gamma}{2}} \left(|a\rangle_\mu \langle e|_\mu + |i\rangle_\mu \langle e|_\mu \right) + \sqrt{\kappa} \hat{c}. \quad (\text{B.8})$$

The time evolution of the system is then described by the master equation [109, 111, 112]:

$$\frac{d\hat{\rho}}{dt} = \mathcal{L}\hat{\rho}, \quad (\text{B.9})$$

with the density operator $\hat{\rho}$ and the Liouvillian \mathcal{L} , which is defined as:

$$\mathcal{L}\hat{\rho} = -\frac{i}{\hbar} [\hat{H}, \hat{\rho}] + \hat{C}\hat{\rho}\hat{C}^\dagger - \frac{1}{2}\hat{C}^\dagger\hat{C}\hat{\rho} - \frac{1}{2}\hat{\rho}\hat{C}^\dagger\hat{C}. \quad (\text{B.10})$$

B.3 Numerical calculation for our system parameters

The solution of Equation (B.9),

$$\hat{\rho}(t) = e^{\mathcal{L}t} \hat{\rho}_0, \quad (\text{B.11})$$

with a given initial condition $\hat{\rho}_0 = \hat{\rho}(0)$, is computed numerically using the Quantum Optics Toolbox [110] under Matlab, which provides a number of numerical routines specifically designed to tackle typical problems in quantum optics.

For the calculation I assume that the Rabi frequency due to the auxiliary laser $\Omega = \Omega_A = \Omega_B$ as well as the single photon coherent coupling rate $g = g_A = g_B$ are equal for both atoms. Initially, the system is prepared in state $|a, i, 0\rangle$ so that the density operator at $t = 0$ is equal to:

$$\hat{\rho}_0 = |a, i, 0\rangle \langle a, i, 0|. \quad (\text{B.12})$$

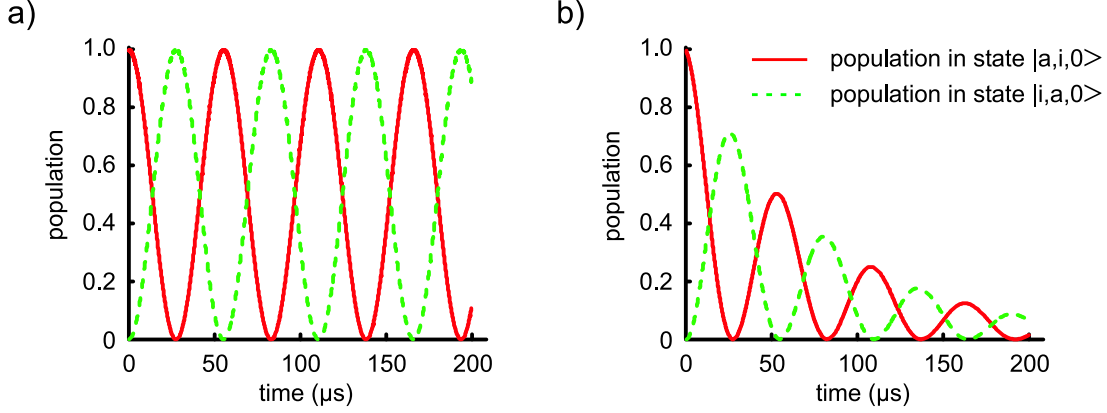


Figure B.2: Calculated time evolution of the four-photon Rabi oscillation. The states $|a, i, 0\rangle$ and $|i, a, 0\rangle$ coherently exchange energy at the Rabi frequency Ω_{eff} . (a) Without dissipation, $\Gamma = \kappa = 0$. (b) With dissipation. A list of all parameters can be found in Table B.1.

Neglecting dissipation, $\Gamma = \kappa = 0$, the resulting populations in the states $|a, i, 0\rangle$ and $|i, a, 0\rangle$,

$$P_{a,i,0} = \text{Tr}\{|a, i, 0\rangle \langle a, i, 0| \hat{\rho}(t)\} \quad (\text{B.13})$$

$$P_{i,a,0} = \text{Tr}\{|i, a, 0\rangle \langle i, a, 0| \hat{\rho}(t)\}, \quad (\text{B.14})$$

are plotted as a function of time in Figure B.2 (a), for the parameters given in Table B.1. The graph shows the resulting coherent energy exchange between the two atoms at the effective Rabi frequency $\Omega_{\text{eff}}/2\pi = 18$ kHz.

The figure of merit which quantifies how well the system has actually evolved to the desired Bell state Ψ_{Bell} , is the fidelity F . It is defined as the overlap integral between Ψ_{Bell} and the system state after a quarter Rabi period $T_{\pi/2}$:

$$F = \langle \Psi_{\text{Bell}} | \hat{\rho}_{\text{atom}}(T_{\pi/2}) | \Psi_{\text{Bell}} \rangle, \quad (\text{B.15})$$

where

$$\hat{\rho}_{\text{atom}}(t) = \text{Tr}_{\text{C}}(\hat{\rho}(t)) \quad (\text{B.16})$$

is the density operator traced over the cavity states. The partial trace is performed because we are only interested in the atomic states and disregard the cavity states. In the ideal case of no dissipation, $F = 1$ showing that the system has evolved to the maximally entangled Bell state. However, dissipation crucially governs the dynamics of the system and causes the fidelity to be smaller than one. If the fidelity is as low as $F = 0.5$, the system state corresponds to a statistical mixture of the states $|a, a\rangle$, $|i, i\rangle$, $|a, i\rangle$, and $|i, a\rangle$. In general, successful creation of entanglement and implementation of quantum gates is only possible in the strong coupling regime, where the rate of coherent energy exchange between atom and cavity field is significantly larger than the dissipation rates. This condition is usually

summarized in the strong coupling parameter [99]:

$$\frac{g^2}{\kappa\Gamma} \gg 1. \quad (\text{B.17})$$

Cavity parameters

Maximization of the strong coupling parameter is an essential condition to achieve high fidelities. In order to achieve a large g , the cavity mode volume V must be small according to Equation (B.1). The mode volume of our cavity:

$$V = \frac{\pi}{4} L w_0^2 = \frac{\lambda}{4} L \sqrt{\frac{LR_c}{2}} \quad (\text{B.18})$$

is therefore minimized by choosing the cavity length L as small as possible. Its current length of $L = 92 \mu\text{m}$ is limited by the condition that the focussed dipole trap laser still needs to fit in between the two mirrors without scattering too much light. In Equation (B.18), $w_0 = 13 \mu\text{m}$ denotes the waist of the cavity mode, $\lambda = 852 \text{ nm}$ is its wavelength, and $R_c = 1 \text{ cm}$ is the curvature of the cavity mirrors. Our cavity is set up in the Fabry-Perot regime, with $L \ll R_c$, where Equation (B.18) is a valid approximation.

Since the cavity decay rate κ should be as small as possible to fulfil the strong coupling condition (B.17), the mirror reflectivity and thus the finesse \mathcal{F} of the cavity must be very high. While the finesse of the current cavity was measured to be $\mathcal{F} = 1.2 \cdot 10^5$, yielding a strong coupling parameter of $g^2/(\kappa\Gamma) = 22$, the company Research Electro-Optics in Boulder – in cooperation with us – has recently managed to manufacture mirrors with a reflectivity corresponding to a cavity finesse as high as $\mathcal{F} = 1.0 \cdot 10^6$. As

$$\frac{\kappa}{2\pi} = \frac{c}{2L} \cdot \frac{1}{\mathcal{F}}, \quad (\text{B.19})$$

the cavity decay rate is reduced by an order of magnitude and is equal to $\kappa/2\pi = 1.6 \text{ MHz}$. However, the excellent mirror quality was only achieved at the expense of a larger radius of curvature of $R_c = 5 \text{ cm}$. Putting together Equations (B.1) and (B.18), the expected single photon coherent coupling rate is $g/2\pi = 27 \text{ MHz}$, see Table B.1, yielding a strong coupling parameter of $g^2/(\kappa\Gamma) = 91$.

Expected fidelity of the entanglement scheme

In addition to maximizing the strong coupling parameter, the other free parameters of the entanglement scheme have to be chosen properly in order to achieve a high fidelity F . To minimize dissipation, it is essential to avoid off-resonant excitation of the excited atomic and cavity states. I have therefore chosen the detunings such that $\Delta \gg \Gamma$ and $\delta \gg \kappa$. Also, the intensity of the auxiliary laser should be chosen such that $\Delta \gg \Omega \gg \Gamma$. Iterative fine-tuning of all parameters for maximum F yields the parameter set given in Table B.1 with an expected fidelity of $F = 85 \%$. For these parameters I have plotted the populations of state $|a, i, 0\rangle$ and $|i, a, 0\rangle$ in Figure B.2 (b). Again, they illustrate the coherent energy

Laser and cavity parameters		
Rabi frequency of auxiliary laser	$\Omega/2\pi$	50 MHz
single photon coherent coupling rate	$g/2\pi$	27 MHz
detuning from the excited atomic state	$\Delta/2\pi$	1600 MHz
detuning from the excited cavity state	$\delta/2\pi$	20 MHz
Dissipation rates		
spontaneous emission rate	$\Gamma/2\pi$	5 MHz
cavity decay rate ($\mathcal{F} = 10^6$)	$\kappa/2\pi$	1.6 MHz
Results		
fidelity	F	85 %
effective four-photon Rabi frequency	$\Omega_{\text{eff}}/2\pi$	18 kHz
strong coupling parameter	$g^2/\kappa\Gamma$	91

Table B.1: Parameters for the calculation of Figure B.2. The Rabi frequency $\Omega = \Omega_A = \Omega_B$ and the single photon coherent coupling rate $g = g_A = g_B$ are assumed to be equal for both atoms.

exchange between the two states at the frequency Ω_{eff} , however with decaying amplitude during the time of two Rabi cycles due to the dissipation of the system.

The two-qubit entanglement time, which is required to transfer the system from the initial state to the entangled state, is equal to $T_{\pi/2} = 14 \mu\text{s}$. Note that at the expense of a slightly lower fidelity of $F = 83 \%$, the gate operation speed can be increased to $T_{\pi/2} = 900 \text{ ns}$ by choosing a smaller detuning of $\Delta/2\pi = 400 \text{ MHz}$.

I have optimized the theoretical parameters for the presented entanglement scheme on the basis of our particular experimental conditions. It thus seems feasible to realize entanglement with our experimental apparatus. The two qubit states $|F = 3, m_F = -3\rangle$ and $|F = 4, m_F = -4\rangle$ could serve as the two ground states $|i\rangle$ and $|a\rangle$, respectively. The excited state $|F' = 4, m_F = -4\rangle$ would then correspond to state $|e\rangle$.

List of Figures

1.1	Magneto-optical trap	5
1.2	Vacuum chamber	6
1.3	Experimental setup of MOT, dipole trap, and imaging system.	7
1.4	Level scheme of the cesium D-doublet.	8
1.5	Fluorescence light from single atoms in a MOT.	9
1.6	3D-view of our standing-wave trapping potential.	12
1.7	Transfer of one atom between MOT and dipole trap.	14
1.8	Molasses cooling in the dipole trap.	17
1.9	Three- and four-photon resonances during illumination in the dipole trap.	18
1.10	Images of a single trapped atom.	20
1.11	Image of a string of five trapped atoms.	22
1.12	Working principle of the optical conveyor belt.	23
1.13	Experimental setup of the optical conveyor belt.	24
1.14	Continued imaging of the transport of single atoms.	25
1.15	Zeeman splitting of the cesium ground state.	27
1.16	Geometry of laser beams for state preparation and detection.	29
1.17	State-selective detection.	30
1.18	Visualization of Bloch vector dynamics.	32
1.19	Setup for microwave spectroscopy.	33
1.20	Experimental sequence used for microwave spectroscopy.	34
1.21	Fourier limited π pulse spectrum.	35
1.22	Rabi oscillations in a homogenous magnetic offset field.	37
1.23	Adiabatic population transfer in the dressed state picture.	38
1.24	Microwave pulse shape for adiabatic population transfer.	39
1.25	Adiabatic population transfer in the Bloch vector model.	40
1.26	Setup for microwave spectroscopy using an adiabatic passage technique.	41
1.27	Adiabatic population transfer.	42
2.1	String of five trapped atoms.	48
2.2	Image analysis for frequency calibration.	50
2.3	Calibration of the atomic resonance frequencies.	52
2.4	Experimental setup for single atom addressing.	53
2.5	Image analysis of a three atom string.	54
2.6	Addressing an individual atom.	55

2.7	Measurement of the addressing resolution.	56
2.8	Resolution of our single atom addressing scheme.	58
2.9	Measurement of the differential circular light shift.	61
2.10	Adiabatic spin flip of single register qubits.	62
2.11	Rabi rotations on the quantum register.	64
2.12	Manipulation of more than one atom of the quantum register.	66
2.13	Coherent phase shift induced by non-resonant interaction with a microwave pulse.	69
2.14	Ramsey spectroscopy.	71
2.15	Decay of Ramsey fringes due to inhomogeneous broadening.	72
2.16	Spin echo.	74
2.17	Spin echo fringes in a magnetic guiding field.	75
2.18	Experimental sequence for the spin echo measurement of the quantum register.	79
2.19	Spin echo contrast of the quantum register.	80
2.20	Radial oscillations of the trapped atoms.	81
2.21	Probability distribution of $\Delta\delta$	83
2.22	Measurement of axial position fluctuations of the dipole trap.	86
3.1	An optical high-finesse resonator.	91
3.2	Single atom sorting with a vertical conveyer belt.	92
A.1	Light shift of the Zeeman sublevels.	96
B.1	Four-photon Raman resonance between two atoms and a cavity mode.	100
B.2	Calculated time evolution of the four-photon Rabi oscillation.	102

List of Tables

1.1	Fit parameters for the spectrum of Figure 1.21.	36
1.2	Parameters for the spectrum of Figure 1.27 (a).	43
2.1	Fit results for the normalized intensity distribution of Figure 2.2.	51
2.2	Parameters and results for the addressing spectra of Figure 2.8.	59
2.3	Fit parameters for the adiabatic passage spectrum of Figure 2.10.	63
2.4	Fit results for the Ramsey fringes of Figure 2.15.	73
2.5	Summary of the relevant dephasing mechanisms in a magnetic guiding field.	77
2.6	Parameters of the contrast according to Equations (2.41) and (2.42).	84
2.7	Overview of relaxation times.	87
B.1	Parameters for the calculation of Figure B.2.	104

Bibliography

- [1] P. Shor, *Polynomial-time algorithms for prime factorization and discrete logarithms on a quantum computer*, SIAM J. Comp. **26**, 1484 (1997)
- [2] L. Grover, *Quantum mechanics helps in searching for a needle in a haystack*, Phys. Rev. Lett. **97**, 325 (1997)
- [3] S. Lloyd, *Almost any quantum logic gate is universal*, Phys. Rev. Lett. **75**, 346 (1995)
- [4] R. Raussendorf and H. J. Briegel, *A one-way quantum computer*, Phys. Rev. Lett. **86**, 5188 (2001)
- [5] H. C. Nägerl, D. Leibfried, H. Rohde, G. Thalhammer, J. Eschner, F. Schmidt-Kaler, and R. Blatt, *Laser addressing of individual ions in a linear ion trap*, Phys. Rev. A **60**, 145 (1999)
- [6] I. L. Chuang, L. M. K. Vandersypen, X. Zhou, D. W. Leung, and S. Lloyd, *Experimental realization of a quantum algorithm*, Nature **393**, 143 (1998)
- [7] T. Yamamoto, Yu. A. Pashkin, O. Astafiev, Y. Nakamura, and J. S. Tsai, *Demonstration of conditional gate operation using superconducting charge qubits*, Nature **425**, 941 (2003)
- [8] Q. A. Turchette, C. S. Wood, B. E. King, C. J. Myatt, D. Leibfried, W. M. Itano, C. Monroe, and D. Wineland, *Deterministic entanglement of two trapped ions*, Phys. Rev. Lett. **81**, 3631 (1998)
- [9] C. A. Sackett, D. Kielpinski, B. E. King, C. Langer, V. Meyer, C. J. Myatt, M. Rowe, Q. A. Turchette, W. M. Itano, D. J. Wineland, and C. Monroe, *Experimental entanglement of four trapped ions*, Nature **404**, 256 (2000)
- [10] F. Schmidt-Kaler, H. Häffner, M. Riebe, S. Gulde, G. Lancaster, T. Deuschle, C. Becher, C. F. Roos, J. Eschner, and R. Blatt, *Realization of the Cirac-Zoller controlled-NOT quantum gate*, Nature **422**, 408 (2003)
- [11] D. Leibfried, B. DeMarco, V. Meyer, D. Lucas, M. Barrett, J. Britton, W. M. Itano, B. Jelenković, C. Langer, T. Rosenband, and D. J. Wineland, *Experimental demonstration of a robust, high-fidelity geometric two ion-qubit phase gate*, Nature **422**, 412 (2003)

-
- [12] S. Gulde, M. Riebe, G. P. T. Lancaster, C. Becher, J. Eschner, H. Häffner, F. Schmidt-Kaler, I. L. Chuang, and R. Blatt, *Implementing the Deutsch-Jozsa algorithm on an ion-trap quantum computer*, Nature **421**, 48 (2003)
- [13] L. M. K. Vandersypen, M. Steffen, G. Breyta, C. S. Yannoni, M. H. Sherwood, and I. L. Chuang, *Experimental realization of Shor's quantum factoring algorithm using nuclear magnetic resonance*, Nature **414**, 883 (2001)
- [14] S. Kuhr, W. Alt, D. Schrader, M. Müller, V. Gomer, and D. Meschede, *Deterministic delivery of a single atom*, Science **293**, 278 (2001)
- [15] N. Schlosser, G. Reymond, I. Protsenko, and P. Grangier, *Sub-poissonian loading of single atoms in a microscopic dipole trap*, Nature **411**, 1024 (2001)
- [16] N. Davidson, H. Jin Lee, C. S. Adams, M. Kasevich, and S. Chu, *Long Atomic Coherence Times in an Optical Dipole Trap*, Phys. Rev. Lett. **74**, 1311 (1995)
- [17] S. Kuhr, W. Alt, D. Schrader, I. Dotsenko, Y. Miroshnychenko, W. Rosenfeld, M. Khudaverdyan, V. Gomer, A. Rauschenbeutel, and D. Meschede, *Coherence properties and quantum state transportation in an optical conveyor belt*, Phys. Rev. Lett. **91**, 213002 (2003)
- [18] O. Mandel, M. Greiner, A. Widera, T. Rom, T. W. Hänsch, and I. Bloch, *Controlled collisions for multi-particle entanglement of optically trapped atoms*, Nature **425**, 937 (2003)
- [19] A. Rauschenbeutel, G. Nogues, S. Osnaghi, P. Bertet, M. Brune, J. M. Raimond, and S. Haroche, *Coherent Operation of a Tunable Quantum Phase Gate in Cavity QED*, Phys. Rev. Lett. **83**, 5166 (1999)
- [20] T. Pellizzari, S. A. Gardiner, J. I. Cirac, and P. Zoller, *Decoherence, Continuous Observation and Quantum Computing: A Cavity QED Model*, Phys. Rev. Lett. **75**, 3788 (1995)
- [21] L. You, X. X. Yi, and X. H. Su, *Quantum logic between atoms inside a high-Q optical cavity*, Phys. Rev. A **67**, 032308 (2003)
- [22] D. Schrader, I. Dotsenko, M. Khudaverdyan, Y. Miroshnychenko, A. Rauschenbeutel, and D. Meschede, *Neutral atom quantum register*, Phys. Rev. Lett. **93**, 150501 (2004)
- [23] D. Schrader, S. Kuhr, W. Alt, M. Müller, V. Gomer, and D. Meschede, *An optical conveyor belt for single neutral atoms*, Appl. Phys. B **73**, 819 (2001)
- [24] W. Alt, *An objective lens for efficient fluorescence detection of single atoms*, Optik **113**, 142 (2002)

-
- [25] Y. Miroshnychenko, D. Schrader, S. Kuhr, W. Alt, I. Dotsenko, M. Khudaverdyan, A. Rauschenbeutel, and D. Meschede, *Continued imaging of the transport of a single neutral atom*, Optics Express **11**, 3498 (2003)
- [26] D. P. DiVincenzo, *The physical implementation of quantum computation*, Fortschr. Phys. **48**, 771 (2000)
- [27] R. Hughes and T. Heinrichs, *A Quantum Information Science and Technology Roadmap, Neutral Atom Approaches to Quantum Information Processing and Quantum Computing* (2004), http://qist.lanl.gov/pdfs/neutral_atom.pdf
- [28] T. W. Hänsch and A. L. Schawlow, *Cooling of gases by laser radiation*, Opt. Commun. **13**, 68 (1975)
- [29] D. Wineland and H. Dehmelt, *Proposed $10^{14} \Delta\nu < \nu$ Laser Fluorescence Spectroscopy on Tl^+ Mono-Ion Oscillator III (side band cooling)*, Bull. Am. Phys. Soc. **20**, 637 (1975)
- [30] S. Chu, L. Hollberg, J. E. Bjorkholm, A. Cable, and A. Ashkin, *Three-dimensional Viscous Confinement and Cooling of Atoms by Resonance Radiation Pressure*, Phys. Rev. Lett. **55**, 48 (1985)
- [31] E. L. Raab, M. Prentiss, A. Cable, S. Chu, and D. E. Pritchard, *Trapping of Neutral Sodium Atoms with Radiation Pressure*, Phys. Rev. Lett. **59**, 2631 (1987)
- [32] M. H. Anderson, J. R. Ensher, M. R. Matthews, C. E. Wieman, and E. A. Cornell, *Observation of Bose-Einstein condensation in a dilute atomic vapor*, Science **269**, 198 (1995)
- [33] K. B. Davis, M. O. Mewes, M. R. Andrews, N. J. van Druten, D. S. Durfee, D. M. Kurn, and W. Ketterle, *Bose-Einstein condensation in a gas of sodium atoms*, Phys. Rev. Lett. **75**, 3969 (1995)
- [34] Z. Hu and H. J. Kimble, *Observation of a single atom in a magneto-optical trap*, Opt. Lett. **19**, 1888 (1994)
- [35] F. Ruschewitz, D. Bettermann, J. L. Peng, and W. Ertmer, *Statistical investigations on single trapped neutral atoms*, Europhys. Lett. **34**, 651 (1996)
- [36] D. Haubrich, H. Schadwinkel, F. Strauch, B. Ueberholz, R. Wynands, and D. Meschede, *Observation of individual neutral atoms in magnetic and magneto-optical traps*, Europhys. Lett. **34**, 663 (1996)
- [37] A. Ashkin, *Acceleration and Trapping of Particles by Radiation Pressure*, Phys. Rev. Lett. **24**, 156 (1970)
- [38] D. G. Grier, *A revolution in optical manipulation*, Nature **424**, 810 (2003)

- [39] V. S. Letokhov, *Doppler line narrowing in a standing light wave*, Pis. Zh. Eksp. Teor. Fiz. **7**, 348 (1968), engl. translation JETP Lett. **7**, 272 (1968)
- [40] R. Grimm, M. Weidemüller, and Y. B. Ovchinnikov, *Optical dipole traps for neutral atoms*, Adv. At. Mol. Opt. Phys. **42**, 95 (2000)
- [41] D. Frese, B. Ueberholz, S. Kuhr, W. Alt, D. Schrader, V. Gomer, and D. Meschede, *Single Atoms in an Optical Dipole Trap: Towards a Deterministic Source of Cold Atoms*, Phys. Rev. Lett. **85**, 3777 (2000)
- [42] W. Neuhauser, M. Hohenstatt, P. Toschek, and H. Dehmelt, *Localized visible Ba⁺ mono-ion oscillator*, Phys. Rev. A **22**, 1137 (1980)
- [43] H. C. Nägerl, D. Leibfried, F. Schmidt-Kaler, J. Eschner, and R. Blatt, *Coherent excitation of normal modes in a string of Ca⁺ ions*, Optics Express **3**, 89 (1998)
- [44] J. J. Bollinger, T. B. Mitchell, X. P. Huang, W. M. Itano, J. N. Tan, B. M. Jelenkovic, and D. J. Wineland, *Crystalline order in laser-cooled, non-neutral ion plasmas*, Phys. Plasmas **7**, 7 (2000)
- [45] A. Kastler, *The optical production and the optical detection of an inequality of population of the levels of spatial quantification of atoms. Application to the experiments of Stern and Gerlach and to magnetic resonance*, J. Phys. Radium **11**, 255 (1950)
- [46] A. Kastler, *Optical methods of studying magnetic resonance*, Physica **17**, 191 (1951)
- [47] W. Nagourney, J. Sandberg, and H. Dehmelt, *Shelved optical electron amplifier: observation of quantum jumps*, Phys. Rev. Lett. **56**, 2797 (1986)
- [48] S. Kuhr, *A controlled quantum system of individual neutral atoms*, Ph.D. thesis, Universität Bonn (2003), available at http://hss.ulb.uni-bonn.de/diss_online/
- [49] D. Schrader, S. Kuhr, W. Alt, Y. Miroshnychenko, I. Dotsenko, W. Rosenfeld, M. Khudaverdyan, V. Gomer, A. Rauschenbeutel, and D. Meschede, *Controlled transport of single neutral atom qubits*, in P. Hannaford, A. Sidorov, H. Bachor, and K. Baldwin, eds., *Proc. of the XVI ICOLS*, World Scientific Singapore (2003)
- [50] F. Bloch, *Nuclear Induction*, Phys. Rev. **70**, 460 (1946)
- [51] L. Allen and J. H. Eberly, *Optical resonance and two-level atoms*, Wiley, New York (1975)
- [52] S. Guérin, S. Thomas, and H. R. Jauslin, *Optimization of population transfer by adiabatic passage*, Phys. Rev. A **65**, 023409 (2002)
- [53] D. Haubrich, A. Höpe, and D. Meschede, *A simple model for optical capture of atoms in strong magnetic quadrupole fields*, Opt. Commun. **102**, 225 (1993)
- [54] W. Alt, *Optical control of single neutral atoms*, Ph.D. thesis, Universität Bonn (2004), available at http://hss.ulb.uni-bonn.de/diss_online/

-
- [55] J. D. Jackson, *Classical Electrodynamics*, Wiley, New York, 2nd edition (1962)
- [56] W. Alt, personal communication (2004)
- [57] W. Alt, D. Schrader, S. Kuhr, M. Müller, V. Gomer, and D. Meschede, *Single atoms in a standing-wave dipole trap*, Phys. Rev. A **67**, 033403 (2003)
- [58] I. Dotsenko, W. Alt, M. Khudaverdyan, S. Kuhr, D. Meschede, Y. Miroshnychenko, D. Schrader, and A. Rauschenbeutel, *Nanometric position control of single trapped neutral atoms* (2005), submitted, available at [arXiv:quant-ph/0411062](https://arxiv.org/abs/quant-ph/0411062)
- [59] D. Meschede, *Optik, Licht und Laser*, Teubner, Stuttgart (1999)
- [60] Marc Cheneau, *Laser cooling of single atoms in a standing-wave dipole trap*, internship report, Universität Bonn and ENS Cachon, Paris (2003)
- [61] V. Gomer, F. Strauch, B. Ueberholz, S. Knappe, and D. Meschede, *Single-atom dynamics revealed by photon correlations*, Phys. Rev. A **58**, 1657 (1998)
- [62] E. Hecht, *Optik*, Oldenbourg Wissenschaftsverlag, Oldenbourg, 3rd edition (2001)
- [63] H. J. Metcalf and P. van der Straten, *Laser Cooling and Trapping*, Springer, 1st edition (1999)
- [64] I. Dotsenko, W. Alt, S. Kuhr, D. Schrader, M. Müller, Y. Miroshnychenko, V. Gomer, A. Rauschenbeutel, and D. Meschede, *Application of electro-optically generated light fields for Raman spectroscopy of trapped cesium atoms*, Appl. Phys. B **78**, 711 (2004)
- [65] T. L. Gustavson, A. Landragin, and M. A. Kasevich, *Rotation sensing with a dual atom-interferometer Sagnac gyroscope*, Class. Quantum Grav. **17**, 2385 (2000)
- [66] P. Goy, personal communication (2003)
- [67] R. Barlow, *Statistics*, Wiley, New York (1989)
- [68] V. F. Ezhov, S. N. Ivanov, V. M. Lobashev, V. A. Nazarenko, G. D. Porsev, O. V. Serdyuk, A. P. Serebrov, and R. R. Tal'daev, *Adiabatic method of separated oscillating fields*, Pis'ma Zh. Eksp. Teor. Fiz. **24**, 39 (1976), [JEPT Lett., **24**, 34 (1976)]
- [69] S. V. Grigoriev, R. Kreuger, W. H. Kraan, F. M. Mulder, and M. Th. Rekveldt, *Neutron wave-interference experiments with adiabatic passage of neutron spin through resonant coils*, Phys. Rev. A **64**, 013614 (2001)
- [70] M. Khudaverdyan, W. Alt, I. Dotsenko, L. Förster, S. Kuhr, D. Meschede, Y. Miroshnychenko, D. Schrader, and A. Rauschenbeutel, *Adiabatic quantum state manipulation of single trapped atoms*, Phys. Rev. A (2005), in print, available at [arXiv:quant-ph/0411120](https://arxiv.org/abs/quant-ph/0411120)

-
- [71] T. Rickes, L. P. Yatsenko, S. Steuerwald, T. Halfmann, B. W. Shore, N. V. Vitanov, and K. Bergmann, *Efficient adiabatic population transfer by two-photon excitation assisted by a laser-induced Stark shift*, J. Chem. Phys. **113**, 534 (2000)
- [72] S. Kuhr, W. Alt, D. Schrader, I. Dotsenko, Y. Miroshnychenko, A. Rauschenbeutel, and D. Meschede, *Analysis of dephasing mechanisms in a standing wave dipole trap*, Phys. Rev. A (2005), in print, available at [arXiv:quant-ph/0410037](https://arxiv.org/abs/quant-ph/0410037)
- [73] R. Scheunemann, F. S. Cataliotti, T. W. Hänsch, and M. Weitz, *Resolving and addressing atoms in individual sites of a CO₂-laser optical lattice*, Phys. Rev. A **62**, 051801 (2000)
- [74] R. Dumke, M. Volk, T. Mütter, F. B. J. Buchkremer, G. Birkl, and W. Ertmer, *Micro-optical realization of arrays of selectively addressable dipole traps: A scalable configuration for quantum computation with atomic qubits*, Phys. Rev. Lett. **89**, 097903 (2002)
- [75] M. H. Levitt, *Spin dynamics*, Wiley, West Sussex (2001)
- [76] C. D. Mackay, R. N. Tubbs, R. Bell, D. Burt, and I. Moody, *Sub-Electron Read Noise at MHz Pixel Rates*, in *SPIE 4306 Conference Proceedings*, 289 (2001)
- [77] N. Ramsey, *Molecular Beams*, Oxford University Press, London (1956)
- [78] N. Ramsey, *The method of successive oscillatory fields*, Physics Today **33**, 25 (1980)
- [79] E. Hahn, *Nuclear Induction Due to Free Larmor Precession*, Phys. Rev. **77**, 297 (1950)
- [80] M. F. Andersen, A. Kaplan, T. Grünzweig, and N. Davidson, *Echo spectroscopy and atom optics billiards*, Comm. Nonlin. Sc. and Num. Sim. **8**, 289 (2003)
- [81] A. Rauschenbeutel, personal communication
- [82] E. Hahn, *Spin Echoes*, Phys. Rev. **80**, 580 (1950)
- [83] M. F. Andersen, A. Kaplan, and N. Davidson, *Echo spectroscopy and quantum stability for trapped atoms*, Phys. Rev. Lett. **90**, 023001 (2003)
- [84] D. W. Allan, *Statistics of atomic frequency standards*, Proc. IEEE **54**, 221 (1966)
- [85] H. J. Lee, C. S. Adams, M. Kasevich, and S. Chu, *Raman Cooling of Atoms in an Optical Dipole Trap*, Phys. Rev. Lett. **76**, 2658 (1996)
- [86] H. Perrin, A. Kuhn, I. Bouchoule, and C. Salomon, *Sideband cooling of neutral atoms in a far-detuned optical lattice*, Europhys. Lett. **42**, 395 (1998)
- [87] S. E. Hamann, D. L. Haycock, G. Klose, P. H. Pax, I. H. Deutsch, and P. S. Jessen, *Resolved-Sideband Raman Cooling to the Ground State of an Optical Lattice*, Phys. Rev. Lett. **80**, 4149 (1998)

-
- [88] S.-B. Zheng and G.-C. Guo, *Efficient Scheme for Two-Atom Entanglement and Quantum Information Processing in Cavity QED*, Phys. Rev. Lett. **85**, 2392 (2000)
- [89] X. X. Yi, X. H. Su, and L. You, *Conditional quantum phase gate between two 3-state atoms*, Phys. Rev. Lett. **90**, 097902 (2003)
- [90] C. Marr, A. Beige, and G. Rempe, *Entangled-state preparation via dissipation-assisted adiabatic passages*, Phys. Rev. A **68**, 033817 (2003)
- [91] J. A. Sauer, K. M. Fortier, M. S. Chang, C. D. Hamley, and M. S. Chapman, *Cavity QED with optically transported atoms*, Phys. Rev. A **69**, 051804 (2004)
- [92] J. McKeever, J. R. Buck, A. D. Boozer, A. Kuzmich, H.-C. Nägerl, D. M. Stamper-Kurn, and H. J. Kimble, *State-Insensitive Cooling and Trapping of Single Atoms in an Optical Cavity*, Phys. Rev. Lett. **90**, 133602 (2003)
- [93] A. Kuhn, M. Hennrich, and G. Rempe, *Deterministic single-photon source for distributed quantum networking*, Phys. Rev. Lett. **89**, 067901 (2002)
- [94] J. McKeever, A. Boca, A. D. Boozer, R. Miller, J. R. Buck, A. Kuzmich, and H. J. Kimble, *Deterministic generation of single photons from one atom trapped in a cavity*, Science **303**, 1992 (2004)
- [95] T. Fischer, P. Maunz, P. W. H. Pinkse, T. Puppe, and G. Rempe, *Feedback on the motion of a single atom in an optical cavity*, Phys. Rev. Lett. **88**, 163002 (2002)
- [96] D. A. Steck, K. Jacobs, H. Mabuchi, T. Bhattacharya, and S. Habib, *Quantum feedback control of atomic motion in an optical cavity*, Phys. Rev. Lett. **92**, 223004 (2004)
- [97] H. W. Chan, A. T. Black, and V. Vuletic, *Observation of collective-emission-induced cooling of atoms in an optical cavity*, Phys. Rev. Lett. **90**, 063003 (2003)
- [98] P. Maunz, T. Puppe, I. Schuster, N. Syassen, P. W. H. Pinkse, and G. Rempe, *Cavity cooling of a single atom*, Nature **428**, 50 (2004)
- [99] L. You, X. X. Yi, and X. H. Su, *Quantum logic between atoms inside a high-Q optical cavity*, Phys. Rev. A **67**, 032308 (2003)
- [100] J. Preskill, *Reliable quantum computers*, Proc. R. Soc. London, Ser. A **454**, 385 (1998)
- [101] D. Kielpinski, V. Meyer, M. A. Rowe, C. A. Sackett, W. M. Itano, C. Monroe, and D. J. Wineland, *Architecture for a large-scale ion-trap quantum computer*, Nature **417**, 709 (2002)
- [102] G. Brennen, C. Caves, P. Jessen, and I. Deutsch, *Quantum Logic Gates in Optical Lattices*, Phys. Rev. Lett. **82**, 1060 (1999)

-
- [103] O. Mandel, M. Greiner, A. Widera, T. Rom, T. W. Hänsch, and I. Bloch, *Coherent transport of neutral atoms in spin-dependent optical lattice potentials*, Phys. Rev. Lett. **91**, 010407 (2003)
- [104] D. Jaksch, H.-J. Briegel, J. Cirac, C. Gardiner, and P. Zoller, *Entanglement of atoms via cold controlled collisions*, Phys. Rev. Lett. **82**, 1975 (1999)
- [105] J. J. Sakurai, *Modern Quantum Mechanics*, Addison Wesley, 2nd edition (1994)
- [106] I. I. Sobelman, *Atomic Spectra and Radiative Transitions*, Springer, Berlin (1996)
- [107] A. R. Edmonds, *Angular momentum in quantum mechanics*, Princeton University Press, Princeton, 3rd edition (1974)
- [108] M. Fabry and J. R. Cussenot, *Détermination théorique et expérimentale des forces d'oscillateur des transitions de l'atome de césium*, Can. J. Phys. **54**, 836 (1976)
- [109] H. Carmichael, *An Open Systems Approach to Quantum Optics*, Springer, Berlin (1993)
- [110] S. M. Tan, *A computational toolbox for quantum and atom optics*, J. Opt. B: Quant. Semiclass. Opt. **1**, 424 (1999)
- [111] M. O. Scully and S. Zubairy, *Quantum Optics*, Cambridge University Press, Cambridge (1997)
- [112] C. Cohen-Tannoudji, J. Dupont-Roc, and G. Grynberg, *Atom-Photon Interactions*, Wiley, New York (1992)

Acknowledgements

Eine aufregende, spannende Zeit neigt sich dem Ende, während der ich viel erlebt und gelernt habe. Denen, die diese Zeit mit mir verbracht und mich unterstützt haben, gilt mein herzlicher Dank.

Prof. Dieter Meschede hat mir die Gelegenheit gegeben, an einem wirklich grandiosen Experiment zu promovieren. Für den großen Entscheidungsspielraum, den er mir immer gewährt hat, aber auch für seine Unterstützung in entscheidenden Situationen möchte ich mich ausdrücklich bedanken. Prof. Karsten Buse danke ich an dieser Stelle für die Übernahme des Korreferats.

Mein besonderer Dank gilt der alten Doktoranden-Garde, Dr. Stefan Kuhr und Wolfgang Alt. Zusammen haben wir ein riesiges und komplexes Experiment aufgebaut, bei dessen Anblick mich heute noch immer wieder erstaunt, dass es funktioniert. Ohne Stefans sagenhaftes Management und seiner Zielstrebigkeit, der Apparatur (und uns) permanent das Äußerste abzuverlangen, hätten wir bis heute noch nicht ein paper geschrieben. Sowohl von diesen Tugenden als auch von seinem untrüglichen Gefühl für die spektakulären Messungen habe ich viel gelernt, mal ganz abgesehen von den vielen Abenden im "Quiet Man". Wir wären aber auch nicht weit gekommen ohne Wolfgang, der uns immer wieder auf den Boden der Tatsachen zurückgeholt hat. Mit seinem unglaublichen Gespür für die Physik gibt es keine Frage, die Wolfgang nicht beantworten könnte, und kein Problem, das er nicht lösen könnte. Bedanken möchte ich mich auch für die vielen Diskussionen mit unserem Post-Doc während dieser Zeit, Dr. Victor Gomer, der jeden auch noch so komplizierten Effekt auf einem Briefumschlag abschätzen kann und nie mehr als 10 % daneben liegt. Ich danke Euch allen für eine erfolgreiche, lehrreiche und lustige Zeit, die ich sicher nicht vergessen werde.

Mittlerweile hat eine neue Generation von Doktoranden dieses Experiment übernommen, Yevhen Miroshnychenko, Igor Dotsenko und Mika Khudaverdyan. Ohne dieses sagenhafte Trio aus der Ukraine hätte ich wahrscheinlich keinen Datenpunkt für meine Dissertation messen können. Nicht selten musste Yevhen, dem ich die Entwicklung der Feedback-Software zu verdanken habe, meine Sonderwünsche in die Software einbauen, und das innerhalb kürzester Zeit, um die Messungen nicht zu verzögern. Igor bewundere ich um seine eiserne Disziplin, mit der er viele Tage und Nächte mit brillantem Verstand das Experiment vorantreibt. Ebenso tapfer ist Mika, dem der Humor auch nach 24 Stunden Messung nicht ausgeht und weiter unermüdlich die Dipolfalle justiert. Ich danke Euch für Eure Unterstützung und wünsche Euch den gleichen Erfolg für Eure Doktorarbeiten.

Post-Doc dieser neuen Doktorandengeneration ist Dr. Arno Rauschenbeutel, der in vielen Diskussionen immer wieder mit hervorragenden Ideen zum Gelingen unserer Forschung beiträgt. Ihm wünsche ich Erfolg bei seiner bald anstehenden Habilitation.

Martin Müller, Wenjamin Rosenfeld und Leonid Förster, die neben Yevhen, Igor und Mika eine Diplomarbeit bei uns angefertigt haben, und unserem Ferienpraktikanten Marc Cheneau danke ich ebenfalls für die gute und freundschaftliche Zusammenarbeit. Jeder von Ihnen hat einen wertvollen Beitrag zum Gelingen unseres Experimentes geleistet. An dieser Stelle möchte ich mich bei allen Mitgliedern der Arbeitsgruppe Meschede bedanken, die immer hilfsbereit waren und erheblich dazu beigetragen haben, dass mir meine Zeit am IAP wirklich Spaß gemacht hat. Für das kritische Lesen dieser Arbeit und wertvolle Korrekturvorschläge danke ich Wolfgang Alt, Dr. Arno Rauschenbeutel und Dr. Stefan Kuhr.

Das Rückgrat unseres Instituts bilden die Elektronik- und Feinmechanik-Werkstätten, die jeden noch so verrückten Auftrag von uns bearbeitet haben. Dafür möchte ich mich ausdrücklich bedanken. Des weiteren danke ich den guten Feen aus dem dritten Stock, Anneliese Miglo, Fien Latumahina und Ilona Jaschke, und Dr. Dietmar Haubrich für ihre enorme Hilfsbereitschaft. Sie sorgen für die reibungslose Abwicklung aller verwaltungstechnischen Aufgaben und halten uns permanent den Rücken frei. Sowohl ihnen als auch allen weiteren Institutsmitgliedern danke ich für die freundschaftliche Atmosphäre im Institut, bei der das Arbeiten gleich doppelt so viel Spaß macht.

At this point I would like to take the opportunity to thank Prof. Jeff Kimble for giving me the chance to be part of his group at Caltech for six months. I have learned a lot during that time apart from enjoying the amenities of Southern California. My special regards go to Theresa Lynn and Kevin Birnbaum with whom I set up an apparatus for cavity QED experiments. Thank you for a good time and good luck for your future! Also I would like to thank Prof. Nir Davidson and Prof. Hal Metcalf for being in Bonn over extended periods of time and for truly valuable discussions.

Last but not least, gilt mein besonderer Dank den Menschen, die mich zwar nicht in physikalischen Fachfragen, aber dafür umso mehr in allen anderen Belangen meines Lebens unterstützen. Meine Eltern haben mir immer zur Seite gestanden und mich auf meinem aufregenden Weg begleitet, sowohl in guten als auch in schwierigen Zeiten. Viel Kraft schenkt mir auch meine Freundin Nicola, die mich aus dem fernen Berlin immer wieder aufmuntert und unterstützt, und für die ich bald endlich wieder mehr Zeit habe.

Herzlich danken möchte ich schliesslich den Sponsoren, die durch ihre finanzielle Unterstützung meine Dissertation ermöglicht haben: der DFG, der Europäischen Kommission, der Studienstiftung des Deutschen Volkes, dem DAAD und der Deutschen Telekom Stiftung.